



ISSN 1343-2230

CNS-REP-97
March, 2019

Annual Report 2017

Center for Nuclear Study,
Graduate School of Science, the University of Tokyo

Editor
Taku Gunji

Center for Nuclear Study

CNS Reports are available from:

Wako-Branch at RIKEN

Center for Nuclear Study,

Graduate School of Science, the University of Tokyo

2-1 Hirosawa, Wako

351-0198, Japan

Tel: +81-48-464-4191

Fax: +81-48-464-4554

Annual Report 2017

Center for Nuclear Study,
Graduate School of Science, the University of Tokyo

Preface

This is the annual report of the Center for Nuclear Study (CNS), Graduate School of Science, the University of Tokyo, for the fiscal year 2017 (April 2017 through March 2018). During this period, a lot of research activities in various fields of nuclear physics have been carried out and a wide variety of fruitful results have been obtained at CNS. This report summarizes research such activities. I hereby mention some highlights of the report.

The Center for Nuclear Study (CNS) aims to elucidate the nature of nuclear system by producing the characteristic states where the Isospin, Spin and Quark degrees of freedom play central roles. These researches in CNS lead to the understanding of the matter based on common natures of many-body systems in various phases. We also aim at elucidating the explosion phenomena and the evolution of the universe by the direct measurements simulating nuclear reactions in the universe. In order to advance the nuclear science with heavy-ion reactions, we develop AVF upgrade, CRIB and SHARAQ facilities in the large-scale accelerators laboratories RIBF. The OEDO facility has been developed as an upgrade of the SHARAQ, where a RF deflector system has been introduced to obtain a good quality of low-energy beam. We added a new group for fundamental symmetry by using heavy RIs. We promote collaboration programs at RIBF as well as RHIC-PHENIX and ALICE-LHC with scientists in the world, and host international meetings and conferences. We also provide educational opportunities to young scientists in the heavy-ion science through the graduate course as a member of the department of physics in the University of Tokyo and through hosting the international summer school.

The NUSPEQ (NUclear SPectroscopy for Extreme Quantum system) group studies exotic structures in high-isospin and/or high-spin states in nuclei. The CNS GRAPE (Gamma-Ray detector Array with Position and Energy sensitivity) is a major apparatus for high-resolution in-beam gamma-ray spectroscopy. Missing mass spectroscopy using the SHARAQ is used for another approach on exotic nuclei. In 2017, the following progress has been made. Experimental data taken under the EURICA collaboration has been analyzed for studying octupole deformation in neutron-rich Ba isotopes and preparing publication. A new experiment measuring the $^4\text{He}(^8\text{He}, ^8\text{Be})4n$ reaction was performed for better statistics and better accuracy in order to verify a candidate of the ground state of the tetra neutrons just above the $4n$ threshold, which is under analysis.

The main activity of the nuclear astrophysics group in CNS is experimental studies on astrophysical reactions and special nuclear clustering using the low-energy RI beam separator CRIB. In 2017, a strong indication of an exotic linear-chain cluster structure in ^{14}C nucleus was presented based on the ^{10}Be resonant scattering measurement at CRIB. To give a solution to the cosmological ^7Li abundance problem, two experimental projects are in progress. One is to determine the $^7\text{Be}(n, \gamma)/(n, p)$ astrophysical reaction rates with the Trojan Horse method, and another is the measurement of $^7\text{Be}(d, p)$ with a ^7Be -implanted target. The latter project is in collaboration with RCNP, Osaka Univ. and JAEA, and CRIB was used for the ^7Be target production. Based on the interest of the galactic γ -ray production, a proton resonant scattering experiment with ^{26}Al isomeric beam was performed at CRIB in Mar. 2017. With the analysis followed that, the isomeric purity was found to be about 50%. Resonances in ^{27}Si are observed in the relevant energy range of supernovae, and we may be able to discuss possible destruction of ^{26}Al in supernovae.

Main goal of the quark physics group is to understand the properties of hot and dense nuclear matter created by colliding heavy nuclei at relativistic energies. The group has been involved in the PHENIX experiment at Relativistic Heavy Ion Collider (RHIC) at Brookhaven National Laboratory, and the ALICE experiment at Large Hadron Collider (LHC) at CERN. As for ALICE, the group has involved in the data analyses, which include the measurement of low-mass lepton pairs in Pb-Pb and p-Pb collisions, J/ψ measurements in p-Pb collisions, long range two particle correlations in p-Pb collisions, and searches for thermal photons in p-Pb collisions. The group has involved in the ALICE-

TPC upgrade using a Gas Electron Multiplier (GEM). Development of the new data readout system for the upgrade, which aims online data processing by utilizing FPGA and GPU, has been ongoing in 2017.

The Exotic Nuclear Reaction group studies various exotic reactions induced by beams of unstable nuclei. One subject is inverse-kinematics (p,n) reaction. In 2017 a set of neutron counters PANDORA was used for the first time at HIMAC facility for the study of the ${}^6\text{He}(p,n)$ reaction. Candidate nuclei to study are high spin isomers such as ${}^{52}\text{Fe}(12^+)$. Development of isomer beam was carried out.

The OEDO/SHARAQ group pursues experimental studies of RI beams by using the high-resolution beamline and the SHARAQ spectrometer. A mass measurement by TOF-B ρ technique for very neutron-rich successfully reaches calcium isotopes beyond $N=34$, ${}^{55-57}\text{Ca}$, and the preparation of publication is ongoing. The experimental study of 0^- strength in nuclei using the parity-transfer charge exchange (${}^{16}\text{O}$, ${}^{16}\text{F}$) is on progress and the data analysis is on the final stage. The OEDO beamline, which was an upgrade of the high-resolution beamline to produce low-energy RI beams, has started the operation in June and has successfully achieved the designed ion-optical performance. The first and second experiments were performed in October and November, and new data for nuclear transmutation of long lived fission products (LLFPs) were successfully obtained.

Two types of gaseous active target TPCs called CAT's and GEM-MSTPC are developed and used for the missing mass spectroscopy. The CAT's are employed for the study of equation of state of nuclear matter. The measurement of giant monopole resonance in ${}^{132}\text{Sn}$ at RIBF with CAT-S and the data analysis is ongoing. In 2017, we developed a larger active target called CAT-M, which has 10-times larger active volume than that of CAT-S. The CAT-M was commissioned at HIMAC and the excitation energy spectrum of ${}^{136}\text{Xe}$ for proton scattering was measured. The GEM-MSTPC is employed for the nuclear astrophysics study. The data analysis of (α , p) reaction on ${}^{18}\text{Ne}$ and ${}^{22}\text{Mg}$ and the β decay of ${}^{16}\text{Ne}$ followed by γ emission are ongoing.

A recoil particle detector for missing mass spectroscopy, named TiNA, had been developed under the collaboration with RIKEN and RCNP. TiNA consists of 6 sector telescopes. Each of which as a stripped-type SSD and 2 CsI(Tl) crystals. After the test experiment at the tandem facility of Kyushu Univ., TiNA was employed at the physics experiment with OEDO. Development of the tritium target is still on-going. Several deuterium doped Ti targets were fabricated at the Toyama Univ. They were tested by using $d({}^{12}\text{C},d)$ reaction at the tandem facility at Kyushu. The amount of deuterium was found to be scattered. The optimum condition to make the target will be sought for. The production cross section ${}^{178m2}\text{Hf}$ was evaluated for the mass production in the future. The digital signal processing devices for the GRAPE have been developed to measure the cascade transitions from the isomeric state. After chemical separation of Hf at the hot laboratory at RIBF. The weak cascade decay was successfully measured.

One of the major tasks of the accelerator group is the AVF upgrade project that includes development of ion sources, upgrading the AVF cyclotron of RIKEN and the beam line to CRIB. In 2017, the operating time of the HyperECR was 2414 hours, which is 61 % of the total operating time of the AVF cyclotron. The beam extraction system of the HyperECR is under development to realize a high intensity and low emittance beam. We have succeeded to suppress ${}^{12}\text{C}^{4+}$ beam which contaminated ${}^{18}\text{O}^{6+}$ beam by measuring the light intensity of the CIV line spectrum. The calculation model of injection beam orbit of the AVF cyclotron was completed and the adjustment of the position and angle deviation between the measured beam orbit and the calculated beam orbit is carried on. The detailed studies on ion optics of the beamline to CRIB from AVF cyclotron were performed with beam diagnosis system and simulation code, and it turned out the loss of the beam intensity is occurred at the entrance of the vertical deflection bending magnet.

Although the Standard Model of particle physics is being steadily and successfully verified, the disappearance of the antimatter in the universe could not be sufficiently explained; a more fundamental framework is required and has to be studied. In order to understand the mechanism of matter-antimatter symmetry violation, we are developing the next generation experiments employing ultra-

cold atoms to search for the electron electric dipole moment (EDM) using heavy element francium (Fr) in an optical lattice at RIBF. The developments of a high intensity surface ionizer to produce Fr and a magneto-optical trap (MOT) are in progress, and Fr-MOT experiments are going on at present at CYRIC.

The nuclear theory group participates a project, “Priority Issue 9 to be tackled by using the Post-K Computer” and promotes computational nuclear physics utilizing supercomputers. In FY2017, we performed the Monte Carlo shell model calculations of the Sn isotopes and revealed that the anomalous enhancement of the B(E2) transition probabilities in the neutron-deficient region is caused by the proton excitation from the $1g_{9/2}$ orbit, and found that the second-order quantum phase transition occurs around N=66. We also investigated the double Gamow-Teller strength distribution of double-beta decay emitters, such as ^{48}Ca . We theoretically predict a linear relation between the nuclear matrix elements of the double Gamow-Teller transition and the neutrinoless double beta decay. In parallel, we have been promoting the CNS-RIKEN collaboration project on large-scale nuclear structure calculations and performed shell-model calculations under various collaborations with many experimentalists for investigating the exotic structure of neutron-rich nuclei, such as ^{35}Mg , ^{136}Ba , ^{138}Ce , and ^{135}La .

The 16th CNS International Summer School (CNSSS17) has been organized in August 2017 with many invited lecturers including four foreign distinguished physicists.

Finally, I thank Mr. Oki and other administrative staff members for their heartfelt contributions throughout the year.

Susumu Shimoura
Director of CNS

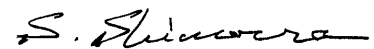


Table of Contents

1a. Experimental Nuclear Physics: Low and Intermediate Energies

Evaluation of the nuclear reaction of $^{79}\text{Se}(n, \gamma)$ via $^{79}\text{Se}(d, p)$ reaction at OEDO	1
<i>N. Imai, M. Dozono, S. Michimasa, S. Ota, T. Sumikama, O. Beliuskina, S. Hayakawa, C. Iwamoto, K. Kawata, N. Kitamura, S. Masuoka, P. Schrock, H. Shimizu, S. Shimoura, K. Wimmer, K. Yako, H. Yamaguchi, L. Yang, N. Chiga, D. Nagae, S. Omika, H. Otsu, H. Sakurai, D. Suzuki, K. Yamada, S. Takeuchi, H. Miki, H. Yamada, S. Kawase, K. Nakano, Y. Watanabe, K. Iribe, T. Teranishi, N. Aoi, E. Ideguchi, H.J. Ong, R. Yanagihara</i>	
Proton- and deuteron-induced reactions on ^{107}Pd at 20 – 30 MeV/u	3
<i>M. Dozono, N. Imai, S. Michimasa, T. Sumikama, N. Chiga, S. Ota, O. Beliuskina, S. Hayakawa, K. Iribe, C. Iwamoto, S. Kawase, K. Kawata, N. Kitamura, S. Masuoka, K. Nakano, P. Schrock, D. Suzuki, R. Tsunoda, K. Wimmer, D. S. Ahn, N. Fukuda, E. Ideguchi, K. Kusaka, H. Miki, H. Miyatake, D. Nagae, M. Nakano, S. Ohmika, M. Ohtake, H. Otsu, H. J. Ong, S. Sato, H. Shimizu, Y. Shimizu, H. Sakurai, X. Sun, H. Suzuki, M. Takaki, H. Takeda, S. Takeuchi, T. Teranishi, H. Wang, Y. Watanabe, Y. X. Watanabe, H. Yamada, H. Yamaguchi, R. Yanagihara, L. Yang, Y. Yanagisawa, K. Yoshida, S. Shimoura</i>	
Study of proton- and deuteron-induced reactions on the long-lived fission product ^{93}Zr at 30 MeV/u in inverse kinematics	5
<i>K. Iribe, M. Dozono, N. Imai, S. Michimasa, T. Sumikama, N. Chiga, S. Ota, O. Beliuskina, S. Hayakawa, C. Iwamoto, S. Kawase, K. Kawata, N. Kitamura, S. Masuoka, K. Nakano, P. Schrock, D. Suzuki, R. Tsunoda, K. Wimmer, D. S. Ahn, N. Fukuda, E. Ideguchi, K. Kusaka, H. Miki, H. Miyatake, D. Nagae, M. Nakano, S. Ohmika, M. Ohtake, H. Otsu, H. J. Ong, S. Sato, H. Shimizu, Y. Shimizu, H. Sakurai, X. Sun, H. Suzuki, M. Takaki, H. Takeda, S. Takeuchi, T. Teranishi, H. Wang, Y. Watanabe, Y. X. Watanabe, H. Yamada, H. Yamaguchi, R. Yanagihara, L. Yang, Y. Yanagisawa, K. Yoshida, S. Shimoura</i>	
Development of a tritium loaded target for reaction studies at the RIBF	7
<i>K. Wimmer, P. Schrock, Y. Beaujeault-Taudiere, Y. Hatano, N. Imai, K. Iribe, N. Kitamura, P. Shi, D. Suzuki, T. Teranishi</i>	
Characterization of a tritium-loaded titanium target through elastic scattering on ^{94}Sr and ^{84}Kr ...	9
<i>N. Kitamura, K. Wimmer, P. C. Bender, G. Hackman, J. Henderson, N. Imai</i>	
The measurement of proton resonance scattering on ^{118}Sn	11
<i>R. Tsunoda, N. Imai, K. Iribe, S. Sakaguchi, T. Teranishi, K. Ueno</i>	
Cross sections of the $^7\text{Be} + n$ reactions relevant to the cosmological Li problem	13
<i>S. Hayakawa, M. La Cognata, L. Lamia, H. Shimizu, L. Yang, H. Yamaguchi, K. Abe, O. Beliuskina, S. M. Cha, K. Y. Chae, S. Cherubini, P. Figueroa, Z. Ge, M. Gulino, J. Hu, A. Inoue, N. Iwasa, D. Kahl, A. Kim, D. H. Kim, G. Kiss, S. Kubono, M. La Commara, M. Lattuada, E. J. Lee, J. Y. Moon, S. Palmerini, C. Parascandolo, S. Y. Park, D. Pierroutsakou, R. G. Pizzone, G. G. Rapisarda, S. Romano, C. Spitaleri, X. D. Tang, O. Trippella, A. Tumino, P. Vi, N. T. Zhang</i>	
Breakup mechanisms of the proton-dripline system $^{17}\text{F}+^{58}\text{Ni}$ at energies around the Coulomb barrier	15

<i>L. Yang, C. J. Lin, N. R. Ma, H. Yamaguchi, D. X. Wang, L. J. Sun, K. Abe, M. La Commara, K. Y. Chae, S. M. Cha, S. Hayakawa, A. Kim, D. Kahl, M. S. Kwag, H. M. Jia, M. Mazzocco, C. Parascandolo, D. Pierroutsakou, C. Signorini, E. Strano, Y. Sakaguchi, F. Yang, Y. Y. Yang, G. X. Zhang, G. L. Zhang, M. Pan, X. X. Xu</i>	
Measurement of low-energy E1 strength in ^{136}Xe with CAT-M via proton inelastic scattering ...	17
<i>C. Iwamoto, S. Ota, S. Hayakawa, K. Kawata, Y. Mizoi, R. Kojima, H. Tokieda, N. Zhang, O. Beliuskina, M. Dozono, T. Harada, N. Imai, T. Isobe, N. Kitamura, S. Masuoka, S. Michimasa, T. Murakami, D. Suzuki, R. Tsunoda, J. Zenihiro, and E. Takada,</i>	
Deuteron Elastic Scattering on ^{16}O in inverse kinematics with CAT-S	19
<i>H. Tokieda, S. Ota, M. Dozono, N. Imai, M. Itoh, Y. Kiyokawa, M. Kobayashi, C. S. Lee, S. Michimasa, Y. Nasu, E. Takada, T. Uesaka, K. Yako, J. Zenihiro</i>	
Production of isomer around ^{52}Fe nucleus via projectile fragmentation	21
<i>K. Kawata, S. Ota, M. Dozono, J. Zenihiro, C. Iwamoto, N. Kitamura, H. Sakai, S. Masuoka, S. Michimasa, K. Yako, T. Harada, H. Nishibata, R. Tsunoda, N. Imai, T. Sato,</i>	
Search for double Gamow-Teller giant resonance in ^{48}Ti	23
<i>M. Takaki, T. Uesaka, N. Aoi, M. Dozono, T. Furuno, C. Iwamoto, T. Kawabata, M. Kobayashi, Y. Matsuda, M. Matsushita, S. Michimasa, S. Ota, M. Sasano, L. Stuhl, A. Tamii, M. Tsumura, R. Yokoyama, J. Zenihiro, S. Shimoura</i>	
Re-measurement of the $^4\text{He}(^8\text{He}, ^8\text{Be})$ reaction	25
<i>S. Masuoka, S. Shimoura, M. Takaki, S. Ota, S. Michimasa, M. Dozono, C. Iwamoto, K. Kawata, N. Imai, N. Kitamura, M. Kobayashi, R. Nakajima, H. Tokieda, R. Yokoyama, D. S. Ahn, H. Baba, N. Fukuda, T. Harada, E. Ideguchi, N. Inabe, Y. Kondo, T. Kubo, Y. Maeda, F. M. Marques, M. Matsushita, T. Nakamura, N. Orr, H. Sakai, H. Sato, P. Schrock, L. Stuhl, T. Sumikama, H. Suzuki, H. Takeda, K. Taniue, T. Uesaka, K. Wimmer, K. Yako, Y. Yamaguchi, Y. Yanagisawa, K. Yoshida, J. Zenihiro</i>	
Present status of EDM experiment with laser cooled radioactive atoms	27
<i>Y. Sakemi, H. Nagahama, T. Hayamizu, N. Ozawa, K. S. Tanaka, K. Harada, A. Uchiyama, J. Tsutsumi</i>	
1b. Experimental Nuclear Physics: PHENIX Experiment at BNL-RHIC and ALICE Experiment at CERN-LHC	
Progress of low mass dielectron analyses in pp and Pb-Pb collisions with ALICE at the LHC ...	29
<i>T. Gunji for the ALICE Collaboration</i>	
J/ψ production in $p\text{-Pb}$ collisions at $\sqrt{s_{\text{NN}}} = 5.02$ TeV	31
<i>S. Hayashi, T. Gunji for the ALICE Collaboration</i>	
Long-range correlations in $p\text{-Pb}$ collisions with ALICE	33
<i>Y. Sekiguchi, T. Gunji for the ALICE Collaboration</i>	
Direct photon measurement via external conversions in pp and $p\text{-Pb}$ collisions at LHC-ALICE .	35
<i>H. Murakami, T. Gunji for the ALICE collaboration</i>	

2. Accelerator and Instrumentation

Commissioning of the OEDO beamline	37
<i>S. Michimasa, J.W. Hwang, K. Yamada, S. Ota, M. Dozono, N. Imai, K. Yoshida, Y. Yanagisawa, K. Kusaka, M. Ohtake, M. Matsushita, D.S. Ahn, O. Beliuskina, N. Chiga, K. Chikaato, N. Fukuda, S. Hayakawa, E. Ideguchi, K. Iribe, C. Iwamoto, S. Kawase, K. Kawata, N. Kitamura, S. Masuoka, H. Miyatake, D. Nagae, R. Nakajima, T. Nakamura, K. Nakano, S. Omika, H. Otsu, H. Sakurai, P. Schrock, H. Shimizu, Y. Shimizu, T. Sumikama, X. Sun, D. Suzuki, H. Suzuki, M. Takaki, M. Takechi, H. Takeda, S. Takeuchi, R. Tsunoda, H. Wang, Y. Watanabe, Y.X. Watanabe, K. Wimmer, K. Yako, H. Yamaguchi, L. Yang, H. Yoshida, S. Shimoura</i>	
Angle-Tunable Degradar for OEDO Beamline	39
<i>J.W. Hwang, S. Michimasa, S. Ota, M. Dozono, N. Imai, K. Yoshida, Y. Yanagisawa, K. Kusaka, M. Ohtake, D. S. Ahn, O. Beliuskina, N. Fukuda, C. Iwamoto, S. Kawase, K. Kawata, N. Kitamura, S. Masuoka, H. Otsu, H. Sakurai, P. Schrock, T. Sumikama, H. Suzuki, M. Takaki, H. Takeda, R. Tsunoda, K. Wimmer, K. Yako, S. Shimoura</i>	
GEM-TPC Development Collaboration	41
<i>S. Ota, C. Iwamoto, R. Kojima, H. Tokieda, M. Dozono, S. Hayakawa, K. Kawata, N. Kitamura, S. Masuoka, R. Tsunoda, S. Michimasa, T. Gunji, N. Imai, H. Yamaguchi, Y. Mizoi, D. Suzuki, T. Isobe, J. Zenihiro, S. Nishimura, N. Zhang, K. Howard, T. Harada, T. Murakami</i>	
The Linear Polarization Sensitivity of CNS-GRAPE detector	43
<i>T.T. Pham, E. Ideguchi, N. Aoi, S. Miyamoto, M.R. Kumar, T. Vijiamaa, H.T. Hoang, A. Kohda, T. Shima, T. Shizuma, Y. Yamamoto, K. Sugita,</i>	
Development of a high density ^7Be beam at CRIB	45
<i>A. Inoue, A. Tamii, H. Yamaguchi, K. Abe, A. Adachi, S. Hayakawa, J. Isaak, N. Kobayashi, H. Shimizu, L. Yang</i>	
Study of spin-isospin responses of radioactive nuclei with the background-free neutron spectrometer, PANDORA	47
<i>L. Stuhl, K. Yako, M. Sasano, J. Gao, for the HIMAC H391 collaboration</i>	
Energy measurements with single crystal diamond detector at HIMAC	49
<i>O. Beliuskina, N. Imai, S. Michimasa, N. Kitamura, M. Dozono, C. Iwamoto, K. Kawata, S. Masuoka, S. Ota, H. Sakai, E. Takada, R. Tsunoda, K. Yako</i>	
Upgrade of the beam-orbit analysis method of RIKEN AVF Cyclotron injection line by four-dimensional emittance	51
<i>Y. Kotaka, Y. Ohshiro, H. Yamaguchi, N. Imai, Y. Sakemi, T. Nagatomo, J. Ohnishi, A. Goto, M. Kase, K. Hatanaka, H. Muto, S. Shimoura</i>	
Production of $^{56}\text{Fe}^{15+}$ ion beam by cylindrical material in Hyper ECR ion source	53
<i>Y. Ohshiro, Y. Kotaka, H. Muto, H. Yamaguchi, N. Imai, Y. Sakemi, S. Shimoura</i>	
3. Theoretical Nuclear Physics	
Variational Monte Carlo method for nuclear shell-model calculations	55
<i>N. Shimizu, T. Mizusaki</i>	
Double Gamow-Teller transitions in connection to $\beta\beta$ decay	57

<i>J. Menéndez, N. Shimizu, K. Yako</i>	
Nuclear studies for the direct detection of dark matter	59
<i>J. Menéndez, M. Hoferichter, P. Klos, A. Schwenk</i>	
Monte Carlo shell model calculations for shape staggering in Hg isotopes	61
<i>Y. Tsunoda, T. Otsuka</i>	
Ground-state properties from the unitary-model-operator approach	63
<i>T. Miyagi, T. Abe, M. Kohno, P. Navratil, R. Okamoto, T. Otsuka, N. Shimizu, S. R. Stroberg</i>	
A thermodynamical consideration on nuclear shell model	65
<i>N. Tsunoda, N. Shimizu</i>	

4. Other Activities

The 16th CNS International Summer School CNSSS17	67
<i>T. Ichikawa, N. Imai, T. Gunji, H. Liang, S. Michimasa, Y. Mizoi, S. Ota, T. Otsuka, H. Sakai, H. Sakurai, N. Shimizu, S. Shimoura, H. Ueno, T. Uesaka, Y. Utsuno, K. Yako, H. Yamaguchi</i>	
Laboratory Exercise for Undergraduate Students	69
<i>S. Ota, M. Niikura, R. Tsunoda, T. Koiwai, K. Yako, H. Sakurai, S. Shimoura</i>	

Appendices

Symposium, Workshop, Seminar, PAC and External Review	71
CNS Reports	72
Publication List	73
Talks and Presentations	82
Personnel	88

Experimental Nuclear Physics: Low and Intermediate Energies

Evaluation of the nuclear reaction of $^{79}\text{Se}(n, \gamma)$ via $^{79}\text{Se}(d, p)$ reaction at OEDO

N. Imai, M. Dozono, S. Michimasa, S. Ota, T. Sumikama^a, O. Beliuskina, S. Hayakawa, C. Iwamoto, K. Kawata, N. Kitamura, S. Masuoka, P. Schrock, H. Shimizu, S. Shimoura, K. Wimmer^b, K. Yako, H. Yamaguchi, L. Yang, N. Chiga^a, D. Nagae^a, S. Omika^a, H. Otsu^a, H. Sakurai^a, D. Suzuki^a, K. Yamada^a, S. Takeuchi^c, H. Miki^c, H. Yamada^c, S. Kawase^d, K. Nakano^d, Y. Watanabe^d, K. Iribe^e, T. Teranishi^e, N. Aoi^f, E. Ideguchi^f, H.J. Ong^f, R. Yanagihara^f

Center for Nuclear Study, Graduate School of Science, University of Tokyo

^a*RIKEN Nishina Center*

^b*Department of Physics, Univ. of Tokyo*

^c*Tokyo Institute of Technology*

^d*Department of Advanced Energy Science and Engineering, Kyushu Univ.*

^e*Department of Physics, Kyushu Univ.*

^f*RCNP, Osaka Univ.*

^{79}Se , which has a half-life as long as 3.3×10^5 years, is one of the long-lived fission products (LLFPs) of the nuclear wastes. It is supposed to be stored for millions of years in the deep geological repository, which has not been determined yet in Japan [1]. The ImPACT program aims to propose an alternative way to reduce the LLFPs by accelerator-driven transmutation. Among the nuclear reactions, generally, neutron-induced reaction is one of the effective ways to transmute the nuclei in terms of the cross section and the mean-free path of neutron due to its chargeless property. To design the facility for the transmutation, cross sections of any neutron induced reaction are demanded. However, because of the radioactivity and the chemical property of the selenium isotopes, the neutron-induced reactions such as (n, γ) and $(n, 2n)$ on ^{79}Se have never been measured.

The (n, γ) on ^{79}Se is also important astrophysically. The nucleus is located on the path of s process nucleosynthesis. ^{79}Se has an isomeric state at 95.8 keV, 0.06% of which β -decays to ^{79}Br . Because the black body radiation of the star can excite the ground state of ^{79}Se to the isomeric state, the isotope ratio of ^{79}Br to ^{80}Se can tell us the temperature [2]. The experimental cross section of $^{79}\text{Se}(n, \gamma)$ reaction is required for the precise determination of the temperature. We report here the evaluation of the (n, γ) reaction by using the (d, p) reaction.

In the present study, the cross section of $^{79}\text{Se}(n, \gamma)$ was evaluated with a surrogate technique [3]. The neutron capture reaction can be considered to be composed of two processes, the formation of the compound nucleus and the γ decay from the unbound states. The formation cross section can be determined by using the global optical potential. On the other hand, the probability of the γ decay depends on the nuclear structure of the nucleus. The surrogate technique depends on the Weisskopf-Ewing approximation of the Hauser-Feshbach theory which assumes that the decay probability from the unbound states of the compound nucleus is independent from the spin parity populated by the nuclear reactions. Under this assumption, the γ decay probability from the unbound states can be evaluated by other

nuclear reaction.

When the γ decay probability is determined by measuring γ rays, the γ decay schemes which is generally quite difficult to determine is assumed. There may be a chance in which the γ ray is emitted after the particle emission from the unbound state. In the Ref. [4], the number of transition of low lying state after neutron transfer reaction was used to determine the γ emission probability with the help of the theoretical γ decay scheme using the statistical model. On the other hand, our experiment determined the γ emission probability by identifying the reaction residue in coincidence with the recoiled particles without γ rays. Comparing the yields of ^{80}Se and ^{79}Se measured at the same excitation energy determined by the energy of recoiled protons can give the γ decay probability from the unbound state in ^{80}Se . The measurement was feasible due to the inverse kinematics.

In the experiment, the $^{77}\text{Se}(d, p)$ reaction was also measured separately. The $^{77}\text{Se}(n, \gamma)$ reaction was directly measured at 550 keV [5], which provides us to assess the cross section determined by the surrogate (d, p) reaction.

The secondary $^{77,79}\text{Se}$ beams were produced by the in-flight fission of ^{238}U beams with a rotating Be target of 3 mm thickness. By tuning the thicknesses of the degraders at F1 and F2 the beam energy was adjusted to 120 MeV/nucleon at F5. The beam energy was further degraded with a thick Al degrader at F5 at 23 MeV/nucleon to achieve 20 MeV/nucleon at the secondary target after passing through the beam line detectors. Diamond detectors of $3 \times 3 \text{ cm}^2$ and 300 μm thickness were placed at F3 and F5 to measure the timing when the beam passed through. The small active area of the diamond limited the momentum slit at F1 $\pm 1\%$. The parallel beam was made by the super conducting triplet quadrupole magnet at FE10, where the RF deflector is installed.

Two PPACs were installed upstream of the secondary target, FE12, to register the timing and the trajectory of the beams on the target. Time of flight (TOF) between F5 and FE12 was measured. Thanks to the high time resolution of

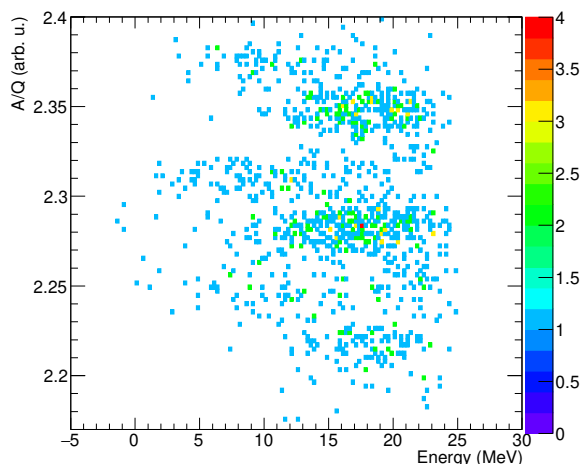


Figure 1. The charge-to-mass ratio of the outgoing nuclei obtained by the SHARAQ spectrometer as a function of the excitation energy of ^{80}Se for $^{79}\text{Se}(d,p)$ reaction in inverse kinematics. There seems to be nine loci which correspond to $^{78,79,80}\text{Se}$ with three different charge states.

diamond and PPACs, the beams were identified only with the TOF without measuring the energy loss to determine the atomic number. The RF deflector squeezed the beam spot in a diameter of 2 cm (σ) at a deuterated polyethylene CD_2 target of 4 mg/cm^2 . The recoiled particles of (d, p) reactions were detected by six telescopes, each of which consisted of SSD and two CsI(Tl)s detectors. The telescope covered the scattering angles from 100 to 150 degrees. The SSD was divided to 16 channels in angle. The momentum of the outgoing particles ^{80}Se was analyzed by the first part of the SHARAQ spectrometer. At the exit of the D1 magnet, two PPACs and an ionization chamber were installed as the focal plane detectors. PPACs gave the TOF of ions. The ionization chamber yielded the energy loss (dE) and the range in the gas. The TOF-dE-range and $B\rho$ information enables us to identify the ions.

Figure 1 shows the charge to mass ratio determined by the spectrometer as a function of the excitation energy obtained from the momenta of the recoiled protons for $^{79}\text{Se}(d, p)^{80}\text{Se}$ reaction. Three charge states of the outgoing nuclei were observed. Only the ^{80}Se were produced below 10 MeV, which is the one neutron separation energy of ^{80}Se , while ^{79}Se was also populated by one-neutron emission above the energy, demonstrating that the absolute missing mass energy was correct. Further analysis is on-going.

Acknowledgment

The work was funded by ImPACT Program of Council for Science, Technology and Innovation (Cabinet Office, Government of Japan).

References

- [1] <https://www.numo.or.jp/en/>.
- [2] F. Kappler, H. Beer, and K. Wisshak, Rep. of Prog. in Phys. 52, 945 (1989).

- [3] J. E. Escher et al., Rev. of Mod. Phys. 84, 353 (2012).
- [4] R. Hatrarik et al., Phys. Rev. C 81, 011602 (R) (2010).
- [5] S. Kawada, M. Igashira, T. Katabuchi, and M. Mizumoto, J. Nucl. Sci. Tech. 47, 643 (2010).

Proton- and deuteron-induced reactions on ^{107}Pd at 20 – 30 MeV/u

M. Dozono, N. Imai, S. Michimasa, T. Sumikama^a, N. Chiga^a, S. Ota, O. Beliuskina, S. Hayakawa, K. Iribe^b, C. Iwamoto, S. Kawase^c, K. Kawata, N. Kitamura, S. Masuoka, K. Nakano^c, P. Schrock, D. Suzuki^a, R. Tsunoda, K. Wimmer^d, D. S. Ahn^a, N. Fukuda^a, E. Ideguchi^e, K. Kusaka^a, H. Miki^f, H. Miyatake^g, D. Nagae^a, M. Nakano^h, S. Ohmika^a, M. Ohtake^a, H. Otsu^a, H. J. Ong^e, S. Sato^h, H. Shimizu, Y. Shimizu^a, H. Sakurai^a, X. Sun^a, H. Suzuki^a, M. Takaki, H. Takeda^a, S. Takeuchi^f, T. Teranishi^b, H. Wang^a, Y. Watanabe^c, Y. X. Watanabe^g, H. Yamada^f, H. Yamaguchi, R. Yanagihara^e, L. Yang, Y. Yanagisawa^a, K. Yoshida^a, and S. Shimoura

Center for Nuclear Study, the University of Tokyo

^a*RIKEN Nishina Center*

^b*Department of Physics, Kyushu University*

^c*Department of Advanced Energy Engineering Science, Kyushu University*

^d*Department of Physics, the University of Tokyo*

^e*Research Center for Nuclear Physics, Osaka University*

^f*Department of Physics, Tokyo Institute of Technology*

^g*WNSC, IPNS, KEK*

^h*Department of Physics, Rikkyo University*

Nucleon- and light-ion-induced reactions at low energies ranging from several keV to tens of MeV play an important role in nuclear physics and its applications. A prime example is understanding of the origin of elements in nature [1], which is one of the most difficult interdisciplinary challenges. Knowledge of nuclear cross sections is a crucial component to understand the synthesis of the heavy elements and identify the nucleosynthesis sites. Nuclear cross sections are also essential for nuclear-waste transmutation in nuclear reactors or accelerator-driven systems (ADS) [2] and the production of medical radioisotopes using cyclotrons [3]. Nuclear model calculations are frequently used to evaluate their cross sections, but the precise predictions are often difficult due to the complicated interplay between various reaction mechanisms such as compound, pre-equilibrium, and direct processes, and their unknown parameters, which have to be tuned to reproduce experimental data. Thus, many areas of basic and applied nuclear physics require relevant nuclear reaction data.

Experimentally, an activation method with nucleon and light-ion beams has been applied [4], but the method is only detectable to unstable reaction products (emitting γ -rays). Furthermore, the method reaches its limit once short-lived or highly radioactive targets are of interest. One possible approach to overcome these limitations is an inverse kinematics method, in which a light target is bombarded by accelerated heavy nuclei. The method allows the direct detection of reaction products, and thus provides a complete set of residue production cross sections. The approach can be also matched with the radioactive-isotope (RI) beam experiments; thus, many reactions involving unstable nuclei that are related to basic and applied nuclear physics can be studied.

Among many projects of RI beam facilities around the world, the “Optimized Energy-Degrading Optics” (OEDO) project [5], which began operation in March 2017 at RIKEN

RI Beam Factory (RIBF), is a suitable one to study low-energy reactions on unstable nuclei for the following reasons. First, the new beamline is capable of decelerating fast RI beams of RIBF down to energies of 5 – 50 MeV/nucleon with a well-focused condition. Second, the beamline can be used in combination with the magnetic spectrometer SHARAQ [6, 7], which allows the identification of all the isotopes produced in nuclear reactions. Using the setup, we performed an experiment to obtain new data related to the transmutations of long-lived fission products (LLFPs): proton- and deuteron induced reaction measurements on ^{107}Pd and ^{93}Zr at 20 – 30 MeV/u. This report describes the current status of the analysis on ^{107}Pd data. The status of the ^{93}Zr data analysis is reported by Iribe *et al.* [8].

Details of the experimental setup and procedure can be found in Ref. [8]. A secondary beam was produced by the in-flight fission of a ^{238}U primary beam at 345 MeV/u on a Be target with a thickness of 5 mm. The beam was degraded and purified by using an Al degrader at the focus F1 and further degraded by using another Al degrader at F5. The purity of ^{107}Pd was 37%, and its energy was 32 MeV/u in front of the secondary target. Another setting was used to study the reaction at a lower beam energy of 26 MeV/u. The OEDO device [5], which consists of a radio-frequency deflector and two superconducting triplet quadrupole magnets, was employed to reduce the beam spot size, and the resulting size was 45 mm in FWHM on the secondary target. The typical beam intensity was 10^4 pps.

The secondary targets, H_2 and D_2 , were prepared as high-pressure cooled gas targets. The temperature was 40 K, and the pressure was adjusted to 7.5(15) mg/cm² for H_2 (D_2). In order to obtain the background contribution, empty-target measurements were also carried out.

Reaction residues were analyzed by the SHARAQ spectrometer and detected by two PPACs [9] and an ionization chamber [10] located at the focal plane. Position and tim-

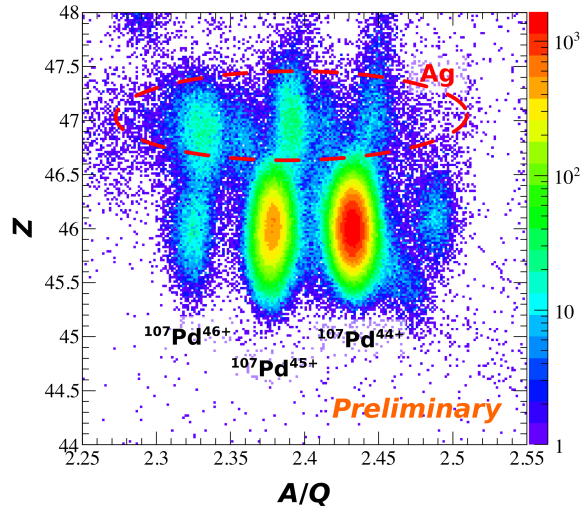


Figure 1. Correlation of atomic number Z and mass-to-charge ratio A/Q of reaction residues produced from a ^{107}Pd beam at 32 MeV/u and a H_2 target.

ing information of PPACs were used to deduce the velocity (β) and magnetic rigidity ($B\rho$). The ionization chamber measured the energy loss (ΔE) and range (R). The mass-to-charge ratio A/Q , atomic number Z , and mass number A , were obtained from $B\rho - \beta$, $\Delta E - \beta$, and $R - \beta$ correlations, respectively. In order to cover a broad range of reaction products, several different $B\rho$ settings were applied in SHARAQ.

Correlation of Z and A/Q for reaction products produced from a ^{107}Pd beam at 32 MeV/u and a H_2 target is shown in Fig. 1. The present resolutions in Z and A/Q were $\sigma(Z) = 0.4$ and $\sigma(A/Q) = 7 \times 10^{-3}$, respectively. In addition to the ^{107}Pd beam events, Ag isotope events are seen. Because the present Z and A/Q resolutions are worse than expected values ($\sigma(Z) = 0.25$ and $\sigma(A/Q) = 4.5 \times 10^{-3}$), further analysis is being examined to improve the resolutions. Analysis for mass number A reconstruction is also in progress. After the particle identification, isotopical production cross sections will be extracted.

This work was funded by the ImPACT Program of the Council for Science, Technology and Innovation (Cabinet Office, Government of Japan).

References

- [1] A. Arcones *et al.*, Prog. Part. Nucl. Phys. **94** (2017) 1.
- [2] Implication of Partitioning and Transmutation in Radioactive Waste Management, IAEA Technical Reports Series No. 435, 2004.
- [3] S. M. Qaim, Radiochim. Acta **100** (2012) 635.
- [4] Handbook on Nuclear Activation Data, IAEA Technical Reports Series No. 273, 1987.
- [5] S. Michimasa *et al.*, CNS Annual Report 2017, CNS-REP-97 (2019) 37 - 38.
- [6] T. Uesaka *et al.*, Prog. Theor. Exp. Phys. **2012** (2012) 03C007.
- [7] M. Dozono *et al.*, Nucl. Instrum. Methods Phys. Res. A **830** (2016) 233.

- [8] K. Iribe *et al.*, CNS Annual Report 2017, CNS-REP-97 (2019) 5 - 6.
- [9] H. Kumagai *et al.*, Nucl. Instrum. Methods Phys. Res. B **317** (2013) 717.
- [10] N. Chiga *et al.*, RIKEN Accel. Prog. Rep. **50** (2017) 164.

Study of proton- and deuteron-induced reactions on the long-lived fission product ^{93}Zr at 30 MeV/u in inverse kinematics

K. Iribe, M. Dozono^a, N. Imai^a, S. Michimasa^a, T. Sumikama^b, N. Chiga^b, S. Ota^a, O. Beliuskina^a, S. Hayakawa^a, C. Iwamoto^a, S. Kawase^c, K. Kawata^a, N. Kitamura^a, S. Masuoka^a, K. Nakano^c, P. Schrock^a, D. Suzuki^b, R. Tsunoda^a, K. Wimmer^d, D. S. Ahn^b, N. Fukuda^b, E. Ideguchi^e, K. Kusaka^b, H. Miki^f, H. Miyatake^g, D. Nagae^b, M. Nakano^h, S. Ohmika^b, M. Ohtake^b, H. Otsu^b, H. J. Ong^e, S. Sato^h, H. Shimizu^a, Y. Shimizu^b, H. Sakurai^b, X. Sun^b, H. Suzuki^b, M. Takaki^a, H. Takeda^b, S. Takeuchi^f, T. Teranishi, H. Wang^b, Y. Watanabe^c, Y. X. Watanabe^g, H. Yamada^f, H. Yamaguchi^a, R. Yanagihara^e, L. Yang^a, Y. Yanagisawa^b, K. Yoshida^b, and S. Shimoura^a

Department of Physics, Kyushu University

^a*Center for Nuclear Study, the University of Tokyo*

^b*RIKEN Nishina Center*

^c*Department of Advanced Energy Engineering Science, Kyushu University*

^d*Department of Physics, the University of Tokyo*

^e*Research Center for Nuclear Physics, Osaka University*

^f*Department of Physics, Tokyo Institute of Technology*

^g*WNSC, IPNS, KEK*

^h*Department of Physics, Rikkyo University*

The nuclear transmutation [1] of long-lived fission products (LLFPs), which are produced in nuclear reactors, is one of the candidate techniques for the reduction and/or reuse of LLFPs. To design optimum pathways of the transmutation process, several nuclear reactions have been studied by using LLFPs as secondary beams. The studies indicate that proton- and/or deuteron-induced spallation reactions at intermediate energy (100 – 200 MeV/u) are sufficiently effective for the LLFP transmutation [2–4].

Measurements at lower reaction energies for both proton- and deuteron-induced reactions would be highly desirable to design an accelerator-driven transmutation system, because proton and deuteron beams lose their energies in the waste materials. For this purpose, we performed an experiment of proton- and deuteron-induced reactions on ^{107}Pd and ^{93}Zr at 20 – 30 MeV/u at RIKEN RI Beam Factory (RIBF). The inverse kinematics technique was adopted in the present work: radioactive isotope (RI) beams of ^{107}Pd and ^{93}Zr were used and proton/deuteron-induced reactions were conducted using proton and deuteron targets. The technique allows us to identify unambiguously reaction products for residue production cross section measurements. In addition, the technique avoids the difficulties associated with using a highly radioactive target. The new beamline OEDO [5] was employed to produce low-energy LLFP beams. This was the first physics experiment with OEDO. In this report, the current status of the analysis on ^{93}Zr data is described. The status of the ^{107}Pd data analysis is reported by Dozono *et al.* [6].

The experimental setup is shown in Fig. 1. A secondary beam was produced by the in-flight fission of a ^{238}U primary beam at 345 MeV/u on a 5-mm-thick ^9Be target located at the object point F0 of the BigRIPS fragment separator. The beam was selected and purified at the focus

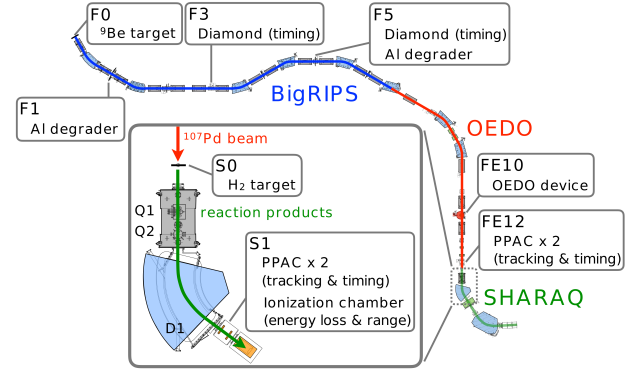


Figure 1. Schematic of the experimental setup.

F1 by placing an aluminum wedge and setting the momentum slit to $\pm 0.15\%$. Figure 2 shows the mass-to-charge ratio A/Q distribution for the beam, which was deduced from the time-of-flight (TOF) between F3 and F5 measured with CVD diamond detectors [7]. The A/Q resolution was $\sigma(A/Q) = 3 \times 10^{-3}$. We can see that the beam contains only $N = 53$ isotones and the ^{93}Zr particle is clearly separated from other particles. The purity of ^{93}Zr was 33.9%.

The beam was further decelerated at F5 by using an aluminum energy degrader, and focused employing the OEDO device [5], which consists of a radio-frequency deflector and two superconducting triplet quadrupole magnets. The beam energy was measured with the TOF between F5 and FE12, and its image was measured with parallel-plate avalanche counters (PPACs) [8] located at FE12. The resulting ^{93}Zr beam had an energy of 32 MeV/u and a spatial spread of 45 mm (FWHM) at the secondary target position S0. The typical beam intensity was 10^4 pps.

H_2 and D_2 gas targets were placed at S0 to induce the

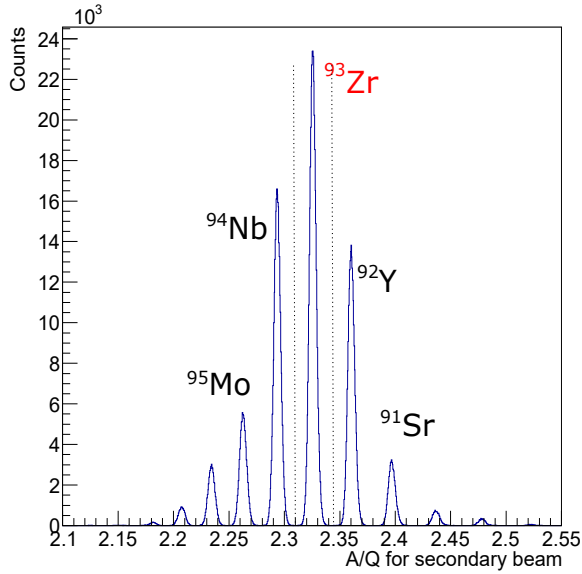


Figure 2. mass-to-charge ratio A/Q distribution for secondary beam.

secondary reactions. The targets were operated at a temperature of 40 K and a pressure of 2.2 atm, resulting in a thickness of $7.5(15) \text{ mg/cm}^2$ for H_2 (D_2). The gas cell windows were made of $10\text{-}\mu\text{m}$ -thick Harvar foil. Empty-target measurements were also carried out to obtain the contributions from both the Harvar foils and the PPACs at FE12.

Reaction residues were momentum analyzed and identified by the first half (QQD; which consists of two quadrupole magnets and one dipole magnet) of the SHARAQ spectrometer [9, 10]. The full momentum acceptance is 8% and the angular acceptance is ± 30 mrad for both horizontal and vertical directions. The particles were detected by two PPACs and an ionization chamber [11] located at the focal plane S1. The magnetic rigidity ($B\rho$) and TOF, which were deduced from the position and timing information of the PPACs at S0 and S1, provided the mass-to-charge ratio A/Q . The ionization chamber measured the Bragg curve along the beam axis, which helped determine the atomic number Z and mass number A . In order to cover a broad energy range of reaction products, several different $B\rho$ settings were applied in the SHARAQ spectrometer. The settings were $\Delta(B\rho)/B\rho = -9.5\%$, -5.5% , -1.5% , $+2.5\%$, and $+6.5\%$ relative to the peak of the $B\rho$ distribution for the fully stripped ^{93}Zr beam.

Figure 3 shows two-dimensional plot of the horizontal position at S1 and the TOF between FE12 and S1 for the H_2 target and $\Delta(B\rho)/B\rho = -1.5\%$ run. Apparently, these quantities have A/Q information; the beam events are separated into different charge states. The events in the red circle may be reaction residues produced from the $^{93}\text{Zr} + p$ reaction. Further analysis for A/Q reconstruction is in progress. After the reconstruction, data from the ionization chamber will be analyzed.

This work was funded by the ImPACT Program of the Council for Science, Technology and Innovation (Cabinet

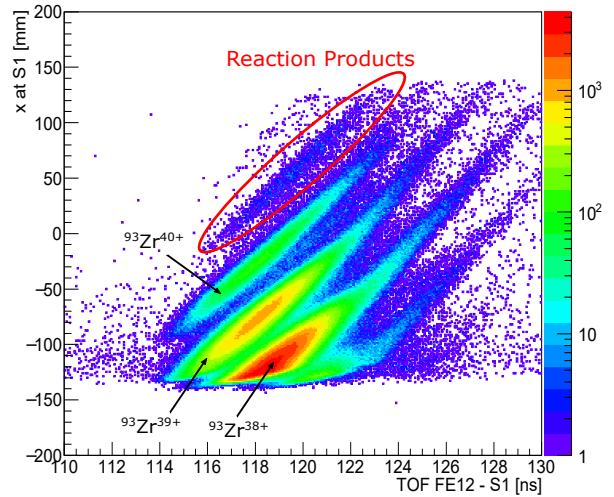


Figure 3. Two-dimensional plot of the horizontal position at S1 and the TOF between FE12 and S1 for the H_2 target and $\Delta(B\rho)/B\rho = -1.5\%$ run.

Office, Government of Japan).

References

- [1] Implication of Partitioning and Transmutation in Radioactive Waste Management, IAEA Technical Reports Series No. 435, 2004.
- [2] H. Wang *et al.*, Phys. Lett. **B754** (2016) 104.
- [3] H. Wang *et al.*, Prog. Theor. Exp. Phys. **2017** (2017) 021D01.
- [4] S. Kawase *et al.*, Prog. Theor. Exp. Phys. **2017** (2017) 093D03.
- [5] S. Michimasa *et al.*, CNS Annual Report 2017, CNS-REP-97, 37, 2019
- [6] M. Dozono *et al.*, CNS Annual Report 2017, CNS-REP-97, 3, 2019
- [7] S. Michimasa *et al.*, Nucl. Instrum. Methods Phys. Res. B **317** (2013) 710.
- [8] H. Kumagai *et al.*, Nucl. Instrum. Methods Phys. Res. B **317** (2013) 717.
- [9] T. Uesaka *et al.*, Prog. Theor. Exp. Phys. **2012** (2012) 03C007.
- [10] M. Dozono *et al.*, Nucl. Instrum. Methods Phys. Res. A **830** (2016) 233.
- [11] N. Chiga *et al.*, RIKEN Accel. Prog. Rep. **50** (2017) 164.

Development of a tritium loaded target for reaction studies at the RIBF

K. Wimmer^a, P. Schrock^b, Y. Beaujeault-Taudiere^c, Y. Hatano^d, N. Imai^b, K. Iribe^e, N. Kitamura^b, P. Shi^d, D. Suzuki^f, and T. Teranishi^e

^a Department of Physics, University of Tokyo

^b Center for Nuclear Study, University of Tokyo

^c Universite Paris-Saclay

^d Hydrogen Isotope Science Center, Toyama University

^e Kyushu University

^f RIKEN Nishina Center

A unique feature of many-body quantum-systems is the occurrence of shape coexistence. Several regions of shape coexistence are known in the nuclear chart [1]. However, understanding the origin of shape coexistence in atomic nuclei presents still one of the greatest challenges for nuclear structure theory.

A unique tool to study shape coexistence in atomic nuclei are two-nucleon transfer reactions. They selectively populate $J^\pi = 0^+$ states, which are the ground state configurations of the respective shapes. Transfer reactions with radioactive beams pose a challenge as they have to be performed in inverse kinematics, requiring the probe to be the target nucleus. For two-neutron transfer reaction, the ideal target is tritium, due to its simple structure and large neutron excess. However, the use of a radioactive target requires special attention for safety and radio-protection matters. The approach considered here, and elsewhere [2] is based on a self-supporting tritium-loaded titanium foil. Special requirements at the RIBF are the large area of the target, due to the beam spot size compared to typical ISOL facilities, as well as the contamination of the target with other nuclei, either in the Ti matrix or on the surface of the target.

celerator at Kyushu University. The target was surrounded by the first implementation of the TINA array for transfer reactions at OEDO [4]. This array of silicon strip detectors was covering scattering angles $\theta_{\text{lab}} = 28 - 78^\circ$ in the laboratory system. Five deuterated Ti foils were irradiated for about one hour each, and elastically scattered deuterons and protons were detected as shown in Fig. 1. For background subtraction and investigation of surface contaminations a pure Ti target was also irradiated. The targets had nominal thicknesses of 2 and 5 μm and were produced under different temperature and pressure conditions as discussed in [3]. One of the targets showed a significantly deteriorated resolution for the excitation energy, which is attributed to the flatness of the target. During production the target were typically sandwiched between two layers of porous Al_2O_3 . As deuterium penetrates the Ti matrix, it is partially converted to TiD_2 , leading to an expansion of the volume. Target 2 was not sandwiched and therefore wavy (see Fig. 2) after deuterium loading which changed the effective thickness for the in-beam experiment.

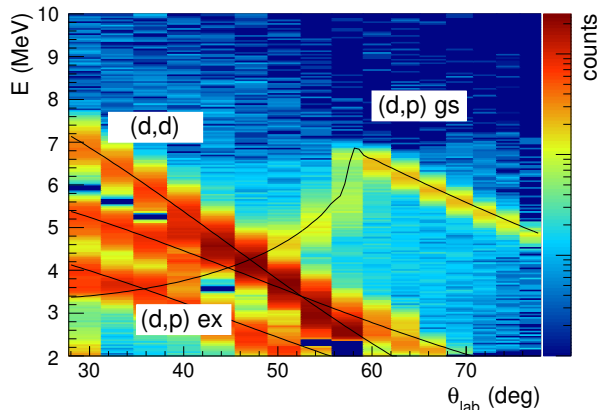


Figure 1. Kinematics correlation of energy versus laboratory scattering angle θ_{lab} for the $d(^{12}\text{C}, p)$ reaction at 20 MeV. (d, p) transfer and (d, d) elastic scattering can be clearly identified.

After initial tests with deuterated prototype targets at the AVF, further prototypes of large area deuterated foils have been produced at Toyama University [3]. The targets were characterized using a 20 MeV ^{12}C beam at the tandem ac-



Figure 2. Photograph of target 2, showing the volume expansion after loading with deuterium.

References

- [1] K. Heyde and J. L. Wood, Rev. Mod. Phys. **83** (2011) 1467.
- [2] K. Wimmer et al., Phys. Rev. Lett. **105** (2010) 252501, K. Nowak, et al., Phys. Rev. C **93** (2016) 044335, K. Wimmer et al., TRIUMF experiments 1481, 1633.
- [3] T. Koiwai et al., CNS annual report 2016.
- [4] P. Schrock et al., CNS annual report 2016.

Characterization of a tritium-loaded titanium target through elastic scattering on ^{94}Sr and ^{84}Kr

N. Kitamura, K. Wimmer^a, P. C. Bender^b, G. Hackman^b, J. Henderson^b, N. Imai

Center for Nuclear Study, Graduate School of Science, University of Tokyo

^aDepartment of Physics, University of Tokyo

^bTRIUMF

Two-neutron transfer reactions are a well-suited tool to study pairing correlations and shape coexistence phenomena. In particular, two-neutron transfer reactions induced by triton, namely (t, p) reactions, are ideal for studies of neutron-rich nuclei because of the simple structure and the neutron excess of the triton. (t, p) reactions on unstable nuclei pose an experimental challenge; the reactions have to be performed in inverse kinematics requiring a radioactive tritium target. Only few (t, p) experiments have been conducted at radioactive beam facilities using targets based on a tritium-loaded titanium foil or a gaseous tritium cell [1–3]. Recently, TRIUMF has acquired a tritium-loaded titanium target¹, opening up possibilities to perform (t, p) reactions at the ISAC-II facility [4]. For the planning of future experiments [5,6], an elastic scattering measurement has been performed to measure the absolute tritium content of the target.

A beam of ^{94}Sr at 6 MeV/nucleon provided by the ISAC-II facility was directed onto the tritium target at the experimental station. SHARC, the Silicon Highly-segmented Array for Reactions and Coulex [7], surrounded the target to detect scattered light particles. The species of light particles recoiling from the target were identified by the ΔE - E method and cuts on the ΔE - E plane allowed for the extraction of scattered tritons and protons. By gating on these tritons and protons, the angular distributions of elastic scattering were obtained (see Figure 1). Note that the elastically scattered protons arise most likely from surface contamination of the target.

A first attempt to deduce the number density of tritium was made with global nucleus-triton optical-model parameterizations [8–10]. However, all of them failed to reproduce the measured angular distribution. For a better reproduction, the optical-model parameters were adjusted by fitting, and the normalization factor of the data points was treated as a free parameter. The resulting optical-model calculation is shown in Figure 2, together with calculations employing global optical-model parameters. Finally, the number of target nuclei was deduced by comparing the measured angular distribution and the calculated cross section. As shown in Figure 3, the resulting tritium thickness amounts to $2 \times 10^{18} \text{ cm}^{-2}$, while the (normal) hydrogen thickness is $2 \times 10^{17} \text{ cm}^{-2}$, which is 10% of the tritium concentration. The systematic error is estimated to be 30%, considering the uncertainty in the optical-model parameters and in the normalization of the total beam flux. The tritium thickness is roughly in agreement with, but less than the design value

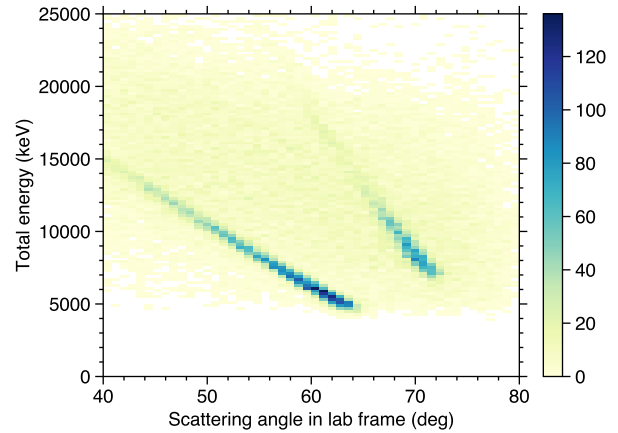


Figure 1. Kinematics curves of triton/proton elastic scattering on ^{94}Sr . The continuous background mostly comes from fusion-evaporation reactions with titanium.

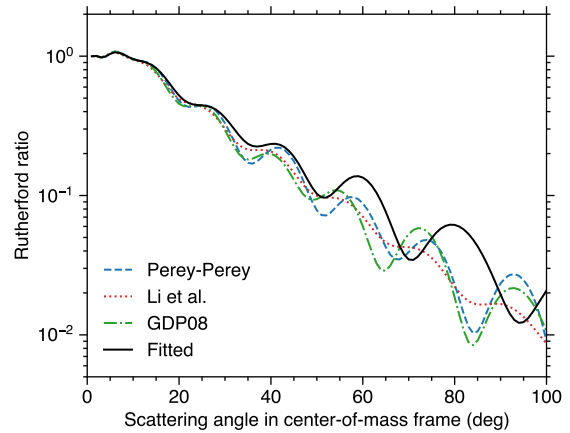


Figure 2. Elastic-scattering differential cross sections in comparison with Rutherford scattering for calculations using the Perey-Perey (dashed), Li *et al.* (dotted), and GDP08 (dashed-dotted) global parametrizations, and the fitted optical-model parameters (solid).

of $6 \times 10^{18} \text{ cm}^{-2}$ (corresponding to $10 \text{ GBq } \mu\text{m}^{-1} \text{ cm}^{-2}$) provided by the manufacturer. The origin of the low concentration remains to be understood.

As reported before [11], utilizing a data set taken with a ^{84}Kr beam at 6 MeV/nucleon the tritium thickness of the same target was estimated as $4 \times 10^{18} \text{ cm}^{-2}$ without adjusting the optical-model parameters. As the fit largely impacts on the thickness estimation, the same analysis was

¹Produced by Sodern (France).

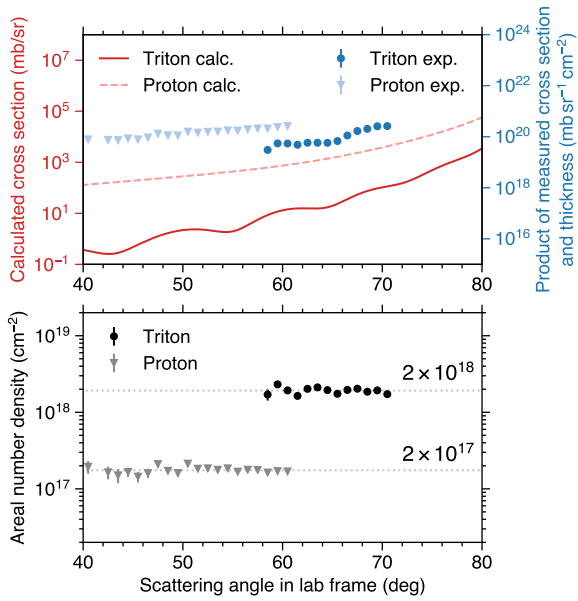


Figure 3. Differential cross sections of elastic scattering on ^{94}Sr (in arbitrary units) in comparison with optical-model calculations (top panel). Number densities of hydrogen and tritium deduced by scaling the experimental cross sections to the optical-model calculations (bottom panel).

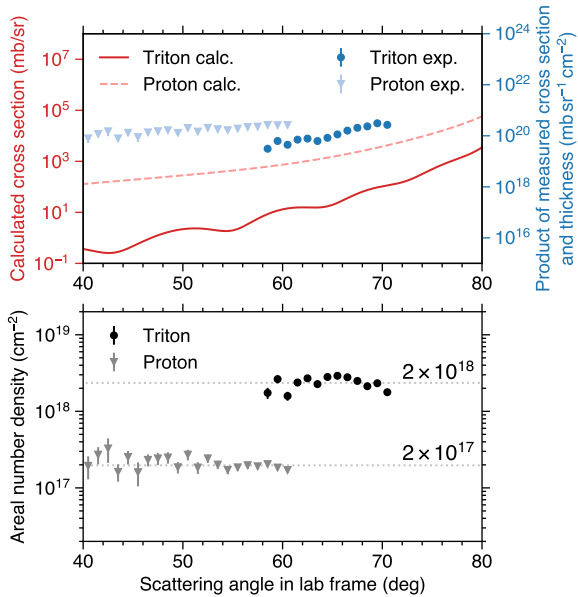


Figure 4. Same as Figure 3, but with the ^{84}Kr data.

performed for the ^{84}Kr data set. As shown in Figure 4, this analysis led to a tritium thickness of $2 \times 10^{18} \text{ cm}^{-2}$, providing a cross-check of this approach.

In conclusion, a new tritium-loaded titanium target at TRIUMF was evaluated by measuring elastic scattering on ^{94}Sr . The target thickness was deduced by comparing the measured cross section and the calculation using the fitted optical-model parameters. An updated analysis of the data set taken with a ^{84}Kr beam also gave the same target thickness. Although the thickness was found to be less than the

design value provided by the manufacturer, the target can still work for (t, p) studies and is ready for future experiments.

References

- [1] M. S. Golokov *et al.*, Phys. Lett. B **672**, 22 (2009).
- [2] K. Wimmer *et al.*, Phys. Rev. Lett. **105**, 252501 (2010).
- [3] K. Nowak *et al.*, Phys. Rev. C **93**, 044335 (2016).
- [4] G. C. Ball *et al.*, Phys. Scr. **91**, 093002 (2016).
- [5] P. C. Bender *et al.*, “Shape evolution towards $N = 60$: characterization of 0^+ states by two-neutron transfer reactions”, TRIUMF approved proposal S1481 (2015).
- [6] A. O. Macchiavelli *et al.*, “Pairing vibrations beyond $N = 82$ ”, TRIUMF approved proposal S1633 (2016).
- [7] C. Aa. Diget *et al.*, J. Instrum. **6**, P02005 (2011).
- [8] C. M. Perey and F. G. Perey, At. Data Nucl. Data Tables **17**, 1 (1976).
- [9] D. Y. Pang *et al.*, Phys. Rev. C **79**, 024615 (2009).
- [10] X. Li *et al.*, Nucl. Phys. A **789**, 103 (2007).
- [11] N. Kitamura *et al.*, CNS Annual Report **2016**, 47 (2018).

The measurement of proton resonance scattering on ^{118}Sn

R. Tsunoda, N. Imai, K. Iribe^a, S. Sakaguchi^a, T. Teranishi^a, K. Ueno^a

Center for Nuclear Study, Graduate School of Science, University of Tokyo

^aDepartment of Physics, Kyushu Univ.

In some atomic nuclei, states which have the different shapes are degenerate in low excitation energy, which is called shape coexistence [1]. As a result of the shape coexistence, in the case of the even-even nuclei, the second 0^+ (0_2^+) state appears in the low-excited state. The phenomenon is considered to be caused by the variation of the shell gap and the residual interaction to across the gap, i.e. $2p - 2h$ excitation cross $Z = 40$ and 50 shell gaps for zirconium (Zr) and tin (Sn) isotopes, respectively.

In the framework of the shell model, as the residual interaction the monopole term of the tensor interaction between protons and neutrons in a nucleus is considered to play an important role to make the neutron configuration changes as the proton number varies. In accordance with the change of the neutron single particle energies, the gap of the proton lowers, which promotes the neutron energies further. The mechanism of the change of the shell structure is named as Type-II shell evolution [2]. The model reproduces the sudden onset of the deformation in Zr isotopes between $N = 58$ and 60 [3]. In addition, it predicts that shape coexistence in the Zr isotopes heavier than $N = 52$.

To trace the variation of the neutron single particle energies experimentally, the respective single particle structure coupled to either 0^+ states needs to be measured. However, because the lifetime of the 0_2^+ state is generally too short to survive as a beam, measuring one neutron transfer reaction on the 0_2^+ is not feasible. The neutron single particle state can also be studied via the isobaric analog resonances (IARs) of even-odd nuclei. In a neutron-rich nucleus $^A Z$, the IAR appears in the high excited states in the neighboring nucleus $^A(Z-1)$. More important point here is that the decay from the IAR to the 0_2^+ state can tell us the single particle structure coupled to the 0_2^+ state. As an example, the inelastic decay to the 0_2^+ state in ^{90}Zr from the isobaric analog resonances of the ^{91}Zr isotopes reveals that the three excited states in ^{91}Zr have large spectroscopic factors relative to the 0_2^+ state [4, 5]. The energy spacing of the states are almost identical to those of the states coupled to the $0_{g.s.}^+$ state, suggesting that the shape of the 0_2^+ state is also spherical. Whereas, in the case of ^{94}Zr , the inelastic decay from the IARs of ^{95}Zr to the 0_2^+ state in ^{94}Zr reveals the single particle states with the same order of those for ^{95}Zr , suggesting that the shape of the 0_2^+ state in ^{94}Zr is also spherical unlike the result of the shell model mentioned above [6]. Before going to the studies of the neutron-rich Zr isotopes, it is demanded that the inelastic decay can be employed to study the shape coexistence structure.

The picture of the shape coexistence is well established in even-even tin isotopes. Indeed, the deformed bands above the 0_2^+ states have been observed [7]. However the inelastic channel to the 0_2^+ from the IARs have not been studied. To

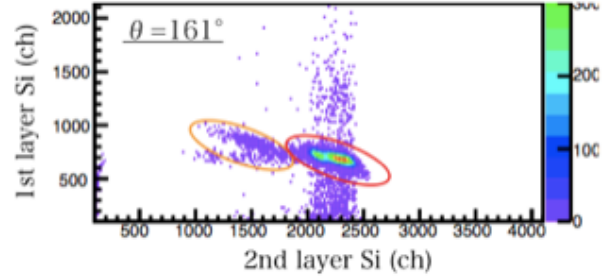


Figure 1. The energy correlation between the first layer SSD and the second layer SSD. The red circle indicates the elastic channel of ^{118}Sn and the orange one indicates the elastic channel of ^{16}O .

apply the inelastic channel measurement from the IAR to the neutron-rich Zr isotopes, we start a project to study the inelastic channel to the 0_2^+ state in Sn isotopes.

In the experiment, the excitation energy of the proton resonance scattering will be measured by changing the proton energy with a small step, i.e. about several keV. To establish an experimental method to measure the excitation function, we conducted an experiment of the isobaric analog resonances of ^{119}Sn . The elastic channel from IARs of ^{119}Sn were measured [8,9] in the past. The experiment aims to evaluate the systematic uncertainty of the experiment by comparing the experimental result to the past data.

The experiment was carried out at the tandem accelerator facility of Kyushu University. This was the first measurement to scan the excitation function in the facility. The typical proton beam intensity was about 0.3 enA. The beam energy was changed from 7.04 MeV to 7.58 MeV with a 20 keV step. The beam was impinged on an enriched ^{118}Sn target of 2.2 mg/cm². The beam intensity was measured with a Faraday cup which was 50 cm downstream of the target. The scattered protons were measured by a three layers SSD telescope, which consisted a pad-type SSD 50×50 mm² of 140 μm thickness and two sector-shaped single-stripped SSDs of 300 μm thicknesses. The inner diameter of the stripped SSD was 5 cm and the outer diameter was 13 cm. They were 16 electrodes of 5 mm width. The telescope placed at 15 cm upstream of the target covered from 140 to 160 degrees in the laboratory frame. The energy correlation measured with the first two layers at 161 degrees in the laboratory frame was presented in Fig. 1.

Figure 2 demonstrates the excitation function of the elastic scattering around IARs of low-excited states of ^{119}Sn . The R-matrix curve calculated with the resonance parameters of Ref. [8] was also shown as a dashed line. The energy shift was evaluated to be 50 keV by shifting the theoretical excitation function in energy to make a best fitting. By tak-

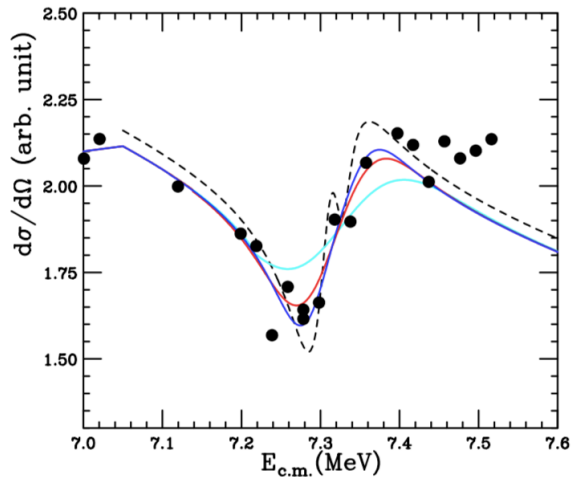


Figure 2. The excitation function of proton elastic scattering on ^{118}Sn at 150 degrees in the laboratory frame as a function of the center of mass energy. The dashed line indicate the R-matrix curve calculated with the resonance parameters [8]. The cyan, red and blue curves indicate the calculation convoluted with the 55, 30 and 20 keV energy resolution in σ .

ing into account the energy loss in half of the target, 30 keV, 20 keV was adopted as the systematic error. The excitation function was folded with three energy uncertainties, 20, 30, 55 keV as presented in Fig. 2. The 30 keV energy resolution, which was dominated by the reaction point in the target, reproduces the experimental data.

The transmission of the proton beam was about 20% in the worst case. Several other problems were found in the experiment, such as the readout of Faraday cup and the lack of the momentum slit in the beam line. They will be dealt with before the measuring the inelastic scattering in 2018.

References

- [1] K. Heyde and J. L. Wood, Rev. of Mod. Phys. **83**, 1467 (2011).
- [2] T. Otsuka and Y. Tsunoda, J. of Phys. G **43**, 024009 (2016).
- [3] T. Togashi, Y. Tsunoda, T. Otsuka, and N. Shimizu, Phys. Rev. Lett. **117**, 172502 (2016).
- [4] C. F. Moore, S. A. A. Zaidi, and J. J. Kent, Phys. Rev. Lett. **18**, 345 (1967)
- [5] K. P. Lieb, J. J. Kent, and C. F. Moore, Phys. Rev. **175**, 1482 (1968).
- [6] T. Hausmann and K. P. Lieb, Phys. Rev. Lett. **23**, 137-139 (1969)
- [7] J. L. Wood, K. Heyde, W. Nazarewicz, M. Huyse, and P. van Duppen, Physics Reports **215**, 101-201 (1992).
- [8] P. Richard, C. F. Moore, J. A. Becker and J. D. Fox, Phys. Rev. **145**, 971 (1966).
- [9] L. Veesser and J. Ellis, Nucl. Phys. **A115**, 185-192 (1968).

Cross sections of the ${}^7\text{Be} + n$ reactions relevant to the cosmological Li problem

S. Hayakawa^a, M. La Cognata^b, L. Lamia^{b,c}, H. Shimizu^a, L. Yang^a, H. Yamaguchi^a, K. Abe^a, O. Beliuskina^a, S. M. Cha^d, K. Y. Chae^d, S. Cherubini^{b,c}, P. Figuera^{b,c}, Z. Ge^e, M. Gulino^{b,f}, J. Hu^g, A. Inoue^h, N. Iwasaⁱ, D. Kahl^j, A. Kim^k, D. H. Kim^k, G. Kiss^e, S. Kubono^{a,e,g}, M. La Commara^{l,m}, M. Lattuada^{b,c}, E. J. Lee^d, J. Y. Moonⁿ, S. Palmerini^{o,p}, C. Parascandolo^m, S. Y. Park^k, D. Pierroutsakou^m, R. G. Pizzone^{b,c}, G. G. Rapisarda^b, S. Romano^{b,c}, C. Spitaleri^{b,c}, X. D. Tang^g, O. Trippella^{o,p}, A. Tumino^{b,f}, P. Vi^e, and N. T. Zhang^g

^aCenter for Nuclear Study, Graduate School of Science, University of Tokyo

^bIstituto Nazionale di Fisica Nucleare - Laboratori Nazionali del Sud

^cDepartment of Physics and Astronomy, University of Catania

^dDepartment of Physics, Sungkyunkwan University

^eRIKEN Nishina Center

^fFaculty of Engineering and Architecture, Kore University of Enna

^gInstitute of Modern Physics, Chinese Academy of Sciences

^hResearch Center for Nuclear Physics, Osaka University

ⁱDepartment of Physics, Tohoku University

^jSchool of Physics and Astronomy, University of Edinburgh

^kDepartment of Physics, Ewha Womans University

^lDepart. of Phys. 'E. Pancini', University of Naples Federico II

^mIstituto Nazionale di Fisica Nucleare - Section of Naples

ⁿInstitute for Basic Science (IBS)

^oIstituto Nazionale di Fisica Nucleare - Section of Perugia

^pDepartment of Physics and Geology, University of Perugia

We have performed indirect measurements of the ${}^7\text{Be}(n,p){}^7\text{Li}$ and the ${}^7\text{Be}(n,\alpha){}^4\text{He}$ reactions by means of the Trojan Horse Method (THM) [1] at Center for Nuclear Study Radioactive Isotope Beam separator (CRIB) [2], relevant to the cosmological ${}^7\text{Li}$ problem [3] in the Big-bang nucleosynthesis (BBN). Those two reactions are responsible for reduction of the ${}^7\text{Li}$ abundance in the BBN, which intend to reduce the discrepancy between its observation and prediction. Here we report the progress of the data analysis from the previous report [4] that summarizes details about the scientific motivation, the experimental method, and preliminary results such as the validity of the energy and position calibration of the position sensitive silicon detectors, consistency of the kinematics, and identification of the observed three-body channels.

Based on the above preliminary works, we confirmed that the momentum distributions of the spectator proton in the exit three-body channels are consistent with that of the well-known p - n intercluster motion inside the deuteron nucleus expressed by the Hulthén function in momentum space [1], both for the ${}^7\text{Be}(d,{}^7\text{Li}p){}^1\text{H}$ and the ${}^7\text{Be}(d,2\alpha){}^1\text{H}$ data. This guarantees the quasifree mechanism is dominant through the reaction process, especially in the low momentum region $|p_s| < 60$ MeV/ c .

Then we successfully extracted p_0 and p_1 yield separately by fitting Gaussian functions to the Q -value spectra with dividing center-of-mass energy into small bins. Preliminary cross sections as functions of the center-of-mass energy of the ${}^7\text{Be}(n,p_0){}^7\text{Li}$, ${}^7\text{Be}(n,p_1){}^7\text{Li}^*$ and the

${}^7\text{Be}(n,\alpha){}^4\text{He}$ reactions for $|p_s| < 60$ MeV/ c are shown in Fig. 1. Tentatively, we simply assume isotropy, and s-wave penetrability correction for the p_0 and the p_1 channels, and p-wave correction for the α channel. The present and the previous data are plotted with marks as shown in the legend. The p_0 and the α channel cross sections are normalized to the previous data [5–14], and the p_1 absolute value is estimated from the ratio of the p_0 and p_1 yield. The prominence appearing in the p_0 excitation function around 300 keV well corresponds to the previously reported resonance by 3^+ state at $E_x = 19.24$ MeV of ${}^8\text{Be}$ [15]. The shape of the excitation function of the (n,α) is also roughly consistent with the previous studies [11–14] in a wide energy range up to 2 MeV. A multi-channel R -matrix analysis using AZURE2 code [16] is ongoing mainly to confirm the consistency of the present p_1 data, which are the first-ever data in the BBN energy region, with the previous data of these three reaction channels over a wide energy range from the comprehensive point of view of the resonance structure of the neutron-induced reactions on ${}^7\text{Be}$. We could reproduce basic features of these excitation functions simultaneously as shown in Fig. 1 as dashed lines with physically reasonable resonance parameters, from the thermal neutron energy to the order of mega electron volt; The calculation includes only neutron-emission states [17], no crucial conflict with the known spins, parities, excitation energies, total widths [17] nor the Wigner limits, and only the orbital angular momenta $l \leq 2$ were adopted. This R -matrix analysis revealed that the present p_1 cross section around the BBN

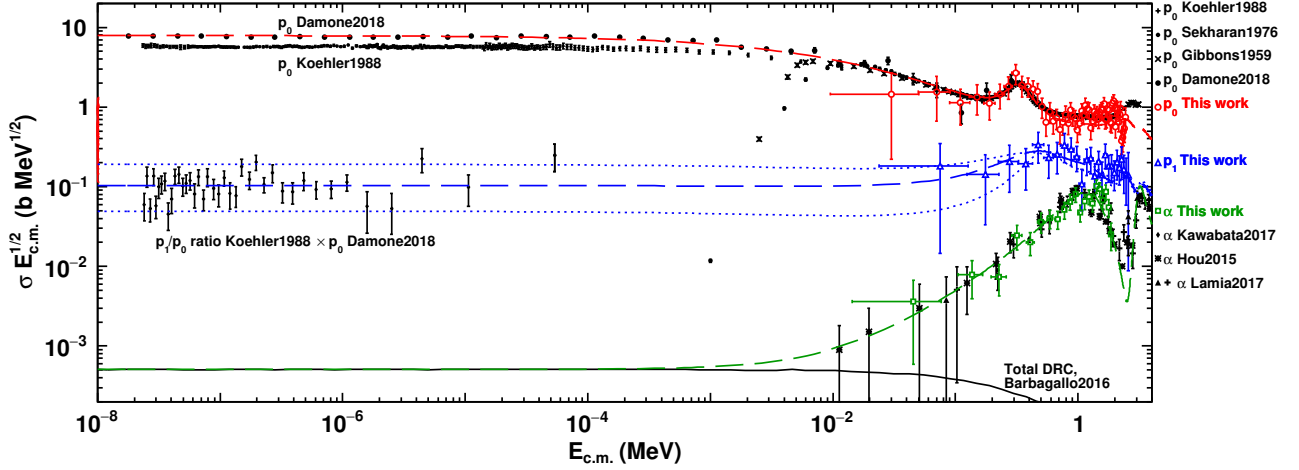


Figure 1. Preliminary cross sections of the ${}^7\text{Be}(n, p_0){}^7\text{Li}$, the ${}^7\text{Be}(n, p_1){}^7\text{Li}^*$ and the ${}^7\text{Be}(n, \alpha){}^4\text{He}$ reactions for $|p_s| < 60 \text{ MeV}/c$ are shown as open circle, triangle, square, respectively. The previous experimental data by Ref. [5–14] are plotted as in the legend. The solid line represents the estimation of the contribution from the direct radiative capture mechanism [12]. The dashed lines are the multi-channel R-matrix calculations. A possible p_1 range is indicated by dotted lines.

energies may be even consistent with that estimated from Ref. [5] and [10] near the thermal neutron energy. Although the contribution of the p_1 channel might not be comparable to that of p_0 , it is still one order of magnitude larger than that of the α , which had ever been completely unknown. The dotted line in Fig. 1 represents possible range of the p_1 cross section, calculated by changing the total width of the 1^- state located at 0.5 MeV. As the result, the deviation of the p_1 cross section is consistent with that of the the known p_1/p_0 ratio around the thermal neutron energy. Based on the newly obtained p_1 cross section by the R-matrix calculation, we calculated the ${}^7\text{Be}(n, p){}^7\text{Li}$ reaction rate relative to that of Ref. [3] as shown in Fig. 2. The solid line is the recent revision of the p_0 reaction rate by Ref. [10], and the dashed line is the sum of the present p_1 reaction rate to that one. The dotted lines express the possible range of the $p_0 + p_1$ reaction rate corresponding to that of the R-matrix calculation for the p_1 channel. The new total ${}^7\text{Be}(n, p){}^7\text{Li}$ reaction rate may be about 15% higher than that of Ref. [3]

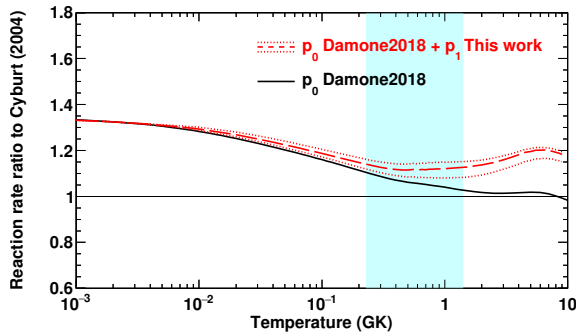


Figure 2. Preliminary reaction rate relative to that of Ref. [3]. The solid line is the recent revision of the p_0 reaction rate by Ref. [10], and the dashed line is the sum of the present p_1 reaction rate to that. The dotted line express the possible range of the $p_0 + p_1$ reaction rate corresponding to that of the R-matrix calculation for the p_1 channel. The shaded area corresponds to the BBN temperature range.

in the BBN temperature range, which may result in about a 10% reduction of the primordial ${}^7\text{Li}$ abundance according to the known sensitivity to this reaction [3].

This experiment was performed at RI Beam Factory operated by RIKEN Nishina Center and CNS, University of Tokyo, and supported by JSPS KAKENHI (Grant No. 15K17631).

References

- [1] C. Spitaleri *et al.*, Phys. Atom. Nucl. **74**, 1725 (2011).
- [2] Y. Yanagisawa *et al.*, Nucl. Instrum. and Meth. A **539**, 74 (2005).
- [3] R. H. Cyburt *et al.*, Rev. Mod. Phys. **88**, 015004 (2016).
- [4] S. Hayakawa *et al.*, CNS Annual Report, **CNS-REP-96**, 11 (2016).
- [5] P. Koehler *et al.*, Phys. Rev. C **37**, 917 (1988).
- [6] R. L. Macklin and J. H. Gibbons, Phys. Rev. **109**, 105 (1958).
- [7] R. R. Borchers and C. H. Poppe. Phys. Rev. **129**, 2679 (1963).
- [8] C. H. Poppe *et al.*, Phys. Rev. C **14**, 438 (1976).
- [9] K. Sekharan *et al.*, Nucl. Instrum. and Meth. **133**, 253 (1976).
- [10] L. A. Damone *et al.*, Phys. Rev. Lett. **121**, 042701 (2018).
- [11] S. Q. Hou *et al.*, Phys. Rev. C **91**, 055802 (2015).
- [12] M. Barbagallo *et al.*, Phys. Rev. Lett. **117**, 152701 (2016).
- [13] T. Kawabata *et al.*, Phys. Rev. Lett. **118**, 052701 (2017).
- [14] L. Lamia *et al.*, Astrophys. J. **850**, 175, (2017).
- [15] A. Adachchour and P. Descouvemont, J. Phys. G **29**, 395 (2003).
- [16] R. E. Azuma *et al.*, Phys. Rev. C **81**, 045805, (2010).
- [17] J.H. Kelley, *et al.*, Nucl. Phys. **A880**, 88, (2012).

Breakup mechanisms of the proton-dripline system $^{17}\text{F}+^{58}\text{Ni}$ at energies around the Coulomb barrier

L. Yang^{a,b}, C. J. Lin^b, N. R. Ma^b, H. Yamaguchi^a, D. X. Wang^b, L. J. Sun^b, K. Abe^a, M. La Commara^c, K. Y. Chae^d, S. M. Cha^d, S. Hayakawa^a, A. Kim^d, D. Kahl^a, M. S. Kwag^d, H. M. Jia^b, M. Mazzocco^{e,f}, C. Parascandolo^g, D. Pierroutsakou^g, C. Signorini^{e,f}, E. Strano^{e,f}, Y. Sakaguchi^a, F. Yang^b, Y. Y. Yang^h, G. X. Zhangⁱ, G. L. Zhangⁱ, M. Pan^a, and X. X. Xu^a

^aCenter for Nuclear Study, Graduate School of Science, University of Tokyo

^bDepartment of Nuclear Physics, China Institute of Atomic Energy

^cDepartment of Pharmacy, University Federico

^dDepartment of Physics, Sungkyunkwan University

^eDipartimento di Fisica, Universita di Padova

^fIstituto Nazionale di Fisica Nucleare-Sezione di Padova

^gIstituto Nazionale di Fisica Nucleare-Sezione di Napoli

^hInstitute of Modern Physics, Chinese Academy of Sciences

ⁱSchool of Physics and Nuclear Energy Engineering, Beihang University

The reactions of weakly bound stable and unstable nuclei have been extensively investigated for several decades [1,2]. The availability of radioactive beams has greatly broadened our ability to study the relation between nuclear structure and reaction mechanisms more in detail. The special features of nuclei such as ^{11}Li (two-neutron halo nucleus), ^{11}Be (one-neutron halo nucleus), and ^8B (one-proton halo nucleus), with more diffused density and high probability of breakup, have created much interest, since couplings to and within the continuum are particularly important for weakly bound nuclei and can have significant effects on other channels.

One of the most intriguing questions on the weakly bound reaction system concerns the effects of the breakup process and the extended radius of the nuclei, especially for halo nuclei, on the fusion cross section [3]. Different aspects have to be considered and they may lead to the opposite effects, either enhancing or suppressing the fusion cross section: the fusion in the Coulomb barrier energy region could be enhanced due to the large extent of the nuclear matter distribution (which reduces the Coulomb barrier) or hindered owing to the breakup channel arising from the small binding energy (leading to an attenuation of the incident current). To get an insight into this question, we need the detailed knowledge of the breakup mechanisms of weakly bound systems.

In the present work, we measured the breakup reactions of the proton-dripline system $^{17}\text{F}+^{58}\text{Ni}$ at four energies around the Coulomb barrier. ^{17}F has a low breakup threshold (0.6 MeV) into $^{16}\text{O}+p$, and its first excited state presents a proton-halo structure [4], which is bound by only 0.105 MeV. The experiment was performed at the low-energy radioactive isotope beam separator CRIB (Center for Nuclear Study Radioactive Ion Beam separator). The radioactive ^{17}F beam was produced via the $^2\text{H}(^{16}\text{O},^{17}\text{F})$ reaction in inverse kinematics by using a 6.6 MeV/nucleon ^{16}O primary beam accelerated by the RIKEN AVF cyclotron bombarding on a cryogenic deuterium gas target. By adjusting the

pressure of the gas target and inserting aluminium degraders of different thicknesses, we produced secondary ion beams of ^{17}F with four distinct energies. After separation by the double achromatic system, the secondary beam was further purified by velocity with a Wien filter. Finally, the purified ^{17}F beam with an intensity of $6\text{--}10\times 10^5$ particle per second and a purity of $\sim 85\%$ was transmitted to the reaction chamber and then impinged on the secondary target, which was a self-supporting, isotopically enriched sample of ^{58}Ni with a thickness of 1.0 mg/cm^2 and a diameter of 22 mm. The beam was tracked by two parallel plate avalanche counters (PPACs) in the reaction chamber, which enables us to reconstruct the trajectory of each incident beam ion event by event. Considering the energy loss in the two PPACs (the equivalent thickness of each PPAC is about $9.5\text{ }\mu\text{m}$ of Mylar) and target, the typical reaction energies (the energy in the middle of the target) of ^{17}F are 63.1, 55.7, 47.5 and 43.6 MeV, respectively. A newly developed detector array, MITA (a Multilayer Ionization-chamber Telescope Array) [5], was installed to measure the breakup fragments.

In order to distinguish the ^{16}O ions produced by direct reactions (i.e., breakup and/or transfer) versus those in the cocktail beam, the energy distribution of oxygen events, which are measured by the most forward telescope of MITA, are shown in Fig. 1. It can be seen that two groups of the oxygen ions were present. Monte Carlo simulations were carried out to identify the origin of these oxygen events, and the elastic scattering of $^{15,16}\text{O}$ beam contaminants from the target was taken into account as well. In the simulation code, we considered (i) the energy spread of the beam; (ii) the beam spot on the ^{58}Ni target; (iii) the geometry of the detector array, and (iv) the energy loss in the target. The simulated energy distribution, along with the experimental data are shown in Fig. 1. According to the simulations, the two groups mainly originate from the scattering of the beam contaminants $^{15,16}\text{O}$. Moreover, the region attributed to proton breakup and/or transfer reactions can be identified in the energy distribution spectrum, as demarked

by a black solid line in Fig. 1, which is consistent with the prediction of continuum discretized coupled-channels (CDCC) calculations [6].

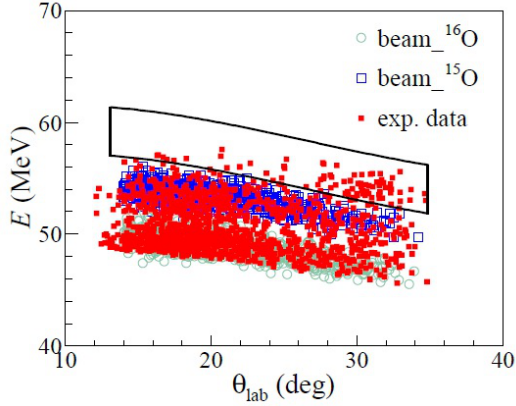


Figure 1. Energy distribution of oxygen measured by the telescope most forward telescope at $E_{\text{rec}} = 63.1$ MeV. See text for details.

Finally, the angular distributions of the ^{16}O events from the direct reactions of $^{17}\text{F}+^{58}\text{Ni}$ are shown in Fig. 2. The calculations with the frameworks of CDCC and the Ichimura, Austern, Vincent (IAV) model [7] are performed, which are responsible for the elastic breakup (EBU) and non-elastic breakup (NEB, including transfer, inelastic breakup and incomplete fusion) processes. The calculated results are also presented in Fig. 2, where we can find that the sum of EBU and NEB, i.e., the total breakup (TBU), can reproduce the experimental data reasonably. Moreover, the NEB is the major contribution for the direct reactions, indicating that the stripping process, rather than the diffraction, is dominant in the breakup dynamics of $^{17}\text{F}+^{58}\text{Ni}$ system.

The data analysis is still in process.

References

- [1] L. F. Canto, P. R. S. Gomes, R. Donangelo *et al.*, Phys. Rep. **424** (2006) 1.
- [2] L. F. Canto, P. R. S. Gomes, R. Donangelo *et al.*, Phys. Rep. **596** (2015) 1.
- [3] B. B. Back, H. Esbensen, C. L. Jiang and K. E. Rehm, Rev. Mod. Phys. **86** (2014) 317.
- [4] R. Morlock *et al.*, Phys. Rev. Lett. **79** (1997) 3837.
- [5] Submitted to Nucl. Instrum. Methods Phys. Res. A.
- [6] L. Jin, private communication.
- [7] M. Ichimura, Phys. Rev. C **37** (1988) 2264.

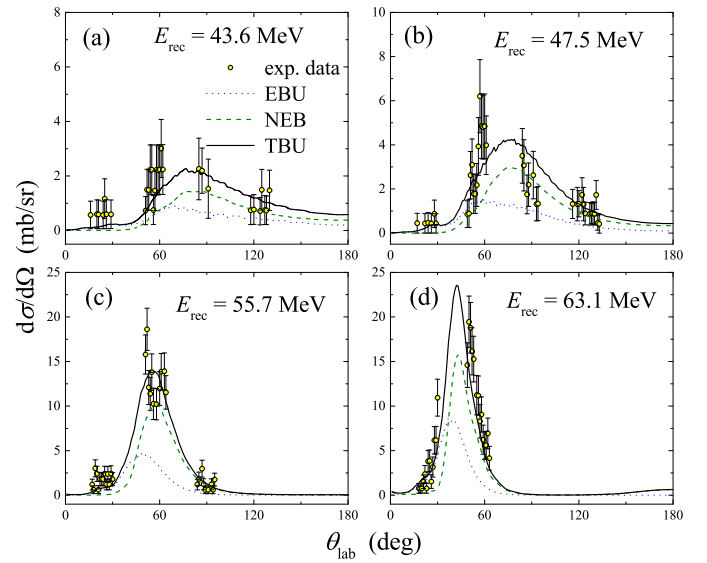


Figure 2. Angular distributions of ^{16}O from the direct reactions of $^{17}\text{F}+^{58}\text{Ni}$. The full circles denote the experimental data. The dotted and dashed curves are the calculated results with the frameworks of CDCC and IAV model, which are responsible for the EBU and NEB processes. The solid curves are the sum of CDCC and IAV model calculations, which demonstrate the TBU.

Measurement of low-energy E1 strength in ^{136}Xe with CAT-M via proton inelastic scattering

C. Iwamoto, S. Ota, S. Hayakawa, K. Kawata, Y. Mizoi^a, R. Kojima, H. Tokieda, N. Zhang^b, O. Beliuskina, M. Dozono, T. Harada^c, N. Imai, T. Isobe^d, N. Kitamura, S. Masuoka, S. Michimasa, T. Murakami^e, D. Suzuki^d, R. Tsunoda, J. Zenihiro^d, and E. Takada^f

Center for Nuclear Study, Graduate School of Science, University of Tokyo

^a*Osaka Electro-Communication University*

^b*Institute of Modern Physics*

^c*Department of Physics, Toho University*

^d*RIKEN Nishina Center*

^e*Department of Physics, Kyoto University*

^f*National Institutes for Quantum and Radiological Science and Technology*

Concentration of electric dipole (E1) strength at the lower excitation energy than the giant dipole resonance was observed in some medium-heavy nuclei, especially neutron rich nuclei. The low-lying E1 strength is discussed often in relation to a dipole oscillation of the excess neutron against the other core nucleus [1]. The low-lying E1 strength is also expected to constrain the slope parameter L of the nuclear equation of state at the saturation density of symmetric nuclear matter. However the nature and the origin of the low-lying E1 strength are still under discussion. The low-lying E1 strengths observed in unstable heavy nuclei and in stable nuclei may have different nature in the nuclear structure. By analyzing the transition densities obtained from a random-phase approximation calculation, the low-lying E1 strength in ^{90}Zr stable nucleus is not associated with the neutron skin oscillation although ^{132}Sn unstable nucleus have a transition density of typical neutron skin oscillation in the low-energy region [2]. Thus it is quite important to do systematic measurements of the low-lying E1 strength, especially the neutron number dependence including unstable nuclei. A correlation between the low-lying strength and the neutron number has been studied with several theoretical calculations [3, 4]. The spatially extending neutrons by occupying orbit of low angular momenta near Fermi energy plays an important role for the emergence of the low-lying E1 strength. Investigation of such a neutron number dependence including unstable nuclei can approach the nature of the low-lying E1 strength.

Inelastic proton scattering measurement have been used well as a promising tool to investigate the low-lying E1 strength in stable nuclei [5]. The E1 component can be decomposed from another multipole transition components by applying a multipole decomposition analysis (MDA) of the angular distribution. The E1 strength by Coulomb interaction with virtual photons can be determined to measure the E1 transition cross sections at forward angle than grazing angle.

In order to investigate the low-lying E1 strength in medium-heavy unstable nuclei, a experiment of inelastic proton scattering in inverse kinematics was performed. ^{136}Xe nucleus was chosen as the target for a trial experi-

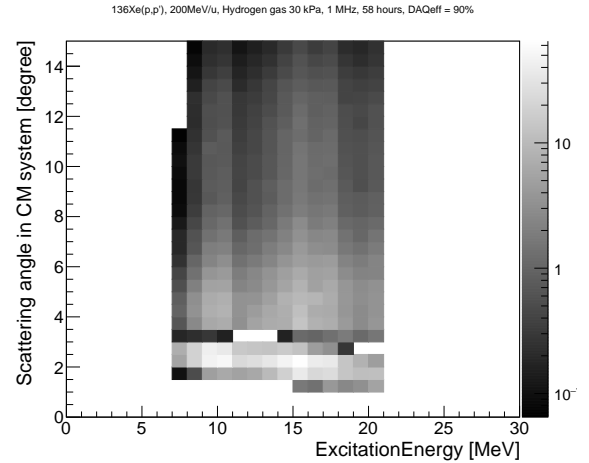


Figure 1. Yield estimation by simulating efficiency of CAT-M including a DAQ efficiency of 90%. In order to estimate the yield, cross sections of E1 strength in ^{132}Sn are referred from ref [7]. A beam intensity of 1 MHz and a measured time of 58 hours are assumed. Angular acceptance in the direction of azimuth angle is ± 30 degree. Vertical and horizontal axis is the scattering angle in center of mass system and excitation energy, respectively.

ment in order to validate the experimental method to study the low-lying E1 strength in inverse kinematics. Scattered protons of low kinetic energy have to be measured to obtain low excitation energy spectra and angular distributions at forward angle in inverse kinematics. In order to measure such low energy recoil protons, a gaseous active target system, CNS active target CAT-M [6], was employed. CAT-M consists of a time projection chamber (TPC) with the active area of $280 \text{ mm} \times 310 \text{ mm}$ and an array of silicon detectors on both sides of the TPC. Dual Gain Multilayer Thick Gas Electron Multipliers (DG-M-THGEM) [8] is employed as an electron multiplier of the TPC. Gain of DG-M-THGEM for recoil protons and beam particles could be was optimized independently in order to irradiate a high intensity

beams of heavy ion such as 1 MHz. Low pressure hydrogen gas of 30 kPa should be used to cover a angular range forward than 2.5 degree of the grazing angle in the center of mass system with the TPC. Angular distributions backward than 4 degree could be measured by combining the TPC and the array of the silicon detectors. In order to generate enough number of virtual photons, the projectile energy of 200 MeV/u is required. Assuming a beam intensity of 1 MHz, a measured time of 58 hours, a DAQ efficiency of 90% and simulated efficiency of CAT-M with angular acceptance of ± 30 degree in the direction of azimuth angle, estimated yield is shown in Figure 1. In this estimation, cross sections of E1 strength in ^{132}Sn [7] are used.

The experiment (program number 15H307) was performed at Heavy Ion Medical Accelerator in Chiba (HI-MAC) in the National Institute of Radiological Science. The primary beam of ^{136}Xe with an energy of 185MeV/u was introduced to the entrance of CAT-M chamber filled by hydrogen gas at the pressure of 30kPa. Beam intensity was monitored with a diamond detector installed 835.5 mm upstream of the entrance of CAT-M chamber during experiment. The maximum intensity of the beam was 750 k particle per pulse according to the diamond detector. Beam pipes in total of 793.5 mm filled by the hydrogen gas and one collimator were attached upstream of CAT-M to cut the multiple scattering. The beam pipes were connected to the entrance of CAT-M chamber. The collimator made of stainless steel was installed 219.5 mm upstream the entrance of CAT-M chamber and between the beam pipes. Aperture of the collimator is 30 mm in width and 80 mm in height. The opening areas of CAT-M as the entrance window for the beam to pass through were sealed with 0.05 mm-thick aluminized mylar film. The gain of DG-M-THGEM for the recoil protons was about 500 while the gain for the beam particles was operated about 30. Twelve silicon detectors were placed on both sides of the TPC. The position of the Silicon array was 275.4 mm from the beam axis in the closest case. The six silicon detectors were located on one side of the TPC field cage to cover the active region as much as possible and the other six silicon detectors were located on the other side. The effective volume of the silicon detector was $90.6 \text{ mm} \times 90.6 \text{ mm} \times 350 \mu\text{m}$ -thick and divided into 8 strip in the drift direction. A aluminized mylar foil with the thickness of $4 \mu\text{m}$ was placed in front of the silicon array to avoid noise from electric field of the field cage. The signals from the TPC and the silicon detectors were digitized using a digitizer module called Generic Electronics for Time Projection Chamber (GET) [9]. Dynamic range and trigger threshold can be optimized channel by channel. The dynamic ranges were 1 pC and trigger thresholds were optimized to cut signals of delta-ray. Detail construction of CAT-M is described at ref [6].

The measurement time was about 21.5 hours in total. DAQ efficiency was about 80% with the maximum beam intensity. According to the yield estimation, 20 counts of the giant dipole resonance event and 10 counts of the low-lying E1 events are expected at the scattering angle of 1.75 degree in center of mass system. The analysis is in progress.

References

- [1] N.Parr *et al.*, Rep. Prog. Phys. **70**, 691 (2007).
- [2] H. Nakada and T. Inakura, Physical Review C **87**, 034302 (2013).
- [3] T. Inakura *et al.*, Physical Review C **84**, 021302(R) (2011).
- [4] S. Ebata *et al.*, Physical Review C **90**, 024303 (2014).
- [5] For example, A. Tamii *et al.*, Phys.Rev.Lett. **107**, 062502 (2011).; C. Iwamoto *et al.*, Phys.Rev.Lett. **108**, 262501 (2012).
- [6] S. Ota *et al.*, CNS Annual Report 2017, CNS-REP-97 (2019) 41 - 42.
- [7] P. Adrich *et al.*, Physical Review Letters **95**, 132501 (2005).
- [8] C. Iwamoto *et al.*, CNS Annual Report 2016 CNS-REP-96 (2018) 51 - 52.
- [9] T. Isobe *et al.*, Nuclear Instrumental and Methods in Physics Research A **899** (2018) 43 - 48.

Deuteron Elastic Scattering on ^{16}O in inverse kinematics with CAT-S

H. Tokieda^a, S. Ota^a, M. Dozono^a, N. Imai^a, M. Itoh^b, Y. Kiyokawa^a, M. Kobayashi^a, C. S. Lee^{a,c}, S. Michimasa^a, Y. Nasu^b, E. Takada^d, T. Uesaka^c, K. Yako^a, and J. Zenihiro^c

^aCenter for Nuclear Study, Graduate School of Science, University of Tokyo

^bCyclotron and Radioisotope Center, Tohoku University

^cNishina Center RIKEN (The Institute of Physical and Chemical Research)

^dNational Institute of Radiological Sciences

Alpha clustering is an attractive phenomenon in nuclei for understanding nuclear structures, especially of light nuclei. Several predictions of alpha clusters have been reported on $N = 4n$ nuclei such as ^8Be , ^{12}C , ^{16}O , and ^{20}Ne [1–3]. As an example of $N = 4n - 1$ nuclei, the ^{11}B nucleus was reported to have $2\alpha + ^3\text{H}$ cluster structure in excited states [4]. Alpha cluster states are characterized by strong isoscalar monopole transitions, where the angular distribution of the differential cross section has a peak at forward angle. We developed a gaseous active target called CNS Active Targets (CAT) to measure low-energy recoiled particles corresponding to forward angle scattering, especially, up to 10 degrees in center-of-mass frame. The CAT consists of a time projection chamber (TPC) and silicon detectors on the both side of a field cage of TPC. The TPC was operated with 0.4-atm pure deuterium gas for the measurement of the isoscalar monopole transitions. As an electron multiplier of the CAT, 400- μm thick gas electron multipliers are employed [5]. We performed an experiment of deuteron scattering on ^{16}O at 100 MeV/u in inverse kinematics with the first generation of CAT, called CAT-S, in Heavy Ion Medical Accelerator in Chiba (HIMAC) (program number H307). Details of the experiment were reported in [6]. In this paper, we report the preliminary experimental results of deuteron elastic scattering on ^{16}O .

We reported on the event-search process of CAT analysis in Ref. [7]. After the event-search process, track reconstruction of recoiled deuterons was done by using the Bragg curve fitting. In order to identify recoiled particles, the trajectory was fitted by assuming the energy loss profiles of deuteron and proton. Differences between chi-squares of the Bragg curve fitting assuming deuteron (χ_d) and assuming proton (χ_p) are compared for a particle identification of recoil particles. Figure 1 shows the correlation between χ_p/χ_d and reduced χ_d . In Fig. 1, events of *deuteron-like* particles are plotted in the region where χ_d is smaller and χ_p/χ_d is larger (top-left region), while those of *proton-like* particles are shown up in bottom-right region. For the particle identification of recoiled particles, we used the following conditions: reduced $\chi_d < 5$, $\chi_p/\chi_d > 1.5$, and stopped point of recoiled particles and reaction point are in active area. The excitation energy (E_x) distribution deduced by missing mass method is shown in Fig. 2. These events correspond to $\sim 0.065\%$ of the CAT triggered events due to many beam-like particles. A peak at around $E_x = 0$ MeV in Fig. 2 is by deuteron elastic scattering. The E_x resolution

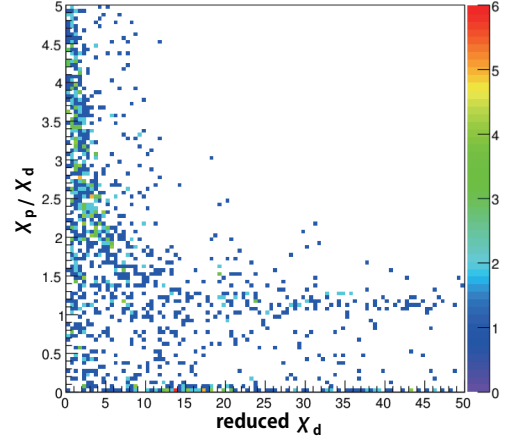


Figure 1. Correlation between χ_p/χ_d and reduced χ_d , assuming chi-squares of the Bragg curve fitting with deuteron and proton tables are χ_d and χ_p , respectively. This figure indicates that events of *deuteron-like* particles are plotted in top-left region and those of *proton-like* particles are plotted in bottom-right region.

was ~ 0.84 MeV(σ) for elastic scattering. Further analysis is in progress.

References

- [1] K. Ikeda, *et al.*, Prog. Theor. Phys. Suppl., **68** (1986): 1.
- [2] H. Horiuch, *et al.*, Prog. Theor. Phys. Suppl., **192** (2012): 1 .
- [3] M. Freer, Rep. Prog. Phys., **70** (2007): 2149.
- [4] T. Kawabata, *et al.*, Phys. Lett., **B646** (2007): 6-11.
- [5] S. Ota, *et al.*, Journal of Radioanalytical and Nuclear Chemistry, **305** (2015): 907-911.
- [6] H. Tokieda *et al.*, CNS Annual Report 2015 CNS-REP **95** (2017): 17.
- [7] H. Tokieda *et al.*, CNS Annual Report 2016 CNS-REP **96** (2018): 53.

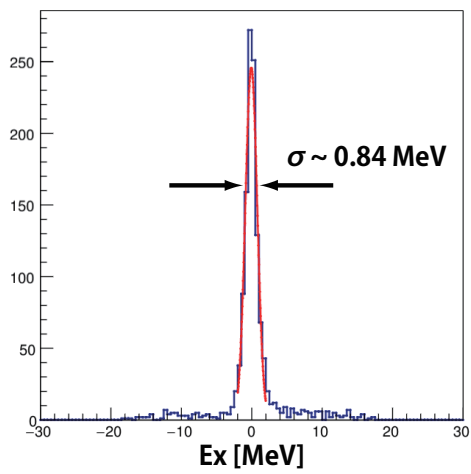


Figure 2. Excitation energy (E_x) distribution deduced by missing mass method when reduced $\chi_d < 5$ and $\chi_p/\chi_d > 1.5$. The E_x resolution was $\sim 0.84 \text{ MeV}(\sigma)$ for elastic scattering.

Production of isomer around ^{52}Fe nucleus via projectile fragmentation

Keita Kawata^{a,b}, Shinsuke Ota^a, Masanori Dozono^a, Juzo Zenihiro^b, Chihiro Iwamoto^a, Noritaka Kitamura^a, Hideyuki Sakai^b, Shoichiro Masuoka^{a,b}, Shin'ichiro Michimasa^a, Kentaro Yako^a, Tomoya Harada^{b,c}, Hiroki Nishibata^b, Rieko Tsunoda^a, Nobuyuki Imai^a, and Tomoya Sato^b

^aCenter for Nuclear Study, Graduate School of Science, University of Tokyo

^bRIKEN Nishina Center

^cToho University

The charge exchange reaction from iron is one of the most important topics in nucleosynthesis in the supernova explosion. That reaction is expected to occur in the high-temperature circumstance. The high temperature circumstance is corresponding to the excited state. One of the first subjects of such an experimental study is nuclear isomer. Due to the limited life of isomers it is provide as a beam. It is convenient to produce the isomer beam by fragmentation reactions since various isomer reactions can be studied with a common setup. Therefore producing isomer beam with high purity and controlling them is an important step.

The goal of our study are (1) to produce effectively isomer beams with high angular momentum and high excitation energy and (2) to clarify the dynamics of the fragmentation reaction involving large angular momentum transfer. Isometric state in ^{52}Fe at $E_x = 7$ MeV with $J^\pi = 12^+$ and a half-life of 46 sec is our first isomer of interest. Previously the isomer ratio of ^{52}Fe in the fragmentation of ^{58}Ni is reported as only 0.3% [1].

Production of high spin IR depends on several parameters. Kinematical conditions are summarized in Fig. 1. Here we consider a fragmentation of mass A_p nucleus into mass A_f isomer.

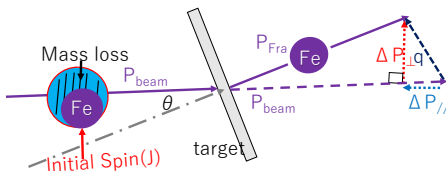


Figure 1. Total momentum transfer (q) can be divided into 2 directions which are longitudinal (ΔP_{\parallel}) and transverse (ΔP_{\perp}). The longitudinal axis is defined as the direction of the incoming projectile. The initial spin is defined as the spin of the projectile. The mass loss is defined as $A_p - A_f$.

Firstly the momentum transfer, $\vec{q} = \vec{P}_{\text{Fra}} - \vec{P}_{\text{beam}}$ induces angular momentum transfer through $\Delta L = r \times \Delta p$ [2, 3]. We note that the momentum transfer consists of two components as longitudinal and transverse as denoted in Fig. 1.

Secondly finite initial spin helps us to reach a large angular momentum of the isomer. In this sense $^{59}\text{Co}(J^\pi = 7/2^-)$ is expected to be nearer to $^{52}\text{Fe}(12^+)$ isomer than ^{58}Ni due to a better overlap of wave function with the $((\pi 1f_{7/2})^{-2}(\nu 1f_{7/2})^{-2})$ configuration in the $^{52}\text{Fe}(12^+)$ isomer. Finally the mass loss, defined as $A_p - A_f$, plays a role

because a larger number of knockout nuclei leads to a larger momentum transfer in general.

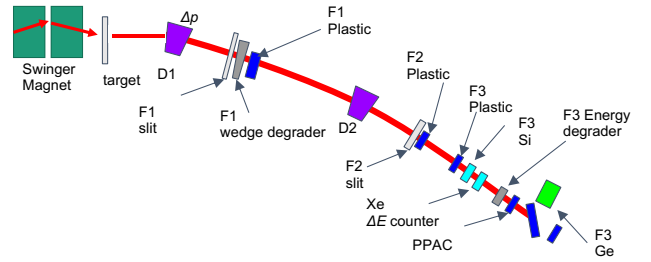


Figure 2. A schematic view of the experimental setup. The fragments are identified by using TOF-dE method, ToF is measured from F2 to F3 while dE is measured by a Si detector. The secondary beams stop at F3 plastic stopper. The total number of fragments is counted by the Si and the number of isomer was counted by Ge detector. $^{52}\text{Fe}(12^+)$ decays to an excited 11^+ state in ^{52}Mn by beta decay and then it decays to the ground state by emitting gamma rays.

We performed an IR measurement from the fragmentation reaction from 3 projectile. ^{58}Ni , ^{59}Co , and ^{82}Kr . Primary beam energy is 350 MeV/u and secondary beam energy is about 200 MeV/u. Figure 2 shows the beam line setting at HIMAC.

In measurement of ^{52}Fe isomer, we controlled ΔP_{\perp} through changing incident angles by the swinger magnet located just upstream of the target. The incident angles were set to 0.0, 0.5, 0.7 and 1 degrees. Primary target is ^9Be and the momentum of fragment was selected and separated at D1 and at D2, then lead to the stopper. With one $B\rho$ setting, we can measure the IR of ^{52}Fe and at the same time those around, such as of $^{53}\text{Fe}(19/2^-)$ and $^{54}\text{Co}(7^+)$.

Now we show IRs depending on some parameters. Figure 3 shows various IRs via ^{58}Ni , ^{59}Co and ^{82}Kr fragmentation reaction at 0 degrees depending on longitudinal momentum transfer in cm system. The upper panel shows the IRs of ^{53}Fe and ^{54}Co . The lower panel shows the IRs of $^{52}\text{Fe}(12^+)$ from ^{59}Co . Triangles show $^{54}\text{Co}(7^+)$ result and squares show $^{53}\text{Fe}(19/2^-)$. The IRs from $^{59}\text{Co}(7/2^-)$ is different from those from ^{58}Ni . Comparing IRs from some projectile nuclei, it was found that the IRs largely depend on mass loss. Also it is confirmed that the IRs depend on longitudinal momentum transfer ΔP_{\parallel} .

On the other hand the effects of the transverse momen-

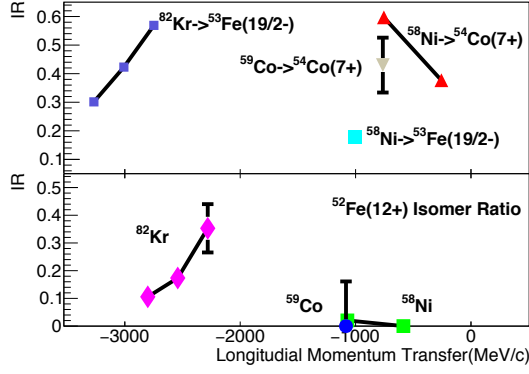


Figure 3. IRs as functions of $\Delta P_{||}$ (MeV/c). See text for details.

tum transfer ΔP_{\perp} is different. Figure 4 shows the IR depending on ΔP_{\perp} in the fragmentation of ^{58}Ni . The upper panel shows the IR of ^{53}Fe and ^{54}Co . Here some points are at the same $\Delta P_{||}$. The lower panel shows the IR of $^{52}\text{Fe}(12^+)$ state. Triangles show the $^{54}\text{Co}(7^+)$ result and squares show $^{53}\text{Fe}(19/2^-)$ under the same momentum condition. Comparing with $\Delta P_{||}$ -dependency of IR, ΔP_{\perp} -dependency is weaker. It is curious to see the IR of $^{54}\text{Co}(7^+)$ decreases with ΔP_{\perp} .

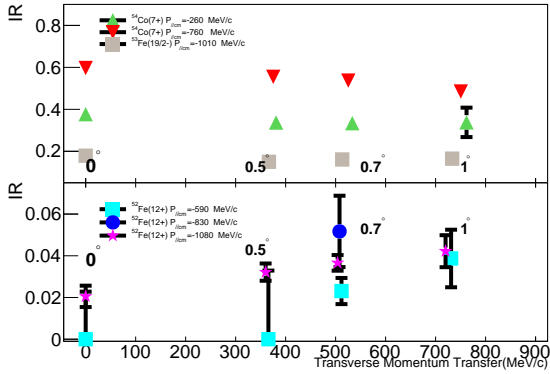


Figure 4. IRs as functions of ΔP_{\perp} (MeV/c). See text for details.

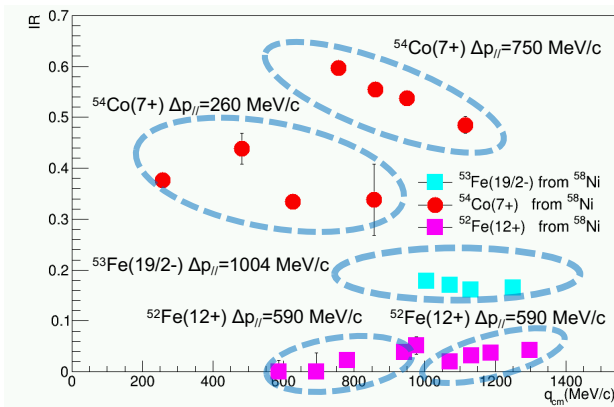


Figure 5. IRs as functions of q in projectile fragmentation of ^{58}Ni . The data points are grouped by $\Delta P_{||}$.

Figure 5 shows the result of IR with ^{58}Ni beam depending on total momentum transfer (q). Red points are the

IR of $^{54}\text{Co}(7^+)$ while the blue and purple squares are of $^{53}\text{Fe}(19/2^-)$ and $^{52}\text{Fe}(12^+)$, respectively. The IR seems almost independent of q as long as $\Delta P_{||}$ is the same. Therefore we can conclude that $\Delta P_{||}$ and ΔP_{\perp} act differently on IR.

Here we compare experimental IRs with model calculation in Table 1. This model calculation is known as statistical abrasion-ablation model like Goldhaber distribution where the momentum distribution is obtained [4]. Although this model currently is incapable of separating the effects of $\Delta P_{||}$ and ΔP_{\perp} , it gives a dependence of mass loss and J state as well as q . IRs in large mass loss is in good agree-

Table 1. Comparison of IR_{exp} with IR_{model} in small mass loss and large mass loss.

projectile	fragment	J^{π}	IR_{exp}	IR_{model}	Mass loss
^{58}Ni	^{52}Fe	12^+	0.0329	$1.86e^{-4}$	6
^{58}Ni	^{53}Fe	$19/2^-$	0.163	$1.49e^{-3}$	5
^{58}Ni	^{54}Co	7^+	0.518	0.110	4
^{59}Co	^{54}Co	7^+	0.430	0.0271	5
^{82}Kr	^{52}Fe	12^+	0.176	0.185	30
^{82}Kr	^{53}Fe	$19/2^-$	0.442	0.331	9

ment with the static abrasion-ablation model calculation, but there are large gap between IR of the experiment and the model in small mass loss. In the next step we will develop a new model calculation where $\Delta P_{||}$ and ΔP_{\perp} are treated separately and compare the data of small mass loss. A candidate theory framework is Glauber theory.

In summary, we successfully produced the $^{52}\text{Fe}(12^+)$ isomer with an isomer ratio of 18% and it is useful in some nuclear reactions. We tried to discuss the longitudinal and transverse momentum transfer ($\Delta P_{||}$ and ΔP_{\perp}) separately and found out that the IRs depend much on the longitudinal momentum transfer $\Delta P_{||}$ while the IRs depend less on the transverse momentum transfer ΔP_{\perp} .

It is difficult to conclude the effect of finite initial spin at this moment. On the other hand, IR was found to depend greatly on mass loss in this experiment. We can compare mass loss effect with the current model calculation but we need a new calculation to discuss the difference of the longitudinal / transverse momentum transfers.

References

- [1] K. Minamisono *et al.*, Phys. Rev. Lett. **171**, 252501 (1986).
- [2] W.-D. Schmidt-Ott *et al.*, Z. Phys. A **359**, 215-219 (1994).
- [3] X. L. Tuet *et al.*, Phys. Rev. C **95**, 014610 (2017).
- [4] M.De Jong *et al*, Nucl. Phys. A 613, 435-444 (1997).

Search for double Gamow-Teller giant resonance in ^{48}Ti

M. Takaki, T. Uesaka^a, N. Aoi^b, M. Dozono, T. Furuno^c, C. Iwamoto^b, T. Kawabata^c,
M. Kobayashi, Y. Matsuda^d, M. Matsushita, S. Michimasa, S. Ota, M. Sasano^a, L. Stuhl, A. Tamii^b,
M. Tsumura^c, R. Yokoyama, J. Zenihiro^a and S. Shimoura

Center for Nuclear Study, Graduate School of Science, University of Tokyo

^a*RIKEN (The Institute of Physical and Chemical Research)*

^b*Research Center for Nuclear Physics, Osaka University*

^c*Department of Physics, Kyoto University*

^d*Cyclotron and Radio Isotope Center, Tohoku University*

Double giant resonances (DGRs), a giant resonance built on another giant resonance, were investigated by using Coulomb excitations and pion double charge exchange reactions [1]. Among them, DGRs with spin-flip excitations were not observed so far. A double Gamow-Teller (GT) giant resonance (DGTGR) is composed of two single GT giant resonances, and is the second order spin-isospin excitation. The DGTGR is a unique research object to study if the DGT transitions are just superposition of single GT excitations, or the spin-dependent correlations cause further changes to structures and responses of DGT states. The information on DGTGRs will provide a comprehensive understanding of the collective behavior in terms of phonon degrees of freedom.

Another obvious interest of DGTGR lies in its relevance to the neutrino physics; the DGT transition is induced by the same transition operator as the $\beta\beta$ -decays (DBD), i.e. $\sigma\tau\sigma\tau$. If 0-neutrino DBD mode is observed, it would give a direct evidence that the neutrinos are Majorana particles. Here, the DGTGR can be an alternative reference for nuclear structure calculations of DBD which is needed to deduce a quantity of interest from the observed lifetime. The $\beta\beta$ -decay occupies a small portion of the total DGT transition strength (sum rule [2]) of 0.01-0.1%, whereas the DGTGR covers a large portion of the strength. Thus, the observation of such large DGT strength serves as an alternative calibrator of the nuclear structure calculation for $\beta\beta$ -decay processes.

The DGTGR was predicted by Auerbach *et al.*, in 1989 [3]. None of experiments, however, have succeeded in observation of the DGTGR. For the DGT transition study, the double spin-isospin flip should occur, and thus, heavy-ion double charge exchange reactions (HIDCXs) are promising. In addition, a (p, n) -type HIDCX probe is much more effective to investigate the DGTGRs in heavy nuclei appearing the large collectivity, while a (n, p) -type probe can excite the DGT states only weakly [4]. We, thus, invented a new probe, $(^{12}\text{C}, ^{12}\text{Be}(0_2^+))$ reaction, on the basis of the results of our first HIDCX experiment [5]. The probe has significant advantages for the DGT study,

- (1) the transition from the grand state of ^{12}C to the second 0^+ state of ^{12}Be has strong DGT strength,
- (2) and the final state $^{12}\text{Be}(0_2^+)$ can be distinguished by

detecting the characteristic γ -rays with an energy of 511 keV emitted in its decay process [6].

These two advantages are difficult to satisfy by other stable isotope induced DCX reactions.

Our study aims at the observation of the DGTGR in ^{48}Ti through the $^{48}\text{Ca}(^{12}\text{C}, ^{12}\text{Be}(0_2^+))$ reaction experiment. We have conducted the experiment by employing the high-resolution magnetic spectrometer Grand Raiden at Research Center for Nuclear Physics, Osaka University. Detailed descriptions of the experimental setup can be found in Ref. [7]. In this report, we present the progress of analysis for the deduction of the excitation energy spectrum of ^{48}Ti via the heavy-ion double charge exchange reaction.

Figure 1 shows an excitation energy spectrum which is obtained by selecting the events with the detection of the characteristic decay γ -rays. In the selected events, however, the events that the ^{12}Be particles accidentally coincide background γ -rays possibly remain as reported in Ref. [8]. To obtain a cross section of the $^{48}\text{Ca}(^{12}\text{C}, ^{12}\text{Be}(0_2^+))^{48}\text{Ti}$ reaction, the accidental coincidence distribution is evaluated by using the accidental coincidence rate in each excitation energy bin and the singles ^{12}Be spectrum. The shaded histogram represents the accidental coincidence contribution. The contribution is evaluated to be 26% to the total statistics.

We obtained the double differential cross section spectra as shown in Fig 2. The scattering angle ranges are $\theta = 0.0^\circ - 0.8^\circ$, $0.8^\circ - 1.6^\circ$ and $1.6^\circ - 2.4^\circ$ with the excitation energy binning of 1.0 MeV. The angular steps are limited by the scattering angle resolution of 0.8° and statistics. The excitation energy resolution was 1.3 MeV in FWHM. It should be noted that the $E_x = 0$ MeV is corresponding to the Q-value of the $^{48}\text{Ca}(^{12}\text{C}, ^{12}\text{Be}(0_2^+))^{48}\text{Ti}(\text{g.s.})$ reaction. The accidental coincidence events were subtracted.

All the spectra show the large non-resonant continuum component which increase from around the particle decay threshold ($E_x \sim 11.0$ MeV). Further more the forward scattering angle data has larger continuum contribution. This tendency is consistent with the case of the previous $^{24}\text{Mg}(^{18}\text{O}, ^{18}\text{Ne})^{24}\text{Ne}$ reaction experiment [4].

For the most forward angle spectrum (top panel of Fig. 2), we can find structures at the excitation energies of $E_x = 16$ and 26 MeV. The former component is almost

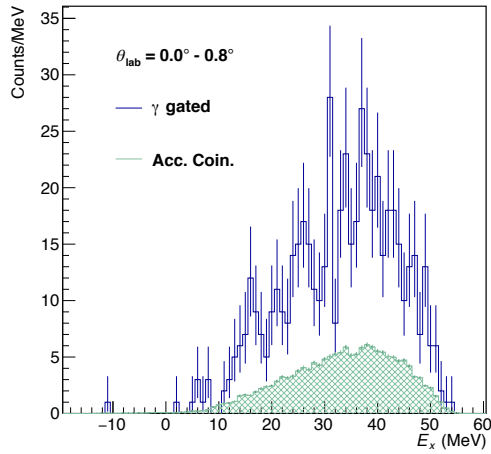


Figure 1. Excitation energy spectrum of $^{48}\text{Ca}(^{12}\text{C}, ^{12}\text{Be}(0_2^+))^{48}\text{Ti}(\text{g.s.})$. The shaded histogram shows the accidental coincidence contribution. The spectra were obtained the scattering angle range of $\theta = 0.0^\circ - 0.8^\circ$. The error bars represent statistical errors.

same energy as the double isobaric analog state (DIAS) with the excitation energy of $E_{\text{DIAS}} = 17.4$ MeV. However, the sum rule value calculation predicted that the DIAS can be excited only weakly about 3% of the DGT sum rule value via the DGT transition [2]. In the $(^{12}\text{C}, ^{12}\text{Be})$ reaction, the DIAS transition considered to be weak because the 0^+ states in ^{12}B were not observed in single charge exchange reaction experiments. Therefore, the structure might be the double GT excitation. The higher excitation energy component is most likely a DGT resonance. If we assumed no correlation between two giant resonances, the DGT resonance is predicted to exist at the excitation energy of $E_{\text{DGT}} = 2(E_{\text{GTR}} - E_{\text{IAS}}) + E_{\text{DIAS}} \sim 26$ MeV. The single GT giant resonance in ^{48}Sc exists at around $E_{\text{GTR}} = 11$ MeV [9] and the IAS was found at $E_{\text{IAS}} = 6.7$ MeV. This simple assumption is reasonably agreement with the measured excitation energy. It may indicate that the correlation between two GT resonances is small. In the early studies [10], the impact of correlations between two giant resonances on DGR excitation energies was also reported to be small. For the further discussion on the correlation, the width and the cross section of the resonance will be examined.

In order to clarify the natures of the candidates of the DGT resonances, the angular distribution of the cross section will be analyzed. In addition, the DGT transition strength to ^{48}Ti will be extracted. Further analysis is in progress.

References

- [1] Ph. Chomaz and N. Frascaria, *Physics Reports* **252**, 275 (1995).
- [2] H. Sagawa and T. Uesaka, *Phys. Rev. C* **94**, 064325 (2016).
- [3] N. Auerbach, L. Zamick and D.C. Zheng, *Annals of*

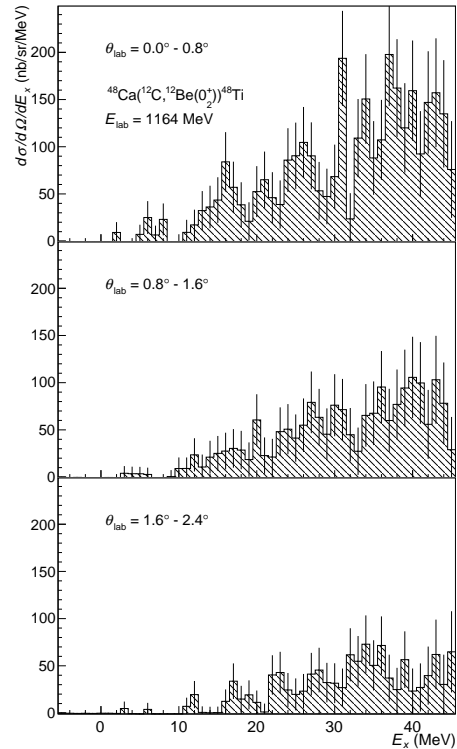


Figure 2. Double differential cross sections with scattering angle ranges $0.0^\circ - 0.8^\circ$ (upper), $0.8^\circ - 1.6^\circ$ (middle) and $1.6^\circ - 2.4^\circ$ (bottom), respectively.

Physics **192**, 77 (1989).

- [4] J. Blomgren *et al.*, *Phys. Lett. B* **362**, 34 (1995).
- [5] M. Takaki *et al.*, *JPS Conf. Proc.* **6**, 020038 (2015).
- [6] S. Shimoura *et al.*, *Phys. Lett. B* **560**, 31 (2003); *ibid* **654**, 87 (2007).
- [7] M. Takaki *et al.*, *CNS Rep.* **94**, 9 (2016).
- [8] M. Takaki *et al.*, *CNS Rep.* **96**, 3 (2018).
- [9] K. Yako *et al.*, *Phys. Rev. Lett.* **103**, 012503 (2009).
- [10] T. Aumann, P. F. Bortignon, and H. Emling, *Ann. Rev. Nucl. Part. Sci.* **48**, 351 (1998), and references therein.

Re-measurement of the ${}^4\text{He}({}^8\text{He}, {}^8\text{Be})$ reaction

S. Masuoka, S. Shimoura, M. Takaki, S. Ota, S. Michimasa, M. Dozono, C. Iwamoto, K. Kawata, N. Imai, N. Kitamura, M. Kobayashi, R. Nakajima, H. Tokieda, R. Yokoyama, D. S. Ahn^a, H. Baba^a, N. Fukuda^a, T. Harada^b, E. Ideguchi^c, N. Inabe^a, Y. Kondo^d, T. Kubo^a, Y. Maeda^e, F. M. Marqués^f, M. Matsushita, T. Nakamura^d, N. Orr^f, H. Sakai^a, H. Sato^a, P. Schrock, L. Stuhl^b, T. Sumikama^a, H. Suzuki^a, H. Takeda^a, K. Taniue^e, T. Uesaka^a, K. Wimmer^g, K. Yako, Y. Yamaguchi, Y. Yanagisawa^a, K. Yoshida^a, and J. Zenihiro^a

Center for Nuclear Study, the University of Tokyo

^a*RIKEN Nishina Center*

^b*Department of Physics, Toho University*

^c*Research Center for Nuclear Physics, Osaka University*

^d*Department of Physics, Tokyo Institute of Technology*

^e*Faculty of Engineering, Univ. of Miyazaki*

^f*Laboratoire de Physique Corpusculaire, IN2P3-CNRS, ENSICAEN et Université de Caen*

^g*Department of Physics, the University of Tokyo*

Nuclei composed of only neutrons have been discussed for over a half century. However, their existence has not been confirmed. In 2002, a candidate bound state of the tetra-neutron, which consists of four neutrons, was reported [1]. An *ab-initio* calculation suggested that there might be a tetra-neutron ($4n$) resonance, but a bound $4n$ was not reproduced [2]. An experimental search for the $4n$ resonance state conducted using the exothermic double charge exchange (DCX) ${}^4\text{He}({}^8\text{He}, {}^8\text{Be})4n$ reaction was performed at the SHARAQ spectrometer in RIBF [3]. As a result, four events of a candidate resonant state were found with a 4.9σ significance level, and the excitation energy of $4n$ was determined as $E_{4n} = 0.83 \pm 0.65(\text{stat.}) \pm 1.25(\text{syst.})$ MeV which is close to the threshold.

To decide that the tetra-neutron state is a bound ($E_{4n} < 0$) or resonant or correlating continuum ($E_{4n} > 0$) state, it is required to reduce the systematic uncertainty for the excitation energy of $4n$. In addition, statistically significant data is required for confirming spectra around the $4n$ threshold. We have performed a new measurement to satisfy these requirements.

Considering the ratio of the magnetic rigidities of the ${}^8\text{Be}$ ejectile and the ${}^8\text{He}$ projectile is nearly 1/2, the (${}^3\text{H}, {}^3\text{He}$) reaction having the same rigidity ratio with the same beam rigidity is to be measured without changing the settings of beamline magnets and the SHARAQ spectrometer. Actually, we use the ${}^3\text{H}$ beam energy of 310 A MeV, which has the same rigidity (8.3 Tm) as the 186A-MeV ${}^8\text{He}$. Since the kinematics of the ${}^1\text{H}({}^3\text{H}, {}^3\text{He}){}^1\text{n}$ reaction is determined uniquely, the systematic errors of the missing mass calibration is expected to be minimized.

In order to obtain more statistics than the previous experiment, the intensity of the ${}^8\text{He}$ secondary beam of 186 MeV/nucleon was approximately twice that in the previous experiment (3.5×10^6 cps at the target). At the “F3 (achromatic focus for beam trigger),” “F6 (dispersive focus),” and “S0 (achromatic focus for the secondary target),” a redundant number of low-pressure multi-wired drift

chambers (LP-MWDCs) were used for tracking the beam. Events for the physics run were triggered by the S2 plastic scintillator at the focal plane of the SHARAQ spectrometer. Because of the high-rate beam condition, a single event may contain multiple hits at the drift chambers over several beam bunches of 13.7 MHz (RF frequency), considering the maximum drift time for the MWDCs is comparable to the interval of the beam bunch. Hence it is necessary to treat information of the redundant planes and other detectors.

In order to estimate the number of true four-neutron events, a strict cut satisfying the condition that the two clusters at the cathode planes of S2 have consistent energy signals with 2 α particles originating in the ${}^8\text{Be}$ is analyzed. A preliminary analysis shows a similar event pattern in a spectrum as a function of the momenta of ${}^8\text{He}$ and ${}^8\text{Be}$ that is similar to the previous experiment. To consider the analyzed area of the decay cone of ${}^8\text{Be}$, we expect approximately 2-3 times more statistics than the previous experiment.

A more precise calibration for the missing-mass spectrum taking into account the energy loss and straggling at the detectors and the target to reduce systematic errors will be performed concurrently.

In summary, we are still attempting to purify true events for increasing statistics with careful rejection conditions for the background. In parallel, missing-mass calibration will be tuned up to increase the accuracy of the $4n$ energy. Further analysis is in progress.

References

- [1] F.M. Marqués et. al., Phys. Rev. C **65**, 044006 (2002).
- [2] S.C. Pieper, Phys. Rev. Lett. **90**, 252501 (2003).
- [3] K. Kisamori et al., Phys. Rev. Lett. **116**, 052501 (2016).

Present status of EDM experiment with laser cooled radioactive atoms

Y.Sakemi, H.Nagahama, T.Hayamizu, N.Ozawa, K.S.Tanaka^a, K.Harada^a, A.Uchiyama^a, J.Tsutsumi^b

Center for Nuclear Study, Graduate School of Science, The University of Tokyo

^a *Cyclotron and Radioisotope Center, Tohoku University*

^b *Department of Physics, College of Science, Rikkyo University*

The fundamental symmetries, charge conjugation (C), parity (P) and time reversal (T), play a significant role in the Standard Model (SM) of elementary particle physics. Of these, T symmetry and the combined CP symmetry are the least well understood, and they hold valuable clues for unraveling the secrets of nature. All subatomic particles are postulated to possess an intrinsic property known as a permanent electric dipole moment (EDM). The EDM of an atom is a combination of those of each constituent particle and also CP-violating interactions between the particles [1]. Being many-particle systems, atoms and molecules are ideal candidates for probing a rich variety of both T- and CP-violating interactions. Paramagnetic atoms, which have a single valence electron in their outer shell, are sensitive to subtle signals associated with CP violations in the leptonic sector, i.e., the EDM of the electron.

Since an electron is a point particle with a non-zero spin, it may possess an intrinsic EDM. However, the electron EDM (e-EDM) is predicted to be very small by many particle physics models. The magnetic dipole moment of the electron has been measured to a precision of just a few parts in a hundred trillion, which is the most accurate verification of a quantum electrodynamics prediction in the history of physics. However, its counterpart, the e-EDM, is still speculative. If the e-EDM was identified, it could be used to indirectly investigate particles with masses of tera electron Volts or higher, which are beyond the reach of even planned high-energy particle colliders [2]. Experimental searches for the e-EDM are currently being carried out using neutral atoms such as thallium (Tl) and francium (Fr), molecules such as YbF and ThO, and solid-state materials. Although no conclusive result has yet been obtained, some upper limits have been established.

The magnitude of the coupling constant is so small that the current experimental sensitivity about 10^{-29} ecm needs to be improved by almost ten orders of magnitude to test the prediction of the SM (10^{-38} ecm), which appears impossible in the foreseeable future. However, there are many extended versions of the SM that predict the e-EDM to be within the reach of current or proposed EDM experiments. This allows the predictions of various models of particle physics to be tested, including the most attractive SUSY models. Under the simple SUSY model, the EDM for an unknown particle can be expressed as

$$d_e \sim \frac{\alpha}{4\pi} \frac{m_\tau}{M_i^2} \frac{\mu m_{\tilde{B}}}{M_i^2} \sin \theta_\mu \tan \beta \quad , \quad (1)$$

where θ_μ is the CP phase, M_i is the SUSY particle mass, α is a fine structure constant. Francium is the heaviest alkali element and is therefore its atomic EDM is therefore most sensitive to the e-EDM. It thus provides a rich laboratory for investigating CP violation arising from the leptonic sector.

The high nuclear charge of Fr significantly enhances the atomic EDM to approximately 895 times that of a free electron, which is calculated very accurately with a relativistic couple cluster model [3,4], therefore Fr is one of the most promising candidates for investigating the e-EDM. At the RI Beam Factory (RIBF) in RIKEN, many kinds of isotopes of Fr can be produced, and we can study the EDM for many Fr isotopes. The ^{210}Fr has high sensitivity to electron EDM. As the number of neutrons increases, the octupole deformation of nuclei becomes large, and as a result, nuclear EDM is amplified for ^{221}Fr etc. It is very important that the CP violating interactions between nucleon and electron can be contributed to the EDM of an atomic system, and it can be extracted from atomic EDM.

The francium is produced by a nuclear fusion reaction between ^{197}Au in the target and an ^{18}O beam produced by an AVF cyclotron accelerator. The beam energy is adjusted to just above the coulomb barrier of ~ 100 MeV, which yields the maximum cross section for the $^{18}\text{O}+^{197}\text{Au}$ reaction to produce ^{210}Fr . The Fr atoms diffuse inside the Au target, and some reach the surface, where a certain fraction are desorbed. In this process, an electron is stripped away to produce a Fr^+ ion with a surface ionization process. One of the key issues to achieve the high intensity cold Fr source is the neutralizer, which recombines the electron to the Fr ion to produce the neutral Fr atom with high neutralization efficiency. The Fr ion is injected to the target, yttrium (Y) that has the work function smaller than the ionization potential of Fr. The injected Fr ion becomes a neutral atom and it will be desorbed from the target surface when the Y target is heated. The Magneto-Optical Trap (MOT) glass cell is attached to the neutralizer directly. The trapping efficiency is less than 1% at present, due to the loss of the atoms by sticking to the inner wall of the tube connected from the neutralizer to the MOT cell, and the velocity of the atoms are too fast compared to the capture range of the MOT. The trapping efficiency can be improved by longitudinal laser cooling for the deceleration of the velocity.

We developed a MOT system shown in Fig. 1, which was directly attached to the chambers for the neutralizer. We have succeeded in developing a frequency-offset locking technique that can adjust the resonance frequency while keeping the two kinds of light sources (trapping and repumping) needed for Fr trapping [5] at a constant frequency difference of 46 GHz. Furthermore, a frequency stabilization technique using iodine (I_2) molecules has been established as a secondary frequency reference for which excitation levels exist near the Fr resonance frequency. The Fr MOT has been succeeded in the experiment at CYRIC, Tohoku University as shown in Fig.1 and 2 [6]. The primary beam intensity at RIKEN will be increased with 10 times, and the number of Fr in the MOT with 10^7 , which is required for the EDM accuracy 10^{-30} ecm, can be achieved at RIKEN.

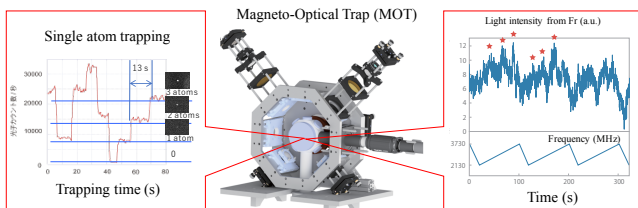


Fig.1. The MOT overview. The result of coherence time with single atom trap (left) and the Fr trap result with the time dependence (Fr in/out) (right).

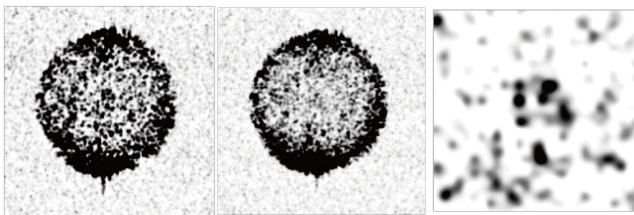


Fig.2. Fluorescence image of the MOT containing Fr atoms (left) and background image without Fr atoms (center). The trapped Fr can be observed from the difference of these images (right), although the number of the Fr atom is limited and less than 10^2 .

Since a MOT gives trapping force by a combination of gradient magnetic field and laser light, this magnetic field is not suitable for the EDM measurement. We have developed an optical dipole force trap (ODT), which can be interpreted as one dimensional optical lattice (OL) that traps the atoms with the potential formed by the standing wave of laser light with the lattice shaped potential. Since the OL has a lattice spacing of about the wavelength of laser light of ~ 100 nm, atomic collisions are suppressed and interaction time can be prolonged. We introduced high-intensity fiber laser and confirmed the formation of ODT/OL with stable atom Rb as shown in Fig.3. Moreover, lifetime measurements by single

atom trap show that 10 seconds or more can be achieved in OL with no disturbance of adjacent atoms as shown in Fig.1.

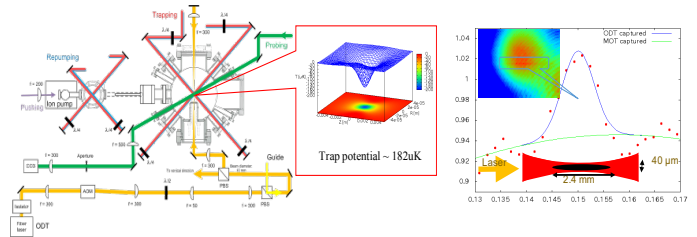


Fig.3. ODT and OL setup. The right plot shows the ODT trapping for Rb atoms.

The cold Fr facility utilizes the high intensity heavy ion beam supplied by AVF cyclotron to produce high flux of Fr isotopes of interest and applies laser cooling techniques on these radioactive isotopes (RI). This cold Fr source has a function capable of investigating various fundamental symmetries. The development of laser apparatus and the construction of the experimental room for the laser are in progress.

References:

- [1] Maxim Pospelov, Adam Ritz, *Annals Phys.* 318 (2005) 119-169.
- [2] Altmannshofer, Harnik, Zupan, *JHEP*11 (2013) 202. and Martin Jung, *JHEP* 1305 (2013) 168.
- [3] D.Mukherjee, B.K.Sahoo, H.S.Nataraj, B.P.Das, *J.Phys.Chem.A*113(2009)12549.
B.K. Sahoo, T. Aoki, B.P. Das, Y. Sakemi, *Phys.Rev.* A93 (2016) 032520.
- [4] Y. Sakemi et al., *J.Phys.Conf.Ser.* 302 (2011) 012051.
B.K. Sahoo, D.K. Nandy, B.P. Das, Y. Sakemi, *Phys.Rev.* A91 (2015) 042507.
- [5] K.Harada, Y.Sakemi, et al. *Appl.Opt.* 55(2016)1164-1169.
T.Aoki, Y.Sakemi, et al., *Phys.Rev.*A87(2013)0642426.
U.Dammalapati, K.Harada, Y.Sakemi, *Phys.Rev.*A93(2016)043407.
- [6] Y.Sakemi, *KOGAKU:光学 (Optical Society of Japan)* Vol.47 (2018) 301.

**Experimental Nuclear Physics: PHENIX
Experiment at BNL-RHIC and ALICE
Experiment at CERN-LHC**

Progress of low mass dielectron analyses in pp and Pb-Pb collisions with ALICE at the LHC

T. Gunji for the ALICE Collaboration

Center for Nuclear Study, Graduate School of Science, The University of Tokyo, Japan

One of the motivations to measure photons and dileptons in ultra-relativistic heavy-ion collisions is to understand the thermodynamical properties of the Quark-Gluon Plasma (QGP) created in heavy-ion collisions [1]. Different invariant mass regions of the dielectron pairs are sensitive to different aspects of heavy-ion collisions. The low mass region ($m_{\pi^0} \leq m_{ee} \leq m_{\eta}$) is a window for the measurements of the virtual photons, while the mass region around $m_{ee} \leq m_{\rho}$ has a link to the vacuum or in-medium modification of the spectral functions of short-lived mesons (ρ , ω , ϕ) [2]. Dielectrons with $1 \leq m_{ee} \leq 3 \text{ GeV}/c^2$ are dominated by the correlated pairs from heavy-flavor decays, where the initial productions are modified due to energy loss in the medium. The production of direct thermal dielectrons lies on the top of correlated pairs from heavy-flavor decays, where the invariant mass of dielectrons can be the proxy of the temperature of the medium.

In 2017, we made good progress in the measurements of low-mass dielectrons at pp collisions at $\sqrt{s} = 7 \text{ TeV}$ and Pb-Pb collisions at $\sqrt{s_{NN}} = 5.02 \text{ TeV}$.

Data analyses were done with 370M pp MB collisions at $\sqrt{s} = 7 \text{ TeV}$ and 80M Pb-Pb MB collisions at $\sqrt{s_{NN}} = 5.02 \text{ TeV}$ collected by ALICE [3]. In pp collisions, electrons are identified from $p_T \geq 0.2 \text{ GeV}/c$ by using dE/dx in the Time Projection Chamber (TPC) and additional requirement by the Time-of-Flight detector (TOF) is required in case of $p_T \geq 0.4 \text{ GeV}/c$. In Pb-Pb collisions, electrons are identified from $p_T \geq 0.4 \text{ GeV}/c$ by requiring TPC+TOF. The hadron contamination in pp , and Pb-Pb, is at most 1% and 10%, respectively, for all p_T range. Electrons from photon conversions are rejected by vetoing the sharing of clusters in the Inner Tracking System (ITS) and orientation pair angle in the magnetic field. After making electron and positron pairs (unlike-sign pairs), the combinatorial background is subtracted by using the like-sign pairs, corrected for acceptance difference between unlike and like-sign pairs, which is estimated by using mixed event pairs. The subtracted data are corrected for efficiency, which is determined via Monte Carlo (MC) simulations including a realistic description of the detector responses.

Figure 1 shows the corrected dielectron invariant mass spectrum and the expected dielectron decays from known hadronic sources (hadronic cocktail). Those hadronic contributions are based on measured differential cross-sections of π^0 , η , ϕ , and J/ψ in pp collisions [4–6]. The contributions from remaining light-hadrons are based on m_T scaling. The correlated pairs from heavy-flavor decays are estimated by using PYTHIA simulations scaled by the charm/bottom cross section measured by ALICE [7].

Figure 2 and Figure 3 show pair DCA (Distance-of-

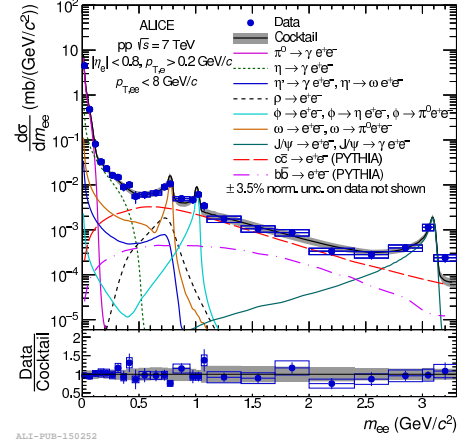


Figure 1. Dielectron invariant mass spectrum in pp collisions at $\sqrt{s} = 7 \text{ TeV}$ compared to the hadronic cocktail

Closest-Approach) distributions for different invariant mass ranges, $1.1 \leq m_{ee} \leq 2.7 \text{ GeV}/c^2$ and $2.7 \leq m_{ee} \leq 3.3 \text{ GeV}/c^2$, respectively. Template of DCA distributions for

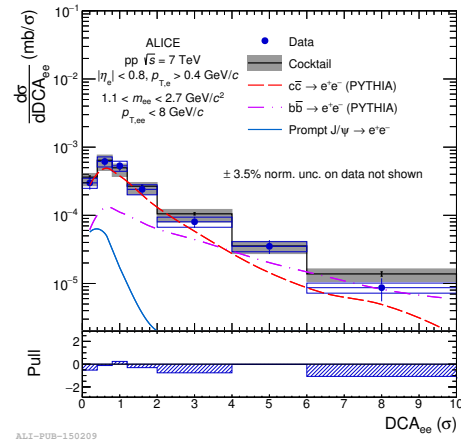


Figure 2. dielectron Pair DCA distribution for $1.1 \leq m_{ee} \leq 2.7 \text{ GeV}/c^2$, where this region is dominated by heavy flavor decays as shown in Fig. 1.

heavy flavors (charm and beauty quarks) and prompt and non-prompt J/ψ are created by using PYTHIA event generators, that tuned various charm hadron yields, and full detector simulations. As is shown in Fig. 2 and Fig. 3, pair DCA distributions for these mass ranges are well described by the contributions from heavy flavor decays and separation between charm and beauty hadron decays is also well feasible. Furthermore, prompt J/ψ and heavy flavor decays are well distinguished that means that direct thermal photons in Pb-Pb collisions can be separated from heavy flavor

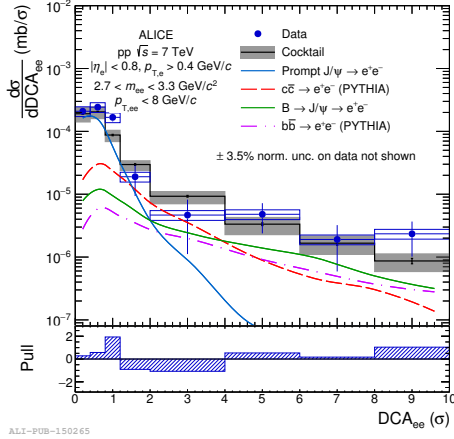


Figure 3. dielectron Pair DCA distribution for $2.7 \leq m_{ee} \leq 3.3$ GeV/c^2 , where this region is dominated by non-prompt J/ψ decays ($B \rightarrow J/\psi$).

decays by using pair DCA distribution.

Figure 4 shows the dielectron invariant mass spectrum in MB Pb-Pb collisions at $\sqrt{s_{\text{NN}}} = 5.02$ TeV and comparison with known hadronic cocktails. The heavy flavor contributions in cocktail are estimated by assuming binary scaling of heavy flavor production in pp collisions at the same collision energy. Due to the current statistical and systematic uncertainties, current dielectron spectrum in Pb-Pb collisions does not have enough sensitivity to discuss possible modification of dielectron production in Pb-Pb collisions.

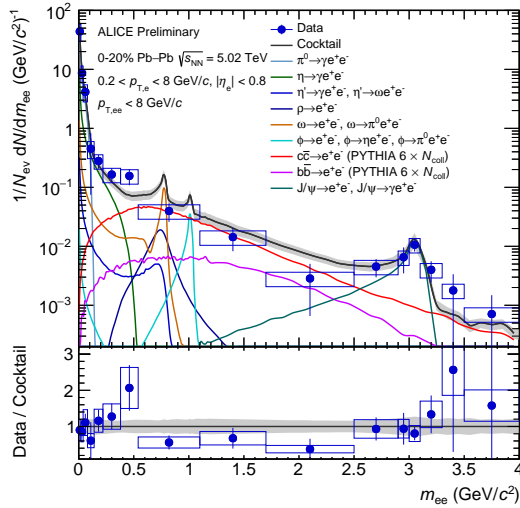


Figure 4. Dielectron invariant mass in MB Pb-Pb collisions at $\sqrt{s_{\text{NN}}} = 5.02$ TeV and comparison with comparison with known hadronic sources, where heavy flavor contributions are estimated from heavy flavor production in pp collisions scaled by binary nucleon-nucleon collisions.

ALICE will upgrade some key detectors and data acquisition systems for RUN 3 to inspect 50 kHz Pb-Pb collisions [8] that is $\times 100$ larger than in RUN 2. CNS has been working on the TPC upgrade, which utilizes the Gas Electron Multipliers (GEM) in the readout chamber. CNS joins

the mass testing of the real-size GEM foils at CERN in 2017 and started some activities in online data processing via GPU (Graphical Processing Unit).

ALICE has measured dielectron production in pp and Pb-Pb collisions at 7 TeV and 5.02 TeV per nucleon pairs, respectively. In pp collisions, the corrected invariant mass spectrum is consistent with known hadronic sources. Pair DCA analysis demonstrates the usefulness of dielectron channels for heavy-flavor measurements. Dielectron measurements in MB Pb-Pb collisions at 5.02 TeV shows that the corrected yield is not significantly larger than the known hadronic sources and not yet sensitive to the modification of the ρ meson due to large uncertainty and large charm contributions.

References

- [1] E. V. Shuryak, Phys. Lett. **B 78** (1978) 150.
- [2] R. Rapp and J. Wambach, Advances in Nuclear Physics, **25**, pp. 1–205 (2000).
- [3] K. Aamodt et al. (The ALICE Collaboration) JINST, **3**, S08002 (2008).
- [4] K. Koch (The ALICE Collaboration), Nucl. Phys. A **855**, pp. 281–284 (2011).
- [5] B. Abelev et al. (The ALICE Collaboration), Eur. Phys. J. **C72**, p. 2183 (2012).
- [6] K. Aamodt et al. (The ALICE Collaboration), Phys. Lett. **B 704**, pp. 442–455 (2011).
- [7] B. Abelev et al. (The ALICE collaboration), JHEP01, 128 (2012).
- [8] B. Abelev et al. (The ALICE Collaboration), J. Phys. G, **41**, 087002 (2014).

J/ψ production in p–Pb collisions at $\sqrt{s_{NN}} = 5.02$ TeV

S. Hayashi, and T. Gunji

Center for Nuclear Study, Graduate School of Science, University of Tokyo

The suppression of charmonium production in ultra-relativistic heavy-ion collisions is one of the most compelling signatures of the formation of the Quark–Gluon Plasma (QGP), a state of matter composed of quarks and gluons [1]. The high colour-charge density in the QGP prevents the formation of charmonium states by screening the charm and anti-charm quark pairs. While at SPS and RHIC energies, a strong suppression in central heavy-ion collisions has been observed and can be described by the color screening, at LHC energies a regeneration mechanism has to be introduced to describe the centrality dependence of charmonium production [2]. It is also expected that the nuclear effects, which are not related to QGP effects, have an impact on charmonium production. For example, the modification of the Parton Distribution Function (PDF) of heavy nuclei affects the charm pair production [3]. Since J/ψ mesons are dominantly produced via gluon fusion, the J/ψ production is particularly sensitive to the possible shadowing of the gluon PDF in nuclei.

Previous measurements in proton–nucleus collisions showed a change in the charmonium production attributed to these nuclear matter effects [4, 5]. ALICE measured J/ψ production as a function of rapidity in p–Pb collisions at $\sqrt{s_{NN}} = 5.02$ TeV, where the suppression was consistent with the expectation of gluon shadowing. This report presents preliminary results on J/ψ production in minimum bias (MB) p–Pb collisions at $\sqrt{s_{NN}} = 5.02$ TeV newly recorded in the year 2016. The statistics increased by a factor of 6 compared to the previous results and consequently these results are used to constrain nuclear matter effects in heavy-ion collisions.

The kinematical acceptance of electron candidates is $p_T > 1$ GeV/c and $|\eta_{lab}| < 0.9$. Electrons are identified in the Time Projection Chamber via their specific energy loss in the gas volume. Additionally, electrons forming low mass pairs ($m_{ee} < 0.05$ GeV/c²) with other electrons are removed to remove pairs from photon conversions.

The raw number of J/ψ mesons is evaluated after the estimation and subtraction of the background. Background contributions are combinatorial background, which comes from unphysical combinations of electrons and positrons, and background pairs from combinations of correlated semi-leptonic decay pairs of D and B mesons or electrons from jet fragmentation. The combinatorial background is estimated by building dielectron pairs from different events with a similar event topology: so-called mixed-event pairs. These pairs are unphysical and do not include any correlation except the pair acceptance. To take into account the correlated background, the mixed event pairs are weighted with an exponential function, which approximates the mass dependence from semi-leptonic heavy-flavour decays. Signal pairs are then calculated after background subtraction

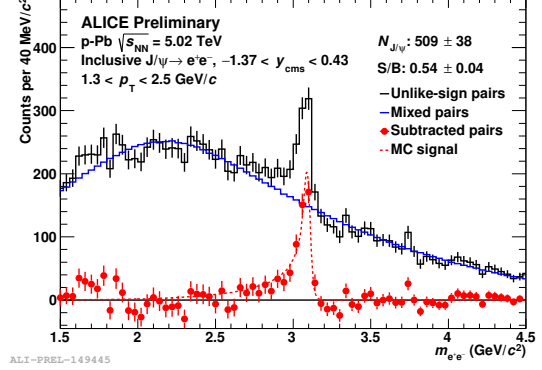


Figure 1. The invariant mass spectrum of opposite sign electron pairs (black lines), the background estimation from weighted mixed event pairs (blue lines), and the background subtracted pairs (red marker).

by bin counting within the mass window $2.92 < m_{ee} < 3.16$ GeV/c². For integrated p_T and centrality, a total of 1953 ± 67 raw J/ψ is available for the analysis. The raw number of J/ψ mesons is then corrected for the detector efficiency. The acceptance and detector efficiencies are evaluated based on the Monte Carlo simulations, where MB p–Pb collisions are simulated by EPOS-LHC and J/ψ signal is inserted with a realistic p_T and rapidity shape based on previous measurements [6]. The pair efficiency is about 7.2% in the lowest p_T bin and increases towards 13.0% towards the highest p_T bin.

The nuclear modification factor R_{pPb} as a function of p_T is defined as

$$R_{pPb}(p_T) = \frac{d^2 N_{pPb}^{J/\psi} / dp_T dy}{\langle T_{pPb} \rangle \times d^2 \sigma_{pp}^{J/\psi} / dp_T dy}, \quad (1)$$

where $d^2 N_{pPb}^{J/\psi} / dp_T dy$ is the yield of J/ψ in p–Pb collisions, $\langle T_{pPb} \rangle$ is the nuclear thickness function and $d^2 \sigma_{pp}^{J/\psi} / dp_T dy$ is the p_T differential reference cross section of J/ψ in pp collisions at the corresponding collision energy. No measurement of the cross section $d^2 \sigma_{pp}^{J/\psi} / dp_T dy$ was carried out with the previous pp dataset at $\sqrt{s} = 5.02$ TeV. The estimation of the p_T differential cross section follows a procedure described in [4]. First, the p_T integrated cross section $d\sigma_{pp}^{J/\psi} / dy$ is calculated from an interpolation of data taken at mid-rapidity at collision energies of $\sqrt{s} = 0.2$ TeV, 1.96 TeV, 2.76 TeV, and 7 TeV. For the interpolation, a set of empirical functions was used and the interpolated cross section results in $BR \times d\sigma_{pp}^{J/\psi} / dy = 369.1 \pm 36.0(stat.) \pm 49.1(syst.)$ nb. Afterwards the p_T differential cross section is estimated by a parametrisation as a function of $p_T / \langle p_T \rangle$.

Several sources of systematic uncertainties are considered for the resulting nuclear modification factor R_{pPb} . The

uncorrelated sources are identified to be the signal extraction including the background estimation (about 5%), the track selection (3–5%) and the interpolation procedure of the pp reference cross section (6–16% increasing with p_T). Correlated uncertainties, i.e. acting in the same direction within the full p_T range, are from the pp reference (16.6%) and from the T_{pPb} normalisation ($\sim 3\%$). The correlated uncertainty of the pp reference spectrum originates from the poorly known p_T integrated cross section interpolated to $\sqrt{s} = 5.02$ TeV as well as from the interpolated mean transverse momentum of the J/ψ . The uncorrelated uncertainty of the pp reference originate from the statistical uncertainty of previous measurements.

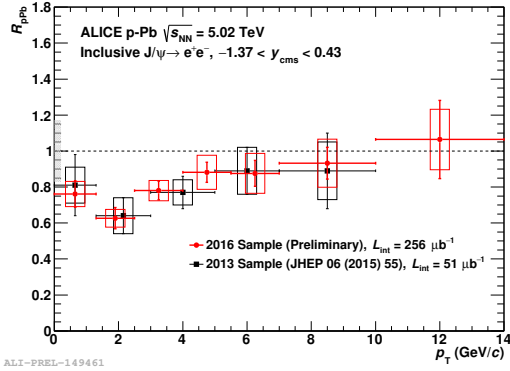


Figure 2. Nuclear modification factor as a function of the transverse momentum p_T in MB p–Pb collisions at $\sqrt{s_{NN}} = 5.02$ TeV is shown for the previous dataset (black squares) [4] and the preliminary result based on the 2016 data sample (red circles).

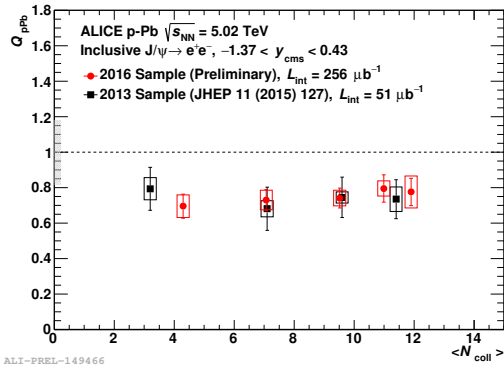


Figure 3. Nuclear modification factor as a function of $\langle N_{coll} \rangle$ at $\sqrt{s_{NN}} = 5.02$ TeV is shown for the previous dataset (black squares) [5] and the preliminary result based on the 2016 data sample (red circles).

The preliminary inclusive J/ψ R_{pPb} as a function of p_T is presented in Fig. 2. At low p_T , the J/ψ yield is suppressed in p–Pb collisions compared to the binary scaled reference cross section in pp collisions. The suppression then decreases with increasing p_T and is consistent with binary scaling of the pp cross section for $p_T > 4$ GeV/c. The results are compared to the published results from the LHC data taking in 2013 and are shown to be consistent within

the given p_T range. Moreover, it has been possible to extend the p_T reach of the measurement in this analysis to 14 GeV/c.

Figure 3 shows the nuclear modification factor of inclusive J/ψ as a function of N_{coll} , which is the number of binary collisions in a p–Pb collision, The new preliminary result is consistent with the ALICE published result from the LHC data taking in 2013 [5]. The inclusive J/ψ Q_{pPb} shows a J/ψ suppression, without a strong centrality dependence.

We presented results on inclusive J/ψ production in minimum bias p–Pb collisions at mid-rapidity at $\sqrt{s_{NN}} = 5.02$ TeV measured with ALICE at the CERN LHC. The nuclear modification factor of inclusive J/ψ as a function of p_T shows a suppression of the yield in p–Pb collisions at low p_T which decreases at higher p_T . The statistical uncertainty is significantly reduced compared to the previous measurements and will help to constrain effects arising from the modification of the initial state of the nucleon in heavy-ion collisions.

References

- [1] T. Matsui and H. Satz, Phys. Lett. B **178** (1986) 416.
- [2] ALICE Collaboration, B. Abelev *et al*, Phys. Rev. Lett. **109** (2012) 072301
- [3] R. Vogt, Phys. Rev. C **81** (2010) 044903
- [4] ALICE Collaboration, J. Adam *et al*, JHEP **06** (2015) 055
- [5] ALICE Collaboration, J. Adam *et al*, JHEP **11** (2015) 127
- [6] T. Pierog, I. Karpenko, J. M. Katzy, E. Yatsenko, and K. Werner, Phys. Rev. C **92** (2015) 034906

Long-range correlations in p -Pb collisions with ALICE

Y. Sekiguchi and T. Gunji for the ALICE Collaboration

Center for Nuclear Study, Graduate School of Science, The University of Tokyo

1. Introduction

Measurement of the correlations in the particle production as a function of the azimuthal angle and rapidity is very useful for investigating particle production in high-energy nucleus-nucleus collisions. The long-range correlations in the rapidity space in near-side angular pairs of dihadrons were firstly observed in Au-Au collisions at $\sqrt{s_{NN}}=200$ GeV at RHIC [1, 2]. The long-range correlations are derived from the collective expansion of the initial geometry fluctuations. Unexpectedly, a similar structure has also been observed in high-multiplicity pp collisions at 7 TeV by the LHC-CMS experiment [3]. The high-density gluon fields in small x (Bjorken x) of nucleus and the collision of two high-density gluon sheets can explain the long-range correlations [4]. The measurements of the particle productions with large rapidity gaps and the centrality dependence are important for quantifying the collective expansion. This analysis aims to explore the partonic collectivity by measuring long-range two-particle correlations using forward detectors in p -Pb collisions at $\sqrt{s_{NN}}=5.02$ TeV.

2. Analysis

The minimum bias data of p -Pb collisions at $\sqrt{s_{NN}}=5.02$ TeV in 2016 are used (~ 600 M events). The main subsystems in ALICE used in this analysis are time projection chamber (TPC) and Forward Multiplicity Detector (FMD). The TPC is used for tracking of charged particles and particle identification. Its acceptance covers 2π in azimuthal angle and a pseudo-rapidity interval $|\eta| < 0.9$. The FMD is composed of three arrays at $-3.4 < \eta < -1.7$, $1.7 < \eta < 3.68$, and $3.68 < \eta < 5$, respectively (Table.1). The position of the

Array	Ring	ϕ segments	η coverage
FMD1	-	20	3.68 - 5.03
FMD2	FMD2i	20	2.28 - 3.68
	FMD2o	40	1.70 - 2.29
FMD3	FMD3i	20	-2.29 - -1.70
	FMD3o	40	-3.40 - -2.01

Table 1. FMD pseudo rapidity coverage and azimuthal segments.

reconstructed vertex along the beam direction is required to be within 10 cm from the detector center. To define centrality, VZEROA detector which is located in the Pb-going direction is used. The correlations between trigger particles and associated particles are measured as a function of the azimuthal angle difference $\Delta\phi$ and pseudo-rapidity difference $\Delta\eta$. The trigger particles are unidentified charged hadrons detected in TPC, while FMD channels are used as associated particles. FMD cannot measure transverse momentum p_T and the multiplicity in each channel is used as the number of tracks in the average ϕ and η of each chan-

nel. The correlation function as a function of $\Delta\eta$ and $\Delta\phi$ between two charged particles is defined as:

$$\frac{1}{N_{\text{trig}}} \frac{d^2 N_{\text{asso}}}{d\Delta\eta d\Delta\phi} = \frac{S(\Delta\eta, \Delta\phi)}{B(\Delta\eta, \Delta\phi)} \quad (1)$$

where N_{trig} is the total number of triggered particles in the event class, the signal distribution $S(\Delta\eta, \Delta\phi) = \frac{1}{N_{\text{trig}}} \frac{d^2 N_{\text{same}} \times w_i}{d\Delta\eta d\Delta\phi}$ is the associated yield per trigger particle from the same event, and the background distribution $B(\Delta\eta, \Delta\phi) = \alpha \frac{d^2 N_{\text{mixed}} \times w_i}{d\Delta\eta d\Delta\phi}$ accounts for pair acceptance and pair efficiency. It is constructed by taking the correlations between trigger particles in one event and associated particles from other events in the same event class. w_i is the multiplicity in each FMD channel. The α factor is chosen so that it is unity at the maximum bin. Figure 1 shows the associated yield per unidentified hadron trigger particles for TPC-FMD1 at $4.7 < \eta < 4.9$ (top) and TPC-FMD3 (at $-3.4 < \eta < -3.1$ (bottom) with $0.3 < p_{T,\text{trig}} < 8$ GeV in 0-20% and 60-100% centrality classes, respectively. Centrality class corresponds to the collision impact parameter b . The long-range correlations in near-side ($-\pi/2 < \Delta\phi < \pi/2$), called ridge, can be observed in 0-20% events both for TPC-FMD 1(Pb-going) and TPC-FMD3 (p-going), while it is not significant in 60-100% events.

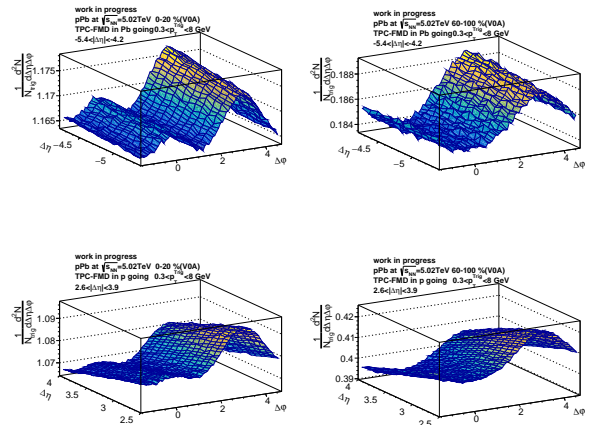


Figure 1. Associated yield per trigger particle for TPC-FMD1,2 (top) and TPC-FMD3 (bottom) for the 0-20% (left) and 60-100% (right) event classes.

The correlation function in the peripheral collisions (60-100%) is subtracted from that in the central collisions (0-20%) to reduce the auto-correlations from jets. Figure 2 shows the projection onto $\Delta\phi$ in central events after subtraction ((0-20%)-(60-100%)) for TPC-FMD1 (left) and TPC-FMD3 (right). Long range structure on both the near and away side is observed. To quantify the near-side and away-side excess structures, the Fourier function is used to fit to

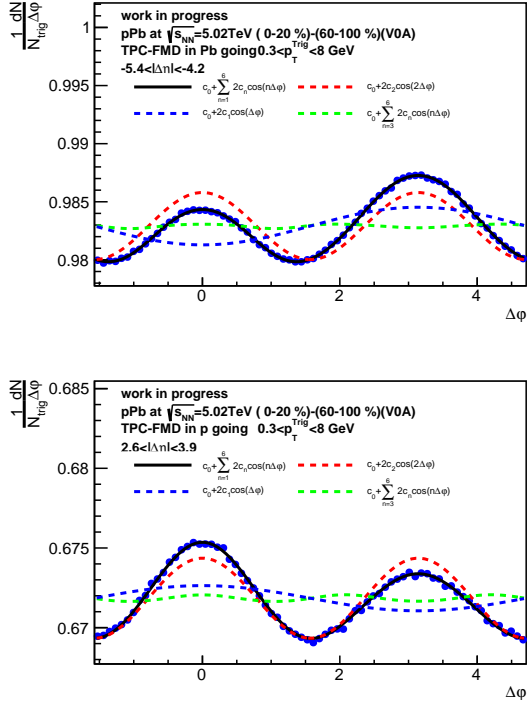


Figure 2. Projection of the subtracted correlation functions of the associated FMD1 (top) and FMD3 (bottom) yield per trigger particle in TPC with $0.3 < p_{T, trig} < 8$ GeV.

the data.

$$\frac{1}{N_{trig}} \frac{dN_{asso}}{d\Delta\phi} = a_0 + 2 \sum_{n=1}^6 \cos(n\Delta\phi). \quad (2)$$

From the relative modulations $V_n(2PC) = a_n / (a_0 + b)$, for example, the azimuthal anisotropy in FMD1 can be obtained as following. b is the baseline which is the minimum of the 60-100% event class.

$$v_{n, FMD1} = \sqrt{\frac{V_n(TPC - FMD1)V_n(FMD1 - FMD3)}{V_n(TPC - FMD3)}} \quad (3)$$

Figure 3 shows the extracted v_2 as a function of η for different event class. The v_2 includes contamination from secondary particles. The multiplicity in each segment of FMD contains primary particles and secondary particles as shown in Fig.4. v_2 distribution reflects the secondary distribution. The estimation of contamination from secondary particles in v_n is ongoing by Monte Carlo simulation.

3. Summary and Outlook

v_2 as a function of η is measured by two-particle correlations between TPC tracks and FMD channels in p-going and FMD channels in Pb-going in p -Pb collisions at $\sqrt{s_{NN}} = 5.02$ TeV. The finalizing correction of contamination from secondary particles is ongoing to extract primary $v_2(\eta)$.

References

- [1] STAR Collaboration, Phys. Rev. **C80** (2009) 064912.
- [2] PHOBOS Collaboration, Phys. Rev. Lett. **104** (2010) 062301.

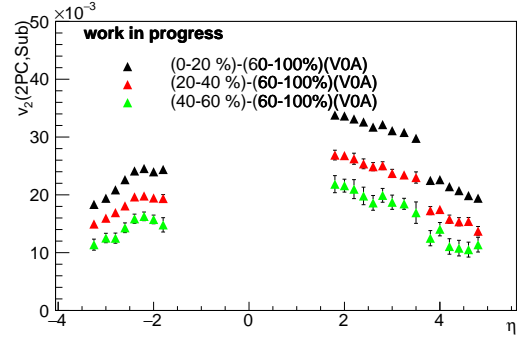


Figure 3. v_2 as a function of η .

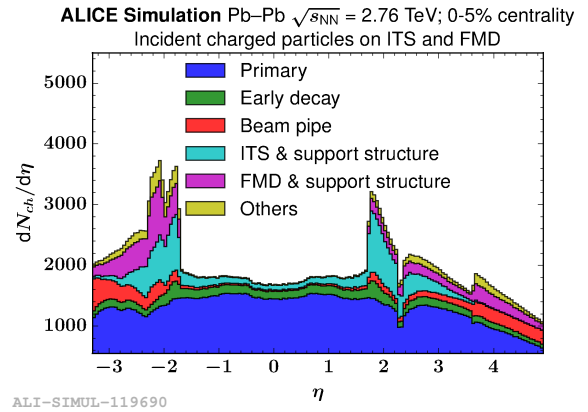


Figure 4. Production origin or incident charged particles on the FMD and ITS.

- [3] CMS Collaboration, JHEP 09 (2010) 091.
- [4] K. Dusling and R. Venugopalan, Phys. Rev. D **87** (2013) 054014.
- [5] ALICE Collaboration, Phys. Lett. B, **726** (2013) 164-177.

Direct photon measurement via external conversions in pp and p-Pb collisions at LHC-ALICE

H. Murakami, T. Gunji^a, for the ALICE collaboration

Department of Physics, University of Tokyo

^a*Center for Nuclear Study, Graduate School of Science, University of Tokyo*

1. Introduction

The observations of collective behavior of hadrons in high multiplicity pp and p-Pb collisions at the LHC is unexpected discoveries in recent years [1, 2]. Up to now, it is not clear if it indicates the formation of thermalized systems such as new state of matter, quark-gluon plasma (QGP) even in small collision systems [3] or it is explained by dynamics of initial gluon field [4]. If the QGP is created in high-multiplicity events in small colliding systems, the thermal photons are expected to be emitted from the QGP. Direct photon is an ideal probe to diagnose the thermalized system since photon is sensitive to thermodynamical variables such as temperature.

In this study, we looked for the direct photon in pp at $\sqrt{s} = 5.02$ TeV and p-Pb collisions at $\sqrt{s_{NN}} = 5.02$ TeV to prove that the QGP is created in small systems. The former measurement is compared to the other in which direct photon is observed. It will provide an baseline for the understanding of high-multiplicity pp and p-Pb collisions. This report presents the status of the direct photon measurement in pp collisions.

2. Analysis overview

In hadronic collisions, photons are emitted at every stage of the space-time evolution. The emitted photons are categorized into two groups: direct photons and decay photons. The former photons include the thermal radiations and photons produced in elementary hard QCD processes such as $q\bar{q} \rightarrow g\gamma$ and $qg \rightarrow q\gamma$. The latter photons are decay photons from $\pi^0/\eta \rightarrow \gamma\gamma$. To extract direct photon signal, the subtraction technique is used. In this method, we first deduce the inclusive photon spectrum and then statistically subtract the spectra of decay photons. The invariant yield of direct photons $\gamma_{\text{dir}}(p_T)$ can be expressed in terms of the inclusive photons $\gamma_{\text{inc}}(p_T)$ and that of decay photons $\gamma_{\text{dec}}(p_T)$:

$$\begin{aligned}\gamma_{\text{dir}}(p_T) &= \gamma_{\text{inc}}(p_T) - \gamma_{\text{dec}}(p_T) \\ &= (1 - R_\gamma^{-1}(p_T)) \cdot \gamma_{\text{inc}}(p_T)\end{aligned}\quad (1)$$

where $R_\gamma(p_T) = \gamma_{\text{dec}}(p_T)/\gamma_{\text{inc}}(p_T)$ is the fraction of photons from π^0 and η decays. If $R_\gamma(p_T) > 1$, it implies direct photon signal. In order to obtain decay photon spectra, π^0 and η which are the major sources of decay photons are deduced by photon conversion method. Other sources are estimated by using m_T scaling [5] from measured π^0 and η spectra.

3. Experimental setup

In this analysis, photons are reconstructed via e^+e^- pairs which converted in a detector material. The method is advantageous in identifying photons down to low p_T , where

thermal photons dominate. Tracking is made by using ALICE central detector system consists of the Inner Tracking System (ITS), the Time Projection Chamber (TPC). Photons convert into e^+e^- pairs in the material of the ITS and TPC. The event multiplicity is estimated with V0 detectors, which are made of two arrays of scintillation counters placed on forward and backward of the ALICE interaction point. Details of ALICE detectors can be found in [6]. V0 detectors also provide trigger information.

4. Data analysis

In 2015, ALICE collected collected over 128 M events in MB pp collision at $\sqrt{s} = 5.02$ TeV. The e^+e^- pairs from photon conversions are reconstructed with the V^0 reconstruction method which enables one to find particles from offvertex decay. Electron was identified by the dE/dx information of TPC. To improve photon purity, several selection criteria, like constraints on invariant mass, opening angle, and topological cuts are applied. Photons from out-of-bunch pileup is statistically subtracted by using the distance closest approach (dca) in the z-direction. Inclusive photon spectrum $\gamma_{\text{inc}}(p_T)$ is given by as follows:

$$\gamma_{\text{inc}}(p_T) = \gamma_{\text{corr.}}(p_T) \times P(p_T) \times \frac{1}{\epsilon(p_T)} \times \frac{1}{C(p_T)}, \quad (2)$$

where $\gamma_{\text{corr.}}(p_T)$ denotes corrected raw photon spectra after out-of-bunch pileup correction and secondary photon contribution, $P(p_T)$ is the purity of photon sample, $\epsilon(p_T)$ is the reconstruction efficiency, $C(p_T)$ is conversion probability. Correction factors are evaluated using Monte Carlo simulations. The purity, the reconstruction efficiency and the conversion probability are above 98%, up to 55% and 9%, respectively. Figure 1 shows an inclusive photon spectrum. The decay photon spectra $\gamma_{\text{dec}}(p_T)$ is obtained by using measured π^0 and η spectra in pp collisions as shown in Figure 2. Here the distributions of π^0 and η are parametrized from a fit to the measured spectra with a Modified Hagedorn function [7]. Once π^0 , η and other particles are generated, then they decay into photons using Pythia decayer. Figure 3 shows the generated distributions of decay photon for respective hadronic sources. Dominant decay photon sources are π^0 , η , η' and ω .

5. Summary and outlook

In this report, current status of direct photon measurement in pp collisions are presented. Currently, estimation of systematic uncertainties and systematic checks are ongoing. Also, the analysis of p-Pb collisions, has been started. Multiplicity dependent π^0 and η spectra measurement has been done and a cocktail simulation is ongoing.

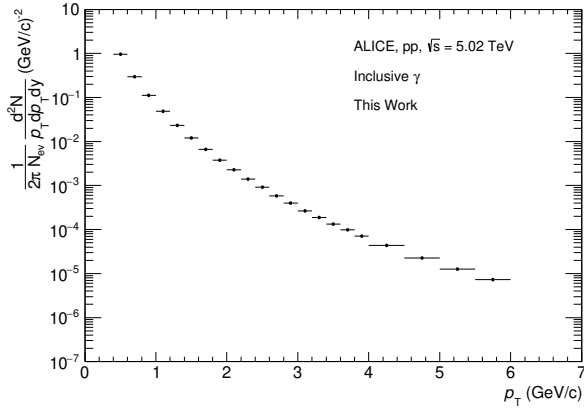


Figure 1. Inclusive photon spectrum in pp collisions at $\sqrt{s} = 5.02$ TeV

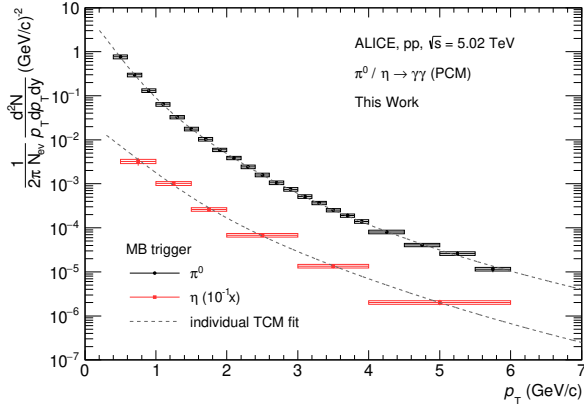


Figure 2. Differential invariant yield of π^0 and η meson in pp collisions at $\sqrt{s} = 5.02$ TeV. Dashed lines show individual fit to respective distributions. The fitting function is Two Component Fit.

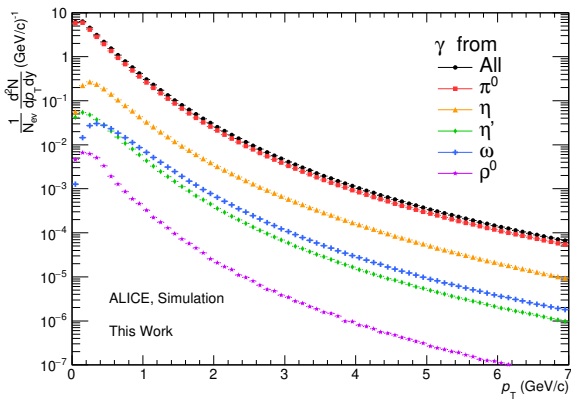


Figure 3. The per event yield of decay photons from various mesons.

References

- [1] CMS collaboration, J. High Energy Phys. **09** (2010) 091.
- [2] CMS collaboration, Phys. Lett. B **718** (2013) 795.
- [3] C. Shen *et al*, Phys. Rev. Lett. **116** (2016) 072301.
- [4] K. Dusling *et al*, Phys. Rev. D **87**. (2013) 054014.
- [5] WA80 collaboration, Phys. Lett. B **361** (1995), 14.
- [6] ALICE collaboration, J. High Energy Phys. **09** (2010) 091.
- [7] PHENIX collaboration, A. Adare *et al*, Phys. Rev. C **81** (2010) 034911.

Accelerator and Instrumentation

Commissioning of the OEDO beamline

S. Michimasa, J.W. Hwang, K. Yamada^a, S. Ota, M. Dozono, N. Imai, K. Yoshida^a, Y. Yanagisawa^a, K. Kusaka^a, M. Ohtake^a, M. Matsushita, D.S. Ahn^a, O. Beliuskina, N. Chiga^a, K. Chikaato^b, N. Fukuda^a, S. Hayakawa, E. Ideguchi^c, K. Iribe^d, C. Iwamoto, S. Kawase^e, K. Kawata, N. Kitamura, S. Masuoka, H. Miyatake^f, D. Nagae^a, R. Nakajima, T. Nakamura^g, K. Nakano^e, S. Omika^a, H. Otsu^a, H. Sakurai^{a,h}, P. Schrock, H. Shimizu, Y. Shimizu^a, T. Sumikama^a, X. Sun^a, D. Suzuki^a, H. Suzuki^a, M. Takaki, M. Takechi^b, H. Takeda^a, S. Takeuchi^g, R. Tsunoda, H. Wang^a, Y. Watanabe^e, Y.X. Watanabe^f, K. Wimmer^h, K. Yako, H. Yamaguchi, L. Yang, H. Yoshida^d, and S. Shimoura

Center for Nuclear Study, Graduate School of Science, University of Tokyo

^a*RIKEN Nishina Center*

^b*Dept. of Physics, Niigata University*

^c*RCNP, Osaka University*

^d*Dept. of Physics, Kyushu University*

^e*Dept. of Advanced Energy Engineering Science, Kyushu University*

^f*Wako Nuclear Science Center, IPNS, KEK*

^g*Dept. of Physics, TITECH*

^h*Dept. of Physics, the University of Tokyo*

The OEDO system is a new beamline proposed for providing slow-down, well-focusing RI beams [1] for high-energy RI facilities with in-flight separators. The OEDO is an abbreviation of **Optimized Energy Degrading Optics** for RI beam. The idea of OEDO is to manipulate a degree-of-freedom in the longitudinal phase space of RI beam. To obtain a beam with a small spot size and a small energy spread, the OEDO system transforms the spreads of horizontal position and angle of the beam to the timing spread, which corresponds to the rotation of the phase space ellipse on the position- (angle-) timing plane to obtain a small position (angle) spread. The previous reports [2–4] have already described the construction and simulation works of the OEDO beamline, where the details on the design of the OEDO were also written. This report describes the results of its commissioning experiment and discusses its performance in RI beam productions.

The commissioning run of the OEDO has been held in June 2017 using $^{77,79}\text{Se}$, ^{93}Zr and ^{107}Pd beams, which were produced from 345-MeV/u ^{238}U primary beam through its fission-fragment reactions. The beamline detectors were installed at each focus point to identify the RI particles and to diagnose the beam profile. Figure 1 shows a synthetic photograph taken between FE9 of the OEDO beamline and S2 of the SHARAQ spectrometer, which is the second half of the beamline. The indications of FE9, FE10, FE11, S0, S1 and S2 show places of the focal planes of the beamline and the spectrometer. The secondary reaction targets for reaction measurements of RI beams are placed at the S0 focus, and the mono-energetic degraders for slowdown of RI beams are installed at FE9. The phase-space rotation of the RI beams is held between FE9 and FE11, and the beamline FE11 and S0 were used for the beam tagging by its nuclear species and velocity. The reaction products from

the secondary reactions are analyzed by the SHARAQ spectrometer. In the commissioning experiment of the OEDO, we have examined the performances in energy compaction, beam focusing by using those RI beams.

The energy compaction of the RI beams were tuned by using the angle-variable degrader [5] installed at FE9. Figure 2 shows the result of energy compaction performed using the variable-angle degrader system to obtain 45-MeV/u ^{79}Se ions from the 170-MeV/u beam. These results demonstrate that, without aggravating the energy spread through energy degradation, a low-energy RI beam is obtained by tuning the angle of the degrader. The beam energies in front of and behind the degrader are $172.8 \pm 3.4(\sigma)$ and $46.3 \pm 2.7(\sigma)$ MeV/u, respectively. Generally, it is difficult that the actual ion optics is identical to the design, and also the wedge angle of a mono-energetic degrader almost mismatches the design. However, the variable-angle degrader system can be controlled to match the real-time situation of the ion optics. Therefore, we can obtain the best setting of energy compaction against those mismatching situations. The performance of this degrader system will be described in detail in Ref. [5].

The beam focusing of slowed-down RI beams was examined by the 50-MeV/u ^{77}Se beams energetically degraded from 170 MeV/u at FE9. Figure 3 shows the FE11 focusing through the RFD. In the figure, the angle of the mono-energetic FE9 degrader was not optimized for energy compaction. The red and black histograms show the horizontal position of the beam at the FE11 focus with and without the RFD in operation, respectively. The high voltage is 280 kV and the phase is optimized the focusing of the ^{77}Se beam. The filled histogram is obtained from a simulation using the ion-optical and RFD parameters in the experiment. The simulation well-reproduces the ion distribution measured at



Figure 1. Second half of OEDO beamline and SHARAO spectrometer.

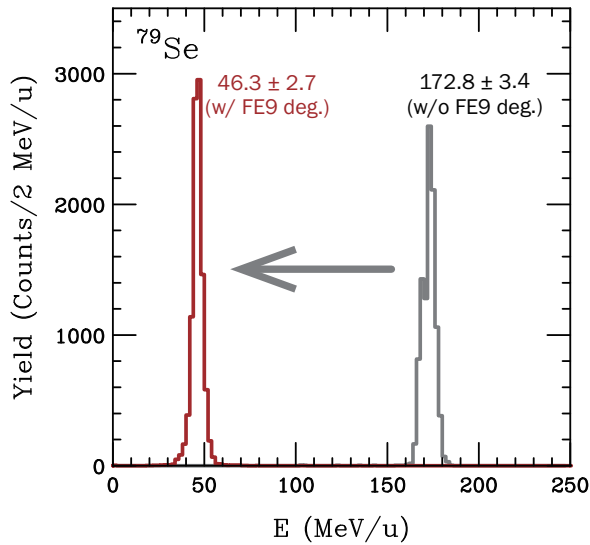


Figure 2. Energy compaction from 172 to 45 MeV/u by using a wedge-shaped degrader. The red (black) histogram shows the energy distribution of the ^{79}Se beam with (without) the FE9 degrader. The thickness and angle of the degrader were set to be 6 mm and 25 mrad, respectively.

FE11. Therefore, the results demonstrate that the ion optics of the OEDO beamline are properly adjusted to achieve the design goal of the ion optics. Finally, by using the RFD, the OEDO beamline can provide an achromatic focus at FE11 with a horizontal width of 13.5 mm FWHM.

After the commissioning experiments, we have performed two physics experiments [6, 7] in October and November 2017, based on the ion optics and beam tuning procedures developed by the commissioning. The analysis on ion optics of the OEDO beamline is still in progress, and is expected to feed back to analyses on those physics experiments.

This work was funded by ImpACT Program of Council for Science, Technology and Innovation (Cabinet Office, Government of Japan).

References

- [1] S. Shimoura *et al.*, CNS Annual Report 2013, CNS-REP-93, 55 (2015).
- [2] S. Michimasa *et al.*, CNS Annual Report 2014, CNS-REP-94, 47 (2016).

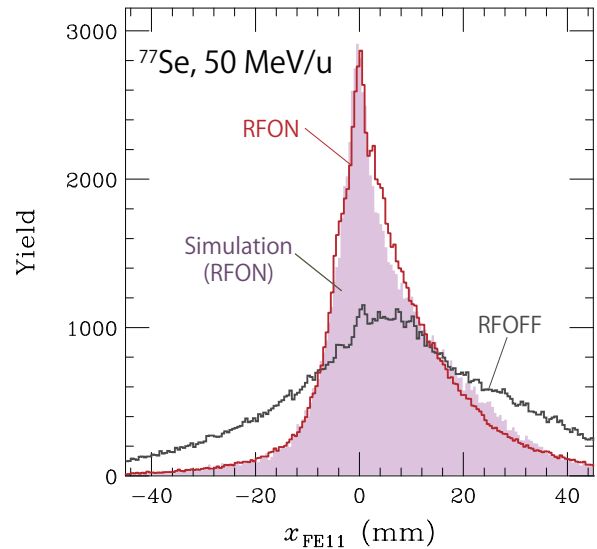


Figure 3. The horizontal hit positions of 50-MeV/u ^{77}Se at FE11. The red (black) histogram is obtained with (without) the RFD operation ($V_0 = 280$ kV). The filled histogram is an estimate based on a simulation with the same parameters as those for the beamline elements.

- [3] M. Matsushita *et al.*, CNS Annual Report 2014, CNS-REP-95, 49 (2016).
- [4] S. Michimasa *et al.*, CNS Annual Report 2016, CNS-REP-96, 39 (2018).
- [5] J.W. Hwang *et al.*, CNS Annual Report 2017, CNS-REP-97, 39 (2019).
- [6] N. Imai *et al.*, CNS Annual Report 2017, CNS-REP-97, 1 (2019).
- [7] M. Dozono *et al.*, CNS Annual Report 2017, CNS-REP-97, 3 (2019).

Angle-Tunable Degradator for OEDO Beamline

J.W. Hwang, S. Michimasa, S. Ota, M. Dozono, N. Imai, K. Yoshida^a, Y. Yanagisawa^a, K. Kusaka^a, M. Ohtake^a, D. S. Ahn^a, O. Beliuskina, N. Fukuda^a, C. Iwamoto, S. Kawase^b, K. Kawata, N. Kitamura, S. Masuoka, H. Otsu^a, H. Sakurai^a, P. Schrock, T. Sumikama^a, H. Suzuki^a, M. Takaki, H. Takeda^a, R. Tsunoda, K. Wimmer^c, K. Yako, and S. Shimoura

Center for Nuclear Study, Graduate School of Science, the University of Tokyo

^a*RIKEN Nishina Center for Accelerator-Based Science*

^b*Department of Advanced Energy Engineering Science, Kyushu University*

^c*Department of Physics, the University of Tokyo*

The angle-tunable degrader system was developed for the OEDO beamline in RIBF [1], which produces a beam of 10 – 100 MeV/u using the slowing-down method in cooperation with BigRIPS [2]. This degrader system has been employed as a mono-energetic degrader to slow down a beam as well as to compress its energy spread. Since the wedge angle and thickness are adjustable, this system can deal with various experimental conditions. In this report, we present the structure and operation principle of the degrader system, together with the simulation studies and the experimental verification.

The angle tunability has been accomplished by a pair of aluminum sheets with quadratic cross section. Since their quadratic coefficients differ only in their signs, the overlap of the two sheets is effectively identical to the typical wedge degrader and the wedge angle can be changed according to the relative position of the sheets. Figure 1 shows the schematic views of this system and the angle-tuning mechanism. The thickness is also adjustable by introducing an additional flat plate with a proper thickness.

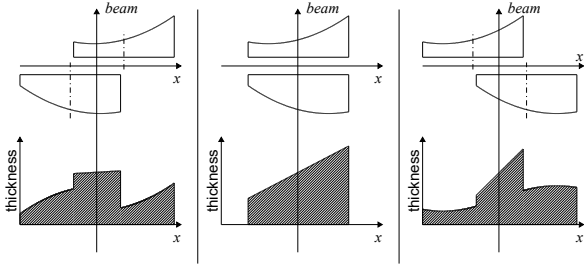


Figure 1. Schematic views of quadratic cross section of the aluminum sheets and the total thickness with the different relative positions.

The total system consists of the two aluminum sheets mentioned above, guides for those sheets mounted on two horizontal rails for parallel movement, and two vacuum motors separately connected to each degrader, as shown in Fig. 2. The curvatures of the aluminum sheets were successfully fabricated thanks to the high-precision machining. The system has the fixed center thickness of 3 mm and the wedge angle from 0 mrad to 40 mrad. The effective area is $\pm 30 \text{ mm(H)} \times \pm 50 \text{ mm(V)}$. The averages of thickness deviations from the machining precision for each aluminum sheet are 33 and 58 μm , respectively. Uncertainty of the

angle originated from these deviations is 2 mrad.

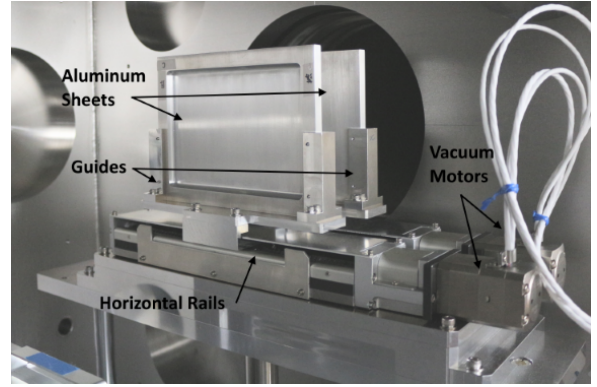


Figure 2. The angle-tunable degrader system installed on the OEDO beamline.

The range of application and performance of compressing energy spread of the system were estimated by Monte-Carlo simulation studies. In the simulation we considered the incident beam profile, the wedge angle and thickness of the degrader, and the energy-loss calculation with straggling. For the energy loss calculation ATIMA [3], the range calculation code developed at GSI, was employed.

The applicable limits according to the atomic numbers (Z) and the outgoing energy of RI beams (K_f) were evaluated by calculating an optimal angle and center thickness for different Z (fixed $K_f = 35 \text{ MeV/u}$) or K_f (fixed $Z = 34$). We assumed that the incident beams are parallel to the beam axis and have a perfect dispersion ($\delta \propto x$) of 5.36 mm/% in a kinetic energy deviation with the energy of 170 MeV/u. The dependency on Z provides another restriction for RI beams of $Z = 15 - 84$ with an energy of 170 MeV/u for $K_f = 35 \text{ MeV/u}$.

We evaluated the spread of K_f to estimate the performance of this system. The energy spread of an outgoing beam (σ_{out}) can be divided into the factors,

$$\sigma_{\text{out}}^2 = \sigma_{\text{in}}^2 + \sigma_{\text{str}}^2 + \sigma_{\text{irr}}^2, \quad (1)$$

where σ_{in} is originated by the energy-spread of the incident beam, σ_{str} is the straggling effect, and σ_{irr} is the uncertainty from the irregular thicknesses of the degraders. In this calculation, the experimental beam profile of 170 MeV/u with the energy deviation and dispersion are $\pm 1.3\%$ (in σ) and

5.36 mm/%, respectively, was employed. Each of the factors in Eq. (1) was deduced for the different Z or K_f applying the same criterion above for the optimized thickness and wedge angle. In most cases, σ_{irr} is largest, for example, $\sigma_{\text{irr}} = 3.4$ MeV/u for ^{79}Se with $K_f = 35$ MeV/u, which is larger than $\sigma_{\text{in}} = 2.8$ MeV/u and $\sigma_{\text{str}} = 0.7$ MeV/u. In particular, for high Z , σ_{irr} becomes dominant where the relative thickness deviation ($\Delta t/t$) is large due to a thin optimal thickness. Exceptionally, for low Z , a large optimal thickness, which means a small $\Delta t/t$, reduces σ_{irr} but increases σ_{str} .

The commissioning experiment of this degrader system was carried out at the OEDO beamline [1] in RIBF. A 345-MeV/u ^{238}U beam impinged on a 5 mm-thick Be target to produce a ^{79}Se beam of 171 MeV/u by the in-flight fission. ^{79}Se , separated by BigRIPS [2], were incident to the degrader system installed at FE9, the dispersive focus in the OEDO beamline. To slow down the beam to 40 MeV/u, the center thickness of the degrader system was set to be 6 mm. The experimental data was taken for the several wedge angles. We measured the TOF over the upstream and downstream of FE9 to reconstruct the incident and outgoing energies of the beams, respectively.

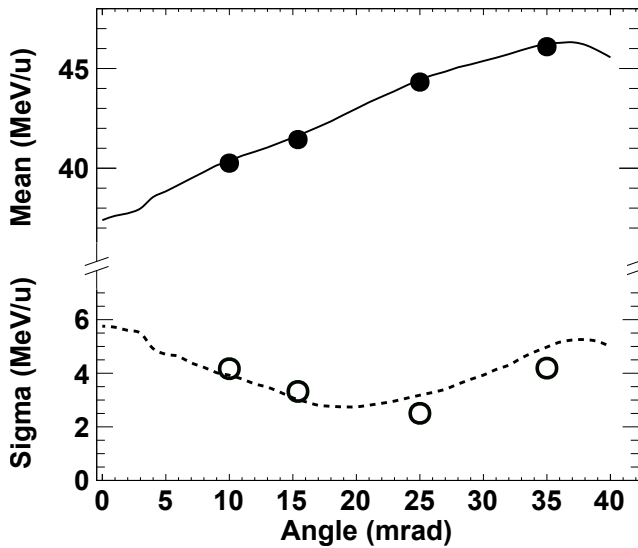


Figure 3. Means (solid) and sigmas (empty circles) of the K_f distributions deduced by fitting a Gaussian function for the different wedge angles with the simulation results (solid and dashed curves).

The wedge-angle dependences of the K_f distribution are shown in Fig. 3. The means and spreads (in σ) were deduced by fitting a Gaussian function. For the simulation the experimental beam profiles were employed. The experimental results are consistent with the simulative ones. While the center thickness of the system is invariable against the wedge angle, the mean value depends on it due to the misalignment of the beam to the degrader center. The spread is minimized at 20 mrad, where the dispersion of the beam is reduced most, and increases on both sides along with an enlarged dispersion.

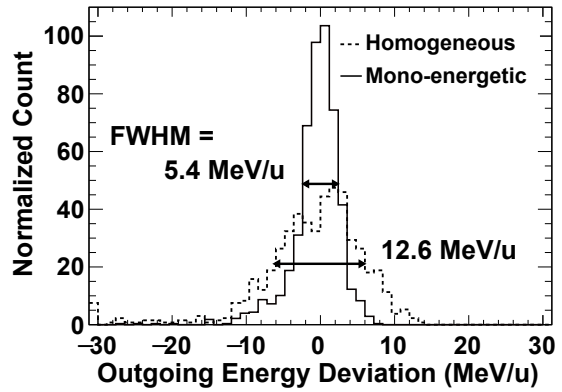


Figure 4. Distributions of the K_f deviation using a homogeneous degrader (dashed) and an optimized mono-energetic degrader (solid). All distributions were normalized to have the same number of events.

The quality of the outgoing beams in terms of an energy spread was evaluated by comparing the K_f deviations for two cases, using the optimized wedge angle for a mono-energetic beam and using the homogeneous degrader (0 mrad). As shown in Fig. 4, the energy spread in the case of the homogeneous degrader was measured to be 12.6 MeV/u in full width at half maximum (FWHM). In the case of the optimized mono-energetic degrader, the spread was reduced to 5.4 MeV/u, consistent with the estimated value by simulation, 5.2 MeV/u.

In summary, we have developed the angle-tunable degrader system as a mono-energetic degrader for the OEDO beamline for a low-energy RI beam. Its wedge angle can be adjusted by overlapping a pair of aluminum plates having quadratic cross section. The performance of the system was experimentally verified using ^{79}Se beam at 171 ± 2.7 MeV/u and we obtained the low-energy beam at 42 ± 2.7 MeV/u with the suppressed spread. The experimental results are consistent with the simulation results and the energy-compression performance was achieved, as successfully as estimated. The flexible wedge angle can provide high versatility to deal with a diverse nuclides and energies of RI beams for various purposes.

References

- [1] S. Michimasa, *et al.*, CNS Annual Report 2017, CNS-REP-97, 37 (2019).
- [2] T. Kubo, Nucl. Instrum. Methods Phys. Res. Sect. B **204**, 97 (2003).
- [3] The Energy Loss Code ATIMA, <https://web-docs.gsi.de/~weick/atima/>.

GEM-TPC Development Collaboration

- Construction and commissioning of a new active target CAT-M -

S. Ota^a, C. Iwamoto^a, R. Kojima^a, H. Tokieda^a, M. Dozono^a, S. Hayakawa^a, K. Kawata^a,
N. Kitamura^a, S. Masuoka^a, R. Tsunoda^a, S. Michimasa^a, T. Gunji^a, N. Imai^a, H. Yamaguchi^a,
Y. Mizoi^{a,b}, D. Suzuki^c, T. Isobe^c, J. Zenihiro^c, S. Nishimura^c, N. Zhang^d, K. Howard^e,
T. Harada^f, T. Murakami^g

^aCenter for Nuclear Study, Graduate School of Science, University of Tokyo

^bOsaka Electro-communication University

^cRIKEN Nishina Center

^dInstitute for Modern Physics of the Chinese Academy of Science

^eNotre Dame University

^fToho University

^gKyoto University

We are developing GEM-based time projection chambers (GEM-TPCs) under an inter-group collaboration in CNS, aiming at the measurement of nuclear reactions of short-lived nuclei at RIBF and the measurement of heavy ion collision at ALICE. In general, process of electron multiplication in GEM (and other so-called micro-pattern gas detectors) is quick relative to the multiplication process around wire. Thanks to the quick response, high-rate particle measurement can be realized. When the beam particles bombard an active area of GEM-TPC, nuclear reactions can occur in the active area. The TPC used in such an operation is called active target, which enables us to measure low-energy recoils and reaction vertex precisely. Within our collaboration, two active targets based on the GEM-TPC, called GEM-MSTPC and CAT-S [1] have been developed and used for the missing mass spectroscopy of short-lived nuclei at RIBF. By using CAT-S, the first forward-angle measurement of deuteron inelastic scattering off ¹³²Sn has been done in 2016, aiming at revealing isospin dependence of nuclear matter equation of state [2]. In the fiscal year of 2017, a new active target CAT-M was developed aiming at the measurements of giant resonances in A~100 unstable nuclei. In this report, the structure of CAT-M and its commissioning experiment are described.

The CAT-M is designed to have the thicker effective target and the larger acceptance than those of the CAT-M. The expected statistics will become 10 times larger with keeping the same resolutions for excitation energy and scattering angle in the center-of-mass frame. Figure 1 shows the picture of the CAT-M. The CAT-M consists of time projection chamber (TPC) and silicon detectors.

The field cage of the TPC is of cubic shape and the volume of the field is of dimension of 400-mm in width and depth and 200-mm in height with two layers of 4-mm pitch wires. Each wire in one layer is connected with 1-MΩ resistor. The wire diameter is 50 μm. The uniform drift field is formed in an active area of 304 × 280 defined by the aperture of anode plate of the field cage. A mesh grid is glued on the anode to maintain the uniform drift field. The wire diameter and the aperture of the mesh grid are 30 μm and 224 μm, respectively. The field cage is placed on the bottom plate of the chamber. A dual-gain multi-layer thick gas

electron multiplier (DG-M-THGEM) is designed by ourselves and produced by REPIC, based on the design of M-THGEM [3]. The DG-M-THGEM has four electrode layers and three insulator layers, which are placed alternately. Total thickness of DG-M-THGEM is about 1.3 mm. The hole size and pitch is 300 μm and 700 μm, respectively. Specification of the DG-M-THGEM is summarized in Table 1. The performance evaluation of a prototype DG-M-THGEM is summarized in Ref. [4]. Three electrode layers are three-fold segmented along the beam axis, in order to control the gains at beam (center) and recoil (side) regions, independently. The multiplied electrons are collected in readout pads. Each readout pad is of regular triangle shape with 7-mm side. The total number of readout pads is 4048.



Figure 1. A photograph of CAT-M, which consists of TPC and silicon detectors. The size of active volume is 310×280×200 mm³.

Table 1. Specification of DG-M-THGEM

Dimension	300 × 360 × 1.3 mm ³
Electrode	15-μ Au coated 18-μ Cu
Insulator	FR4 (400, 380, and 400 μm)
Hole	300 μm in diameter with 700 μm pitch
Beam region	29.4 × 308 mm
Recoil region	132.5 × 308 mm

Two arrays of silicon detectors are placed on the both sides of the TPC. Each array consists of six single sided strip silicon detectors with 10 × 10-cm² area and about 500-

μm thickness (products of Hamamatsu). The signals from the strips are read out.

The same readout scheme is used both for the TPC and the silicon detector arrays. The signal is transferred by using flexible printed circuit (FPC) cable with 67 lines. The 32 lines are used for signal and the rest are connected to ground. At the border of chamber, a printed circuit board (PCB) with FPC connectors at the both sides used as feedthrough in order to seal the gas. The signals are processed and acquired by using general electronics for TPC's (GET) consisting of AsAd, COBO and Mutant. The transferred charge is read by a digitization board with programmable pre-amplifier and shaping amplifier called AsAd through protection circuit board called ZAP. In our ZAP board diodes are mounted to protect the pre-amplifier from unexpected large amount of charges. The AsAd board has a function to produce the multiplicity signal of hits. One AsAd board can treat 256 signals and four AsAd boards can be connected to one COBO. The COBO collect the multiplicity signal from the AsAd board and produce the trigger output to be used as the external trigger. The COBO accepts the external trigger and distributes it to the AsAd boards, then the AsAd board buffers the digitized samples and sends them to the COBO. The data is read out directly from each COBO via 10-Gbps optical link connected to a data storage server. The Mutant synthesizes the clocks among the COBO's and the AsAd's, while the Mutant has other intelligent functions such as the multiplicity assembling, high-level trigger production and so on. The whole system of GET is managed by using a software Narval.

The CAT-M was constructed and commissioned in December, 2017. The commissioning was performed at HIMAC under the experiment program 15H307. The CAT-M was operated with 0.3-atm hydrogen to measure the proton inelastic scattering off ^{136}Xe . The bias voltage values for the cathode and the anode of the field cage were -9 kV and -6 kV to form the drift field having the strength of 1 kV/cm/atm, with which the drift velocity was about 1 cm/ μs . The typical bias voltages for the electrodes of the DG-TH-GEM are -1600 V, -1120 V, -640 V, -160 V for the recoil region and are -1600 V, -1146 V, -815 V, -361 V for beam region. The ^{136}Xe beam accelerated by a synchrotron up to 200 MeV/u bombarded the CAT-M. The typical intensity was 10^6 particles per pulse (ppp) with typical extraction time of 1.2 sec. The thresholds to produce the trigger from the hits in readout pad of the TPC should be high enough to discriminate the delta rays. However, these threshold values are commonly used to determine if the hits are recorded or not. If the thresholds for all the readout pads are high, the singles from the high energy recoils reaching at silicon detectors cannot be recorded. In order to overcome this problem, we decided to divide the recoil region into two region. In one region the threshold value is high enough to create the trigger for the events where the recoil particles stops inside the active area in TPC, namely, around the beam trajectory, and in the other regions the threshold values are as low as possible to record all the pulses. The external trigger was the logical OR of the hit signals of readout pads in TPC

and ones of the silicon detectors.

The CAT-M worked with 10^6 -ppp beam injection during about 20-hours measurement. The recoil events were successfully recorded with the TPC triggers. Typical hit pattern in the TPC is displayed in Fig. 2. Beam particles traveled from bottom to top and a particle was recoiled at around $Z = 20$ mm horizontally. But the number of silicon triggers was larger than expected and thus the external trigger was produced by using only TPC triggers. One possible reason for the background in the silicon trigger is light particle production at the transportation of beam and it strongly depends on the experimental condition. We will find the source of the background in the next experiment in HIMAC. Analysis for the performance evaluation is ongoing.

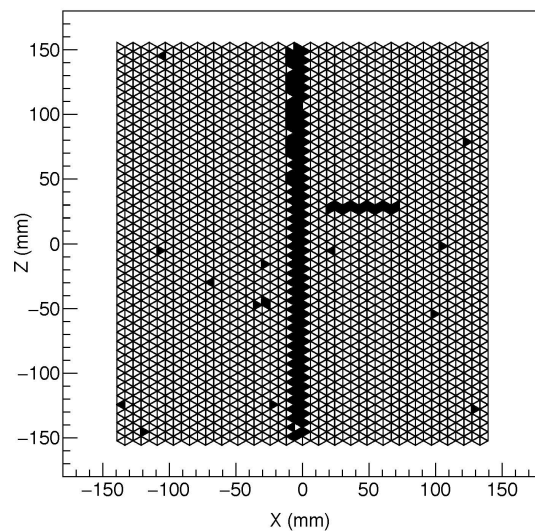


Figure 2. Hit pattern for one event triggered by TPC.

References

- [1] S. Ota *et al.*, J. of Radioanal. Nucl. Chem. 305, 907 (2015).
- [2] S. Ota *et al.*, CNS Annual Report 2016, CNS-REP-96, 49, 2018
- [3] M. Cortesi *et al.*, Rev. of Sc. Instrum. 88, 013303 (2017).
- [4] C. Iwamoto *et al.*, CNS Annual Report 2017, CNS-REP-97, 17, 2019

The Linear Polarization Sensitivity of CNS-GRAPE detector

T.T. Pham, E. Ideguchi^a, N. Aoi^a, S. Miyamoto^b, M.R. Kumar^a, T. Vijiamaa^{a,c}, H.T. Hoang^a,
A. Kohda^a, T. Shima^a, T. Shizuma^c, Y. Yamamoto^a, K. Sugita^d,

^aResearch Center for Nuclear Physics, Osaka University

^bUniversity of Hyogo

^cUniversity of Jyvaskyla

^dNational Institute for Quantum and Radiological Science and Technology

Linear polarization of γ -ray emitted from excited nuclei is one of important information which in addition to angular distribution or correlation, can be used to assign the nuclear state parities and the electric -magnetic characteristic of the γ transition. Standard method to deduced the linear polarization is evaluating the Compton scattering angular distribution of γ -ray. These information can be achieved by taking the coincidence between signal from the detector/segment that get hit from the original photon and the one that get hit from the scattered photon. The asymmetry of scattering angle will show the polarity of γ -ray. The CNS GRAPE segmented detector as a Compton polarimeter allows to measure the polarity. The application of such polarimeters in multidetector arrays gives opportunity to obtain the complete and comprehensive spectroscopic information even in a case of complex spectra or weak transitions. [1].

To determine the polarization sensitivity (Q) one should use the polarized γ -rays with well known linear polarization (P). In the experiment one measures an asymmetry of Compton scattered photons

$$A = \frac{N_{\perp} - N_{\parallel}}{N_{\perp} + N_{\parallel}}$$

where: N_{\perp} , N_{\parallel} -number of coincidence counts in perpendicular and parallel (to the reaction plane) segments detector, respectively. The polarization sensitivity is defined as:

$$Q = \frac{A}{P}$$

The aim of the experiment was evaluating the linear polarization sensitivity of CNS-GRAPE (Gamma-Ray detector Array with Position and Energy sensitivity) using polarized laser-compton scattering γ -ray in NewSUBARU storage ring. GRAPE is an integrated detector with 2 coaxial HPGe crystals 60 mm diameter x 20 mm thick which divided into 9 electrical segments. The 3.8 MeV gamma beam was irradiated to central segment. The beam polarization was set to horizontal and vertical direction respectively. The data acquisition system define an "event" as a set of energy deposited value corresponding to each segment with a common time stamp. Because the rate is relatively low, it is able to assume that all sub-events are time-coincident. Events that reflect the polarization of the primary gamma photon and thus show the polarization sensitivity of the detector is the one interacts with central segment via a single Compton scattering and then completely absorbed by a vertical or horizontal segment. Such event should satisfy the

energy conditions: total energy deposited in these two segments is equal to the original gamma energy and the energy deposited in the central segment stays in the range limited by the scattering angle. The limitation angle depend on the size of detector segments (as demonstrated in Figure 1).

The experiment was run for 2 hours totally with horizontal and vertical polarization respectively. The asymmetry deduced is $A = 0.022 \pm 0.018$.

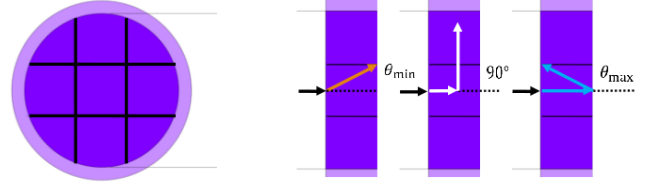


Figure 1. Left: front view of GRAPE crystal. Right: side view of GRAPE crystal and demonstration of scattering angle limitation.

The experimental result is compared with simulation using Geant4 toolkit. The geometry is simplification as crys-

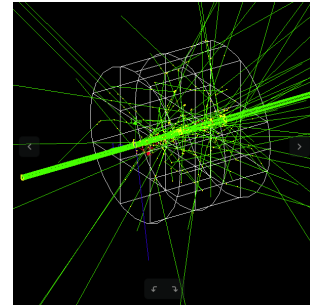


Figure 2. Gamma trajectory simulation.

tal volume only. This simplization has slightly effect the efficiency of the detector at low and intermediate energy. To reproduce energy spectrum, the beam original energy which is not simple monochromatic value, should be generated correctly. The gamma source used is quasi-monochromatic beam generated by Compton scattering from high energy electron collision with laser photon. Gamma energy depend on electron energy, laser wavelength and scattering angle. [2]

$$E_{\gamma} = \frac{4\eta^2 \epsilon_L}{1 + (\eta\theta)^2 + 4\eta\epsilon_L/m_e c^2}$$

where:

E_γ is energy of scattered gamma ray

ϵ_L is energy of laser photon

E_e is electron energy

θ is scattering angle of laser photon with respect to electron incident direction

$m_e c^2$ is rest mass of electron

$\eta = E_e / m_e c^2$

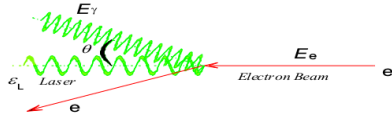


Figure 3. Laser-electron Compton back scattering.

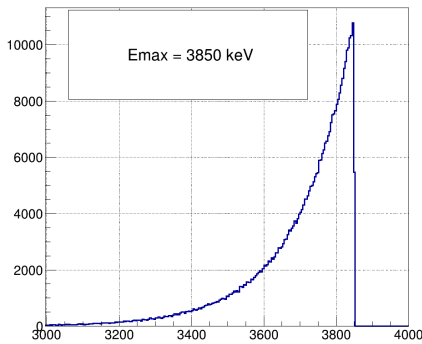


Figure 4. Simulated primary gamma energy distribution.

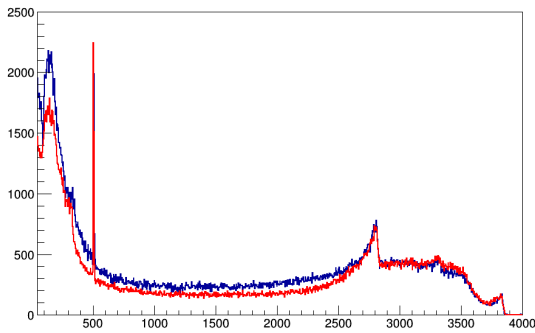


Figure 5. Experiment in comparison with simulation. The blue line is sum spectrum with background subtraction. The red line is simulated spectrum

Simulated photon energy with intensity exponentially decreasing from the maximum energy.

$$p(E) = ae^{-a(E_{max}-E)}$$

where a is a constant and adjusted to fit with full energy peak shape experimental spectrum. The simulation give the best fit with experiment with the number of incident events higher by approximately 5% than in experiment

References

- [1] K. Starosta, Ch. Droste, G. Hagemann, B. Herskind, T. Morek, P. Napiorkowski, G. Sletten and J. Srebrny, Polarization Sensitivity of CLOVER detector
- [2] H. Utsunomiya, S. Hashimoto, S. Miyamoto, The γ -ray beamline in NewSUBARU, *Nuclear Physics News* Vol. 25, No. 3, 2015
- [3] www.lasti.u-hyogo.ac.jp/NS-en/newsubaru

Development of a high density ${}^7\text{Be}$ beam at CRIB

A. Inoue, A. Tamii, H. Yamaguchi^a, K. Abe^a, A. Adachi, S. Hayakawa^a, J. Isaak, N. Kobayashi, H. Shimizu^a, and L. Yang^a

Research Center for Nuclear Physics, Osaka University

^a*Center for Nuclear Study, Graduate School of Science, University of Tokyo*

The ${}^7\text{Li}$ problem is a discrepancy between the standard Big-Bang Nucleosynthesis (BBN) model and observations. Our research goal is to measure the cross section of the ${}^7\text{Be}(d, p)$ reaction to solve this ${}^7\text{Li}$ problem. A recent theoretical BBN model predicts a primordial ${}^7\text{Li}$ abundance that is 3 times larger than the recent precise observation [1]. This difference is quite large, while the theoretical calculation reproduces the abundance of the other light nuclei well. One possible scenario to solve the problem, which has not been included yet in the BBN model, is that ${}^7\text{Be}$ was destroyed in the nuclear reaction after the Big Bang. The ${}^7\text{Be}(d, p){}^8\text{Be}$ and the ${}^7\text{Be}(n, \alpha){}^4\text{He}$ [2] reactions are two promising processes for destroying ${}^7\text{Be}$. We are focusing on the ${}^7\text{Be}(d, p){}^8\text{Be}$ reaction since the contribution from ${}^7\text{Be}(d, p){}^8\text{Be}$ is suggested to be larger than that from ${}^7\text{Be}(n, \alpha){}^4\text{He}$ [3].

We are developing an unstable ${}^7\text{Be}$ target for high-resolution measurement of the ${}^7\text{Be}(d, p){}^8\text{Be}$ reaction in normal kinematics. This is a big technical challenge since ${}^7\text{Be}$ is an unstable nucleus. We suggested to make the ${}^7\text{Be}$ target by implantation in a host material. This is called the *Implantation method*. The development is ongoing at CRIB, Center for Nuclear Study (CNS), University of Tokyo. The first experiment was performed in June 2016. The primary beam was ${}^7\text{Li}^{2+}$ at 5.6 MeV/nucleon. The secondary beam was produced by the ${}^1\text{H}({}^7\text{Li}, {}^7\text{Be})$ reaction by employing a cryogenic hydrogen gas target. The gas thickness is 8 cm and the gas pressure was 760 Torr. The secondary beam energy was 4.0 MeV/nucleon. A 10- μm thick gold foil as a host target was irradiated with the ${}^7\text{Be}$ beam after an energy degrader made of gold with a thickness of 15 μm and a collimator with a diameter of 3 mm. We evaluated the amount of the implanted ${}^7\text{Be}$ by detecting 477 keV γ rays with a LaBr_3 detector after the implantation. The γ ray is emitted through the electron capture decay of ${}^7\text{Be}$ with a branching ratio of 10.4%. We obtained 1.3×10^{11} ($4.3 \times 10^{10} / \text{mm}^2$) ${}^7\text{Be}$ particles after 19 hours of irradiation. The average beam intensity was $6.3 \times 10^5 / \text{mm}^2$. However, the number of the ${}^7\text{Be}$ particles is almost 10 times smaller than our estimation from the maximum intensity ($\sim 10^6 / \text{mm}^2$) of CRIB's previous performance. We suspect that the beam spot size and the beam profile at F2 were not fully optimized for the high-intensity ${}^7\text{Be}$ beam downstream of the collimator and not maintained at a fixed position during the long irradiation time since we did not check the ${}^7\text{Be}$ beam profile when the beam intensity was increased. This is because it was not possible to count such a high intensity beam directly.

Based on the result of the experiment in 2016, we per-

formed a development experiment at CRIB to optimize the beam line optics and obtain an intense beam of ${}^7\text{Be}$, in April 2017. Previously, the beam profile was checked with the PPAC detector at CRIB. However the PPAC detector is not a detector for such a high rate, so we could not count the high intensity beam with the existing detector. To solve this issue, we installed a metal mesh at F1 and a plastic scintillator at F2 to count the beam intensity. This was a new trial at CRIB. The metal mesh was used to reduce the ${}^7\text{Be}$ beam intensity, and hence we could count the ${}^7\text{Be}$ beam intensity directly by the plastic scintillator. In this experiment, we tuned the ion-optical parameters and the steerer on the beam line for the best-positioning and focusing of the secondary ${}^7\text{Be}$, by counting the intensity with the plastic scintillator. We achieved $6.8 \times 10^6 / \text{mm}^2$ as the average beam intensity after the optimization of the settings of beam-line optics. We obtained 1.2×10^{12} ($1.7 \times 10^{11} / \text{mm}^2$) ${}^7\text{Be}$ particles with 7-hours irradiation as expected. As the next step, we plan to measure the ${}^7\text{Be}(d, p)$ reaction at Japan Atomic Energy Agency, tandem facility. The ${}^7\text{Be}$ target will be produced at CRIB before the (d, p) reaction measurement, planned for 2018. About 8.2×10^{12} ($2.6 \times 10^{12} / \text{mm}^2$) ${}^7\text{Be}$ ions will be implanted in 2 days of irradiation.

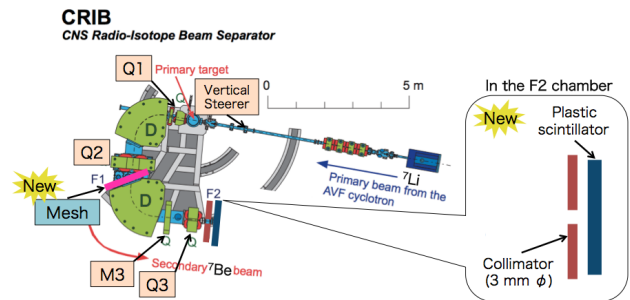


Figure 1. Plane view of CRIB, where the Q1, Q2, Q3, and M3 magnets and the steerer were optimized in the present work. The installation of the mesh at F1 and the plastic scintillator at F2 was a new trial at CRIB to count the high intensity beam. The ${}^7\text{Be}$ beam was counted after the 3 mm diameter collimator.

References

- [1] R.H. Cyburt *et al.*, *J. Cosmol. Astropart. Phys.* **11**, 012 (2008).
- [2] T. Kawabata *et al.*, *Phys. Rev. Lett.* **118**, 052701 (2017).
- [3] S.Q. Hou *et al.*, *Phys. Rev. C* **91**, 055802 (2015).

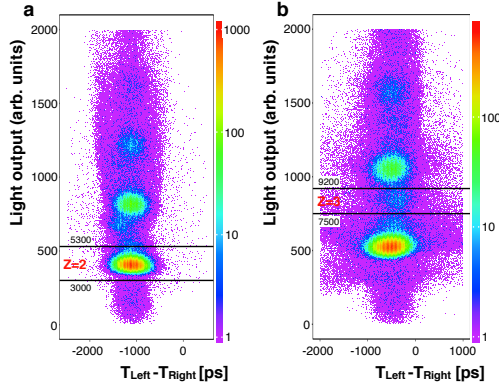


Figure 2. An incoming (a) and outgoing (b) PID spectrum of the SBT and HOD 0 detectors. The $Z=2$ and $Z=3$ gates provided the clear tagging of the ${}^6\text{He}(p,n){}^6\text{Li}$ reaction events.

local triggering option of the two-two coupled channels, in V1730 two neighboring channels are paired, was used to ensure the coincidence between the top and bottom PMTs of PANDORA. The digitizers were configured so that the validation of the local triggers came from an external trigger based on the programmed software criteria. In order to manage the coincidence requirements between the SBT start counter, hodoscopes and PANDORA, the first channel of each digitizer was dedicated to a logic signal coming from the coincidence of the start counter and hodoscope detectors (analog DAQ branch). This external trigger was validating the PANDORA self-triggers in a 500-ns wide time window.

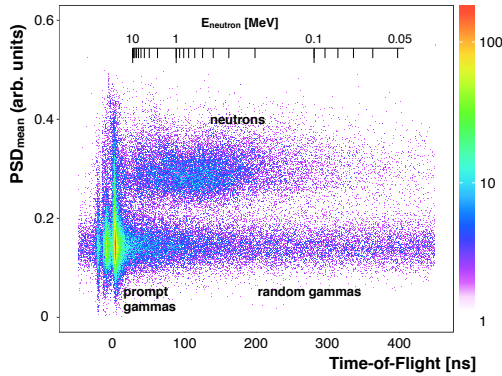


Figure 3. The PSD_{mean} vs. ToF spectrum of PANDORA shows the importance of separating neutrons and random gamma background. Inset scale corresponds to the kinetic energy of the detected neutrons obtained by the ToF method.

The neutron-gamma discrimination (PSD parameter) of PANDORA is based on comparison of integrated charges measured over two different time regions of the input signal:

$$\text{PSD} = \frac{Q_{\text{Long}} - Q_{\text{Short}}}{Q_{\text{Long}}}, \quad (1)$$

where Q_{Long} and Q_{Short} are the charges integrated in long and short gates, respectively. The arithmetic mean of PSD values of two single-end readouts of each PANDORA bar ($\text{PSD}_{\text{bottom}}$ and PSD_{top}) was defined as, PSD_{mean} [9]. The

combination of the measured neutron ToF with the new PSD parameter improved the discrimination of neutron- and gamma-like events originating from the (p,n) reaction on ${}^6\text{He}$. Figure 3 shows the PSD_{mean} plotted against the neutron ToF. The large random gamma background, originating from the environment, in the ToF range of neutrons could not be removed without the PSD information. By using the DDAQ, we were able to detect neutrons having kinetic energies lower than 100 keV.

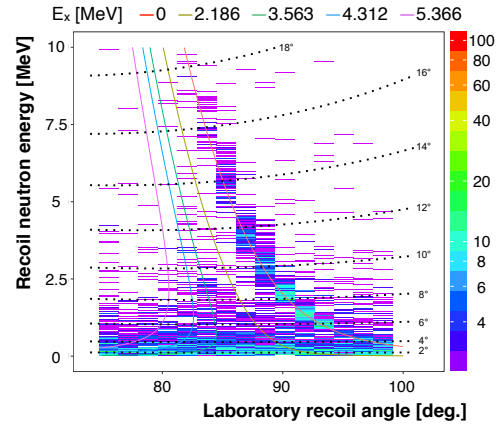


Figure 4. Correlations between recoil neutron energy and laboratory kinematics for fixed excitation energies. Each vertical bar (a unit in horizontal axis) represents a PANDORA bar.

Selecting the incident ${}^6\text{He}$ particles and requiring the identification of ${}^6\text{Li}$ reaction residues produced from the (p,n) reaction and gating on neutron-like events by PSD_{mean} , a clear kinematical correlation can be seen in Fig. 4. This matches with the calculated kinematical correlations for the ${}^6\text{He}(p,n)$ charge-exchange reaction at 123 MeV/u energy and corresponds to transitions to the ground state in ${}^6\text{Li}$, and demonstrates effectiveness of PANDORA and its PSD capability.

In summary, PANDORA was successfully commissioned in the ${}^6\text{He}(p,n){}^6\text{Li}$ measurement.

References

- [1] K. Yako, et al., RIKEN Accel. Prog. Rep. 45 (2012) V.
- [2] L. Stuhl, et al., RIKEN Accel. Prog. Rep. 48 (2015) 54.
- [3] K. Nakayama, et al., Phys. Lett. B 114 (1982) 217.
- [4] T.N. Taddeucci, et al., Nucl. Phys. A 469 (1987) 125.
- [5] M. Sasano, et al., Phys. Rev. Lett. 107 (2011) 202501.
- [6] M. Sasano, et al., Phys. Rev. C 86 (2012) 034324.
- [7] K. Yako, et al., RIKEN Accel. Prog. R. 45 (2012) 137.
- [8] J. Yasuda, et al., Phys. Rev. Lett. 121 (2018) 132501.
- [9] L. Stuhl, et al., Nucl. Instrum. Meth. A 866 (2017) 164.
- [10] L. Stuhl, et al., Proceedings of Sci. (INPC2016) 085.
- [11] N. Zaitseva, et al., Nucl. Instr. Meth. A 668 (2012) 88.

Energy measurements with single crystal diamond detector at HIMAC

O. Beliuskina^a, N. Imai^a, S. Michimasa^a, N. Kitamura^a, M. Dozono^a, C. Iwamoto^a, K. Kawata^a, S. Masuoka^a, S. Ota^a, H. Sakai^b, E. Takada^c, R. Tsunoda^a, K. Yako^a

^aCenter for Nuclear Study, Graduate School of Science, University of Tokyo

^eRIKEN Nishina Center

^dNational Institute of Radiological Sciences

Many works performed in the last decades demonstrated that the diamond offers new possibilities for fast, radiation hard detection devices for charged particles [1–6]. The latest generations of diamond particle detectors are made using the high-purity single-crystals (SCDD), which produced by chemical vapour deposition method (CVD). An attractive advantage of SCDDs is in the possibility to measure time and energy signals simultaneously with an excellent resolution [3–5].

The experiment was carried out at the Heavy Ion Medical Accelerator in Chiba (HIMAC) at the National Institute of Radiological Sciences (NIRS), Japan. ¹³⁶Xe primary beam with energy 200 MeV/u passed through an active target [7] and different detectors including the polycrystalline CVD diamond strip detector before they hit a SCDD installed at angle of 0° in respect to the beam direction. It has to be mentioned that all detectors were placed in the air.

For the energy measurements the single-crystal CVD diamond detector with thickness of 140 μm manufactured by CIVIDEC [8] was used. It has the pad type gold electrodes of 4 × 4 mm² area with one readout. The electrical field applied to SCDD was 2 V/μm.

In this experiment we used the charge sensitive preamplifier CIVIDEC C6. The expected energy deposit of a Xe beam was higher than PA working range. Because of it we used -40 dB attenuator CIVIDEC D4. To avoid the damage on the attenuator the high voltage was applied to SCDD via the AC-DC splitter. The AC-DC splitter is a device to decouple the AC part from the DC part of the detector signal. To obtain a better energy resolution we analyzed the pulse area instead of the pulse height. For this we used a charge-to-time converter with a leading edge discriminator (CTC) manufactured by Fuji Diamond [9]) and a time-to-digital-converter Caen V1290 (TDC). Additionally we have taken a few runs for SCDD without the PA where instead of it we used the AC-DC splitter only.

Energy losses in SCDD estimated to be 640 MeV for ¹³⁶Xe beam. To determine the energy resolution of SCDD we performed the linearity check of the measuring system with a pulse generator (model 417 NIM). In prior to these experiments we performed the energy calibration of SCDD with the mixed α-source. The obtained value of the detector energy resolution including the contribution from the readout electronics was 25 keV for 5.5 MeV alphas of ²⁴¹Am.

In this experiment the ¹³⁶Xe beam with the energy of 170 MeV/u passed through SCDD. Because the maximum charge accepted by the C6 is 180 fC we attenuated the signal by 100 times. The energy spectrum of the ¹³⁶Xe measured by SCDD is presented in Figure 1. The obtained en-

ergy resolution, $\Delta E/E$, was about 1%. This value contains following uncertainties: the beam straggling in the air, the multiple scattering along all setup parts, the detector thickness ambiguity and effects in readout electronics.

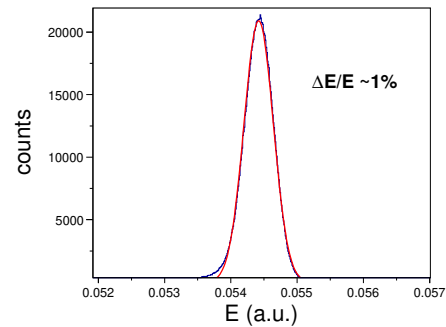


Figure 1. The energy spectrum of the ¹³⁶Xe obtained by SCDD.

As mentioned above, additionally we measured a few runs for SCDD without the PA where instead of it we used the AC-DC splitter only. First we checked the signals with a 500 MHz digital storage oscilloscope. The observed pulse height and length were about 150 mV and 12 ns and 250 mV and 8 ns at the electric field of 1 and 2 V/μm, respectively. The energy resolution, $\Delta E/E$, was about 4.5%.

References

- [1] Kozlov S. F., Stuck R., Hage-ali M. and Siffert P., IEEE Trans. Nucl. Sci., NS-22 (1975) 160.
- [2] Knoll G. F., Radiation Detection and Measurement, 3rd edition (Wiley, New York, USA) 2000, pp. 357, 389–391.
- [3] C. Bauer *et al.*, Nucl. Instr. and Meth., **383** (1996) 64.
- [4] M. Pomorski *et al.*, Phys. Stat. Sol. (a) **202** 11 (2005) 2199.
- [5] M. Pomorski *et al.*, Phys. Stat. Sol. (a) **203** (2006) 3152.
- [6] S. Michimasa *et al.*, Nucl. Instr. Meth. **B42** (2013) 710.
- [7] S. Ota, H. Tokieda, C. S. Lee, Y. N. Watanabe, J. Radioanal. Nucl. Chem. **305** (2015) 907.
- [8] CIVIDEC Instrumentation, <https://cividec.at>
- [9] T. Ishikawa *et al.*, Nucl. Instr. Meth. **A875** (2017) 193.

Upgrade of the beam-orbit analysis method of RIKEN AVF Cyclotron injection line by four-dimensional emittance

Y. Kotaka, Y. Ohshiro, H. Yamaguchi, N. Imai, Y. Sakemi, T. Nagatomo^a
 J. Ohnishi^a, A. Goto^a, M. Kase^a, K. Hatanaka^b, H. Muto^c and S. Shimoura
 Center for Nuclear Study, Graduate School of Sciences, University of Tokyo

^aRiken Nishina Center

^bResearch Center for Nuclear Physics, Osaka University

^cCenter of General Education, Tokyo University of Science, Suwa

1. Introduction

For the purpose of increasing the beam intensity of AVF cyclotron, we focused on the improvement of the injection beam intensity. Therefore we started to optimize the injection beam transport system. As a first step of the optimization, we have developed a calculation method of the beam-orbit down to the center of the AVF cyclotron from the ion source by using the 4D emittance measured with a pepper-pot emittance monitor[1] (PEM_IH10), as shown in Fig. 1.

2. Multistep ellipse model for space charge effect

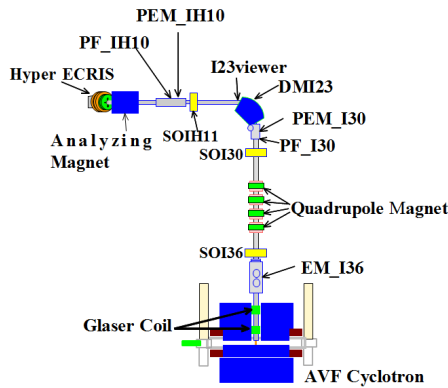


Figure 1. Beam injection line of AVF cyclotron

In order to improve the calculation of the space charge effect, we formulated a multistep-ellipse model instead of a single-ellipse model. In the single-ellipse model, the shape and beam intensity distribution of the beam cross section are approximated by an ellipse and by a uniform distribution, respectively. However, the real beam intensity distribution is not uniform [2]. Therefore, we presume a number of concentric ellipses and give each ellipse different amount of beam elements to simulate the real intensity distribution.

To construct the equation of motion (EOM) [3], a standard ellipse must be defined by the combination of the average, standard deviation and correlation of the

beam intensity distribution. This time, multistep ellipses are made by evenly dividing the ellipse, the radius of which is 6 times larger than the radius of the standard ellipse, into 30 ellipses.

First, the EOM including the space charge effect for the beam element in the innermost ellipse is constructed. Then, the EOM for the beam element located between the second and first innermost ellipse is constructed from the second ellipse. For the outer ellipses, the EOM is constructed accordingly. The beam elements beyond the outermost ellipse are neglected.

An example of calculated beam distribution by the multistep-ellipse model is shown in Fig. 2. Ion beam measured is ${}^4\text{He}^{2+}$ 15.4 keV of 250 μA . The left of Fig. 2 shows a beam intensity distribution measured by I23viewer shown in Fig. 1, which is a beam viewer. The middle of Fig. 2 shows a beam intensity distribution calculated using the single-ellipse model. The radius of the single ellipse is 1.8 times larger than the radius of the standard ellipse. The right of Fig. 2 shows a beam intensity distribution calculated using the multistep-ellipse model. It can be seen that the multistep-ellipse model reproduces the measured distribution better than the single-ellipse model.[4]

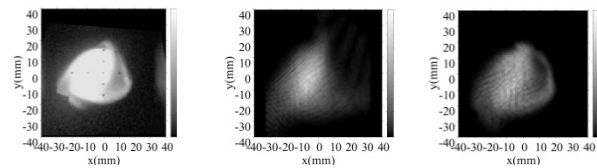


Figure 2. (Left) beam intensity distribution measured with I23viewer. (Middle) beam intensity distribution calculated by the single-ellipse model. (Right) beam intensity distribution calculated by the multistep-ellipse model. Ion beam is: ${}^4\text{He}^{2+}$ 15.4 keV of 250 μA .

3. Evaluation of the beam-orbit calculation

In order to evaluate the comparison between the measurements and the beam-orbit calculation, χ^2 test is introduced. The existing measurements are composed of I23viewer, beam profile monitor (BPM) and 2D emittance monitor (EM_I36). The coordinate system of

EM_I36 is (u, w) perpendicular to beam direction. I23viewer and EM_I36 are 2D distribution, so that χ^2 test should be done with 2D distribution. However, some 2D distributions obtained from the beam-orbit calculation become uneven because the 4D emittance is measured at 3 mm intervals. In such a case, χ^2 becomes so large that a fair comparison is difficult. Therefore, we adopted the comparison with two 1D distributions which are the two projections made from 2D distribution. This way is preferable to prevent the distribution from being uneven.

An example of the comparison with 1D distribution is shown in Fig. 3. The solid line and dashed line show the measured and the calculated distributions, respectively. The areas of both distributions are normalized to 1. By the way, the dispersion of χ^2 test is arbitrary this time because the accuracy of the beam-orbit calculation is rough, so that χ^2 is too large if a proper dispersion is used. Therefore, we suppose the dispersion is 10% of the highest value of the calculated distribution. For example, the χ^2 divided by degree of freedom (χ^2/DOF) of Fig. 3 is 1.0 by using the dispersion.

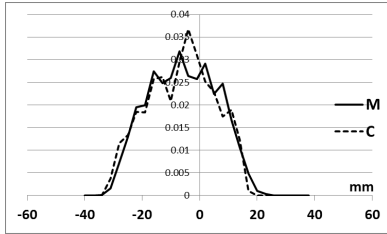


Figure 3. An example of the comparison. The solid line shows measurement and the dashed line shows the beam-orbit calculation. In this example, χ^2/DOF is 1.0.

Using this χ^2 test, we try to evaluate our beam-orbit calculation by comparing with the measured 2D emittances, u-u' and w-w' of EM_I36. The beams used for measurement are shown in Table 1. The left of Fig. 4 indicates the scatter plot of χ^2/DOFs of u and u'. The horizontal axis is u (position projection of u-u') and the vertical axis is u' (angle projection of u-u'). In the same way, the χ^2/DOFs of w-w' are indicated in the right of Fig. 4. All the χ^2/DOF is found to be less than 6. Though the absolute values of χ^2/DOF mean little, our beam-orbit calculation may be judged to be somewhat useful in reference to Fig. 3. The ambiguity of dispersion of χ^2 test should be improved in future.

Table 1. Measured beams used for χ^2 test

Ion	Energy(keV)	Intensity(μA)	DMI23(A)
H ⁺	12.6	220	12
² H ⁺	12.6	335, 360	25
⁴ He ²⁺	13.8	18, 32, 110	18
⁴ He ²⁺	15.4	250, 250, 270	19
⁴ He ²⁺	25.4	5, 10	25
⁷ Li ²⁺	22.3	69	30
¹¹ B ⁴⁺	22.8	17, 27	27
¹⁸ O ⁶⁺	17.6	57	25

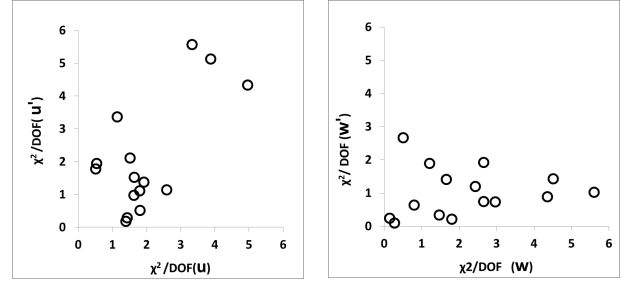


Figure 4. (left) Scatter plot shows χ^2/DOFs of u and u'. (right) Scatter plot shows χ^2/DOFs of w and w'.

4. Difference of the position and angle of beam

By the development of beam-orbit calculation, each shape of position or angle distributions is close to the measurement. But, each center position or each center angle is still different between the measurement and the calculation. From the result of 15 kinds of beams as previously mentioned, the differences of each center position are found to be about 10 mm and the differences of each center angle are found to be about 10 mrad at EM_I36. Such differences are not negligible because the minimum radius of beam pipes is 55 mm and the aperture of the spiral inflector at the entrance of AVF cyclotron is about 8 mm. Two reasons are considered about such differences. The first reason is incomplete alignments of PEM_IH10. As PEM_IH10 still has been aligned with only one BPM, we need to improve the alignment with two BPMs. The second reason is the difference caused by the magnetic hysteresis of the dipole magnet (DMI23 shown in Fig. 1).

We examined field hysteresis of DMI23 and found out it is at most 1.7%, which is caused as the excitation current is within the range from 10A to 20A. This is also not negligible. This region of excitation current is often used, shown in table 1. For example, the 1.0% magnetic field difference means leads to a position difference of 10 mm at 300 mm from the exit of DMI23 when the magnetic rigidity of beam is 0.023 Tm. To solve it, we will measure the magnet field of DMI23 at the time of measurement of PEM_IH10. In the future, the differences of position and angle should be solved. Then we suppose that the development of the calculation method of beam-orbit will be completed.

References

- [1] T.Hoffmann et al., Proc. 9th BIW 2000, Cambridge, USA, PP.432-439.
- [2] Y.Kotaka et al., CNS Ann. Rep. 2016 (2018) 57.
- [3] S. Y. Lee: *Accelerator Physics 1st ed.* (Singapore, World Scientific, 1999)
- [4] Y. Kotaka et al., Proc. 14th Annual Meeting of PASJ, Sapporo (2017), pp. 1118-1122.

Production of $^{56}\text{Fe}^{15+}$ ion beam by cylindrical material in Hyper ECR ion source

Y. Ohshiro, Y. Kotaka, H. Muto^a, H. Yamaguchi, N. Imai, Y. Sakemi and S. Shimoura

Center for Nuclear Study, Graduate School of Sciences, University of Tokyo

^aSchool of General and Management Studies, Suwa University of Science

1. Introduction

The Hyper ECR ion source injected various kinds of ion beams from gas and metal into the RIKEN AVF cyclotron [1,2,3]. This year, the beams such as $^2\text{H}^+$, $^4\text{He}^{2+}$, $^7\text{Li}^{2+}$, $^{12}\text{C}^{4+}$, $^{56}\text{Fe}^{15+}$ were extracted from the cyclotron. In particular, $^4\text{He}^{2+}$ beam with energy of 7.25 MeV/u was obtained with high intensity of 38 eμA. These beams were supplied with sufficient intensity for nuclear experiments, RI production and biological irradiation.

This year, we changed the method of iron vapor supply to the ion source. Cylinder method of inserting cylindrical material (called a cylinder) made of SUS was introduced in the $^{56}\text{Fe}^{15+}$ beam production. In this way, the reproducibility and stability of $^{56}\text{Fe}^{15+}$ beam was greatly improved

Recently, we measured the beam intensity inside the plasma chamber of the ion source. $^{56}\text{Fe}^{15+}$ beam was tuned and measured by monitoring the light intensity of plasma. As the $^{56}\text{Fe}^{15+}$ beam intensity injected into the analyzing magnet increased, the beam was clearly assigned on the spectrum measured by the analyzer, and the tuning time was shortened. The results are described.

2. Cylinder method

The schematic diagram of the Hyper ECR ion source is shown in Fig. 1. The ECR zone is formed by the mirror coil of MC1, MC2 and a hexapole magnet. The cylinder size is 10 mm in outer diameter, 0.5 mm in wall thickness and 80 mm in length. And gas and RF are introduced into the chamber to generate plasma. The cylinder is inserted into the plasma from the non-axial direction of the gas inlet side.

The length of the ECR zone is about 70 mm. The tip of the cylinder is inserted to a position approximately 10 mm away from the end of the ECR zone. Iron vapor was regulated by changing the gap between the tip of the cylinder and the ECR zone. The cylindrical material gave reasonable evaporation, and the beam intensity was stabilized by fine adjustment of the position.

3. Beam analysis by light intensity

A grating monochromator and a photomultiplier are attached to the straight line of the analyzing magnet of the Hyper ECR ion source [4]. And then, each ion species generated in the plasma emits the light having a specific wavelength. The optical line spectrum of the ion source under operation of $^{56}\text{Fe}^{15+}$ ion beam is shown in

Fig. 1: Schematic diagram of the Hyper ECR ion source. The cylindrical material was inserted from the gas inlet side along the wall surface of the plasma chamber and its tip is brought close to the ECR zone.

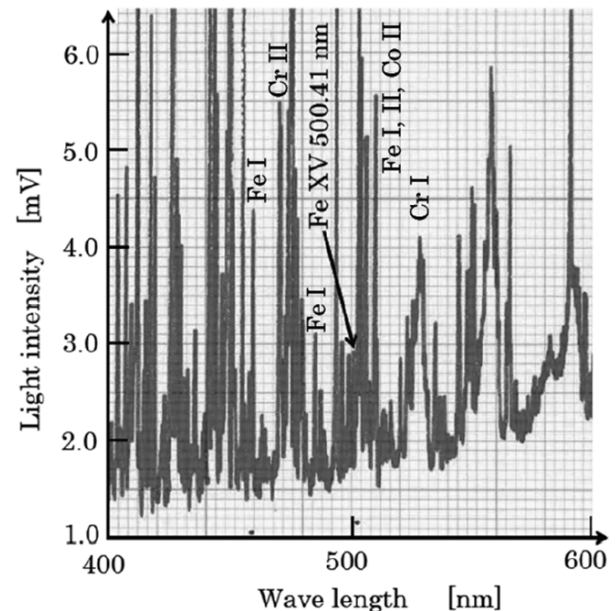
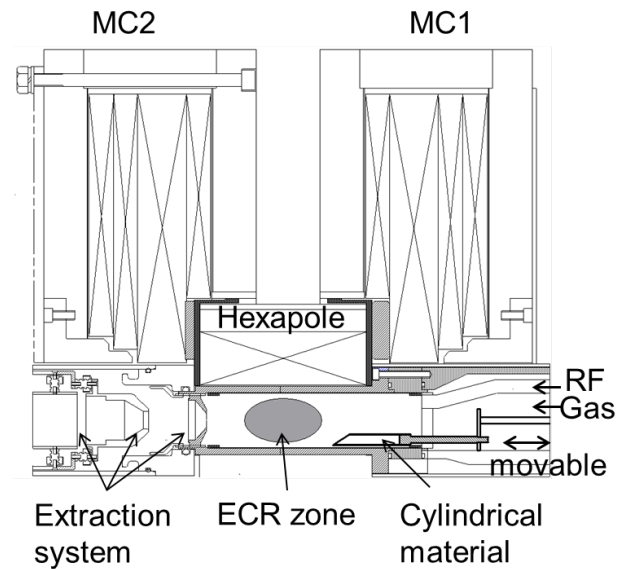


Fig. 2: Optical line spectrum of the Hyper ECR ion source under $^{56}\text{Fe}^{15+}$ beam operation.

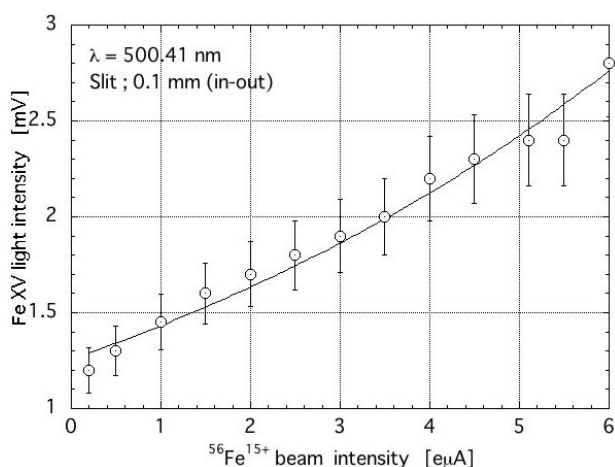


Fig. 3: Light intensity of Fe XV ($\lambda = 500.41$ nm) line spectrum as function of analyzed $^{56}\text{Fe}^{15+}$ beam intensity.

Fig. 2. Wavelength of Iron line spectrum was determined from NIST Database. Light intensity of Fe XV line spectrum was observed at $\lambda = 500.41$ nm [5].

Light intensity of Fe XV line spectrum as a function of analyzed beam intensity is shown in Fig. 3. This result shows a strong correlation between light intensity and beam current. From the graph, we were able to find the beam intensity within the plasma chamber.

We monitored the light intensity of the plasma, increased the beam intensity, and injected it into the analyzing magnet. The beam intensity of $^{56}\text{Fe}^{15+}$ was enhanced about 3 times compared to the beam like $^{52}\text{Cr}^{14+}$ and $^{63}\text{Cu}^{16+}$ approaching the charge to mass ratio. So we clearly assigned $^{56}\text{Fe}^{15+}$ beam on the spectrum measured with the analyzing magnet.

4. Some results of $^{56}\text{Fe}^{15+}$ beam production

1) In the ion beam production of $^{56}\text{Fe}^{15+}$, we baked first the gas adsorbed on the wall of the plasma chamber. The parameter were 580 A for MC1, 520 A for MC2 and 500 W RF power. When the degree of vacuum reached 10^{-5} Pa, the RF power was lowered to 300 W and the cylinder material was inserted until the light intensity increase to 1 mV. After baking out, we got a stable beam by placing the tip of the cylindrical material at the optimum position.

2) This time, we tuned first the analyzed $^{56}\text{Fe}^{15+}$ beam intensity by the ion source parameters while monitoring the light intensity of the plasma, then, extracted the beam with parameters of extraction voltage, lens system and analyzing magnet. In this way, the beam was stabilized and the intensity was enhanced by adjusting the parameters of ion generation and beam extraction independently.

3) The beam intensity extracted from the ion source required for biological irradiation is about 3 e μA . In the conventional FeO rod method, the light intensity was 2 to 3 mV and the $^{56}\text{Fe}^{15+}$ beam intensity was 1 to 3 e μA . However, as the rod approached the ECR zone the total current sharply increased and the beam became unstable. On the other hand, the cylinder method was able to feed

the material following the light intensity, and the beam became very stable. Therefore, the beam intensity was increased to 6 to 8 e μA at the light intensity of 5 to 6 mV.

5. Summary

We introduced the cylinder method to the Hyper ECR ion source and produced the stable $^{56}\text{Fe}^{15+}$ beam. By monitoring the light intensity of the plasma, optimization of iron vapor supply, independence of beam adjustment, and $^{56}\text{Fe}^{15+}$ beam analysis by analyzer of the ion source were possible. As a result, the reproducibility of $^{56}\text{Fe}^{15+}$ ion beam intensity was improved.

References

- [1] Y. Ohshiro, S. Yamaka, S. Watanabe, K. Kobayashi, Y. Kotaka *et al.*, Rev. Sci. Instrum. **85** (2014) 02A912.
- [2] Y. Ohshiro, S. Yamaka *et al.*, RIKEN Accel. Prog. Rep. **39** (2005) 231.
- [3] Y. Ohshiro, S. Watanabe *et al.*, CNS Annual Report 2004 (2003) 71.
- [4] H. Muto *et al.*, Rev. Sci. Instrum. **84** (2013) 073304.
- [5] H. Muto, Y. Ohshiro *et al.*, CNS Annual Report 2014 (2012) 69.

Theoretical Nuclear Physics

Variational Monte Carlo method for nuclear shell-model calculations

N. Shimizu^a, and T. Mizusaki^b

^aCenter for Nuclear Study, Graduate School of Science, The University of Tokyo

^bInstitute of Natural Sciences, Senshu University

1. Introduction

The large-scale shell model (LSSM) calculation is one of the most powerful methods to describe the nuclear spectroscopic information precisely. However, the dimension of the Hamiltonian matrix in the LSSM tends to be huge, and often surpasses the capability of the state-of-the-art supercomputers. In order to avoid this problem and to describe the shell-model wave function in a sophisticated form, we have introduced variational Monte Carlo (VMC) in LSSM calculations for even-mass nuclei [1]. In the present report, we discuss the VMC method with the variation after the total angular-momentum projection (VAP) for odd-mass nuclei. This report is based on Ref. [2].

2. Formulation of the VMC

We briefly describe the formulation of the VMC. The trial wave function of the VMC is written as

$$|\psi\rangle = GP|\phi\rangle, \quad (1)$$

where the $|\phi\rangle$ is a pair-correlated wave function and P is a projection operator, both of which are discussed later. The operator G is the Gutzwiller-like factor [3] as

$$G = e^{\sum_{i \leq j} \alpha_{ij} n_i n_j} \quad (2)$$

where n_i is the number operator of the single-particle orbit i and α 's are variational parameters.

For odd-mass nuclei with the N valence neutrons and the Z valence protons, the $|\phi\rangle$ is defined as

$$|\phi\rangle = \left(\sum_l h_l c_l^\dagger \right) \left(\sum_{kk'} f_{kk'} c_k^\dagger c_{k'}^\dagger \right)^{(N+Z-1)/2} |-\rangle \quad (3)$$

where f is a skew-symmetric matrix, $f_{kk'} = -f_{k'k}$, the matrix elements of which are variational parameters. The $|-\rangle$ is an inert core and the c_k^\dagger 's are proton or neutron creation operator of the single-particle state k . The h_l are the variational parameters to describe the unpaired-particle state. Note that this trial wave function well describes the correlations not only of the identical-particles pairing but also of the proton-neutron pairing, while the z -component of the isospin is not conserved.

The projection operator P serves to restore the rotational symmetry, parity symmetry and z -component of isospin such as

$$P = P^{T_z} P^\pi P_M^I = P^{T_z} P^\pi P_M \cdot \tilde{P}_M^I \quad (4)$$

where P^{T_z} , P^π and P_M^I are projectors of the z -component of the isospin, the parity π , and the total angular momentum (I, M) , respectively. The total angular momentum operator

is decomposed into the $\langle J_z \rangle = M$ projection and the rest such as $P_M^I = P_M \tilde{P}_M^I$ and

$$\begin{aligned} \tilde{P}_M^I &\equiv \frac{2I+1}{4\pi} \sum_{K=-I}^I g_K \int d\gamma d\beta \sin\beta d_{MK}^I(\beta) \\ &\times e^{-iK\gamma} e^{iJ_y\beta} e^{iJ_z\gamma}. \end{aligned} \quad (5)$$

The $d_{MK}^I(\beta)$ is Wigner's d -function and g_K denotes the $2I+1$ variational parameters. In the VMC framework, the remaining projectors, $P^{T_z} P^\pi P_M$, is realized by the random walker of m -scheme basis states, which will be described hereafter.

The projection operator $P^{T_z} P^\pi P_M$ is expressed as a linear combination of the complete set in the m -scheme basis states as

$$P^{T_z} P^\pi P_M = \sum_{m \in \{M^\pi\}} |m\rangle \langle m|, \quad (6)$$

where the m -scheme basis state $|m\rangle$ is defined as

$$|m\rangle = c_{m_1}^\dagger c_{m_2}^\dagger \cdots c_{m_N}^\dagger |-\rangle \quad (7)$$

which is parametrized by a set of occupied single-particle states, $m = \{m_1, m_2, \dots, m_{N+Z}\}$. The $\sum_{m \in M^\pi}$ denotes the summation of any $|m\rangle$ in the subspace with $T_Z = (N-Z)/2$, $J_z = M$, and π -parity. It is convenient to take $M = I$, especially for the yrast states.

The energy expectation value of the trial wave function is obtained as

$$\begin{aligned} \langle H \rangle &= \frac{1}{\sum_{m \in M^\pi} |\langle m|\psi\rangle|^2} \sum_{m \in M^\pi} |\langle m|\psi\rangle|^2 \frac{\langle m|H|\psi\rangle}{\langle m|\psi\rangle} \\ &= \sum_{m \in M^\pi} p(m) E_l(m) \end{aligned} \quad (8)$$

where $p(m)$ is defined as $p(m) = |\langle m|\psi\rangle|^2 / \sum_m |\langle m|\psi\rangle|^2$. $E_l(m)$ is called the local energy and is defined as

$$\begin{aligned} E_l(m) &= \frac{\langle m|H|\psi\rangle}{\langle m|\psi\rangle} \\ &= \frac{1}{\langle m|\psi\rangle} \sum_{m' \in M^\pi} \langle m|H|m'\rangle \langle m'|\psi\rangle \end{aligned} \quad (9)$$

where the matrix $H_{mm'} = \langle m|H|m'\rangle$ is sparse and then the summation concerning m' can be computed efficiently since the shell-model Hamiltonian H is a two-body interaction and has good parity and rotational symmetries.

The weighted summation $\sum_m p(m)$ in Eq.(8) is estimated stochastically using the Markov Chain Monte Carlo (MCMC) method in which $|m\rangle$ walks randomly in the $\{M^\pi\}$ subspace obeying the probability $p(m)$. Such random walker of the m scheme basis state was adopted also in Refs. [1, 4, 5].

The overlap between the m -scheme basis state and the $|\psi\rangle$ is obtained by

$$\langle m|\psi\rangle = G(m)\langle m|\tilde{P}_M^I|\phi\rangle \quad (10)$$

with $G|m\rangle = G(m)|m\rangle$. Note that G is a diagonal operator for the m -scheme basis representation and is commutable with the projection operator P . The projected overlap, $\langle m|\tilde{P}_M^I|\phi\rangle$, is computed by performing the double integration in Eq. (5) utilizing the Pfaffian [2].

The variational parameters α , h , f , and g are determined so that the energy is minimized by utilizing the stochastic reconfiguration method [6], which is an improved version of the steepest gradient method. The energy gradient of these parameters are also obtained stochastically in the same way as the energy expectation value.

3. Numerical results

In this section, we demonstrate that the angular-momentum projected energy is minimized in the VAP framework and is compared with the exact shell-model energies. We take the shell-model calculation of ^{25}Mg with the sd -shell model space as an example. The USD interaction is adopted as an effective interaction [7]. For the test of the VMC calculation, we use a realistic residual interaction, not a schematic interaction so as to properly judge the feasibility of the method.

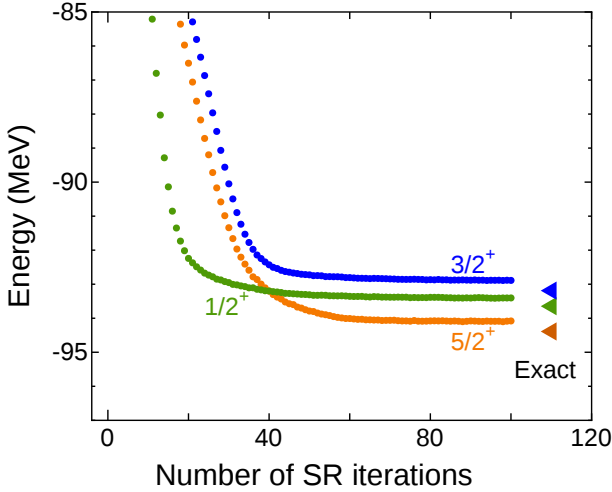


Figure 1. Convergence of energies of $I^\pi = 5/2^+$ (orange circles), $1/2^+$ (green) and $3/2^+$ (blue) states of ^{25}Mg obtained by the VAP VMC as functions of the number of the SR iterations. The rightmost triangles denote the exact shell-model energies.

Figure 1 shows the convergence of the energy expectation value of the VAP as a function of the number of the iterations of the stochastic reconfiguration (SR) method [6]. In the MCMC process, we adopt the Gibbs sampler with 64 random walkers, each of which contains 5000 sample steps after 1000 burn-in steps. The VAP energies of the yrast $5/2^+$, $1/2^+$, and $3/2^+$ states decrease as the number of SR iterations increases. During the iterations, the statistical error of the energy expectation value is around 5 keV. They well converge and agree with the exact shell-model energies within 300 keV at most, while the excitation energies,

namely the energy gap between the states, show the better agreements. Note that the variation before the total angular-momentum projection [1] does not work in this case. Because the $5/2^+$ energy is lower than the $1/2^+$ energy, the variation after the $J_z = 1/2^+$ projection would converge to the $J = 5/2^+$ state, not the $J = 1/2^+$ state.

4. Summary

We have introduced the VMC method to solve the LSSM calculations in Ref. [1]. In this report, we extended the VMC framework to the odd-mass case with the variation after the total-angular-momentum projection. Further extensions of the present VMC framework with the “approximate” angular-momentum technique and the extrapolation method are also discussed in Ref. [2]. Further investigation to improve the precision of the approximation by utilizing the Restricted Boltzmann Machine is ongoing.

This work was partly supported by KAKENHI grants (25870168, 17K05433) from JSPS and priority issue (Elucidation of the fundamental laws and evolution of the universe, hp170230 and hp180179) to be tackled by using Post K Computer from MEXT and JICFuS. This work was also partly supported by the research grant of the Senshu Research Abroad Program (2018) for one of the authors, (T.M.).

References

- [1] T. Mizusaki and N. Shimizu, Phys. Rev. C **85** 021301(R) (2012).
- [2] N. Shimizu and T. Mizusaki, Phys. Rev. C **98** 054309 (2018).
- [3] D. Tahara and M. Imada, J. Phys. Soc. Jpn. **77**, 114701 (2008).
- [4] N. Shimizu, T. Mizusaki, and K. Kaneko, Phys. Lett. B **723**, 251 (2013).
- [5] M. Lingle and A. Volya, Phys. Rev. C **91**, 064304 (2015).
- [6] S. Sorella, Phys. Rev. B **64**, 024512 (2001).
- [7] B. A. Brown and B. H. Wildenthal, Ann. Rev. Nucl. Part. Sci. **38**, 29 (1988).

Double Gamow-Teller transitions in connection to $\beta\beta$ decay

J. Menéndez, N. Shimizu and K. Yako

Center for Nuclear Study, Graduate School of Science, The University of Tokyo

While Gamow-Teller (GT) transitions in nuclei have provided precious nuclear structure information for decades [1–3], planning a dedicated program to observe double GT (DGT) transitions has only become feasible in the recent years [4–6]. DGT observations are relevant from the point of view of nuclear structure, and, in addition, they are very promising in connection to $\beta\beta$ decay. In particular, DGT transitions could be related to $\beta\beta$ decay in a similar manner to the relation between GT transitions and β decay. This connection would be very valuable especially if by performing DGT measurements it is possible to extract some information on neutrinoless $\beta\beta$ decay. This unobserved $\beta\beta$ is not permitted in the standard model of particle physics, but its detection will establish if neutrinos are its own antiparticle (Majorana particle). Furthermore, neutrinoless $\beta\beta$ decay can provide information on the origin of the dominance of matter over antimatter in the universe, and the absolute value of the neutrino mass.

Motivated to investigate this relation, we calculated with the large-scale shell model the DGT strength distribution of the lightest $\beta\beta$ emitter ^{48}Ca [7], defined as

$$B(DGT^-; \lambda) = \langle f | \left| \sum_{a,b} \boldsymbol{\sigma}_a \tau_a^+ \times \boldsymbol{\sigma}_b \tau_b^+ \right|^{(\lambda)} | i \rangle \right|^2, \quad (1)$$

where $\boldsymbol{\sigma}$ is the spin and τ^+ the isospin raising operator, the tensor coupling can get values $\lambda = 0, 2$, and i and f denote the initial and final nuclear states, respectively. We have continued our research program by exploring which parts of the nuclear interaction the DGT distribution is more sensitive to [8]. We have found that the energy of the DGT resonance is very sensitive to the amount of isovector (like-particle) pairing in the nuclear interaction, while the width of the distribution depends more on the strength of the isoscalar pairing. Interestingly, neutrinoless $\beta\beta$ decay nuclear matrix elements are also very sensitive to the isovector and isoscalar pairing strengths [9–11]. Combining the dependence on both observables it is possible to obtain a correlation between the energy of the DGT resonance of ^{48}Ca and the value of the neutrinoless $\beta\beta$ decay nuclear matrix element [8].

Finally we study the DGT transition to the ground state of the final nucleus for even-even nuclei (therefore only the coupling to $\lambda = 0$ is relevant). The similarity between this DGT matrix element and neutrinoless $\beta\beta$ decay is apparent because [12]

$$M^{0\nu\beta\beta} = \sum_{X=GT,F,T} \langle f | \sum_{a,b} H_X(r_{ab}) S_X \tau_a^+ \tau_b^+ | i \rangle, \quad (2)$$

$$H_X(r_{ab}) = \frac{2R}{\pi} \int_0^\infty q^2 dq \frac{j_X(qr_{ab}) h_X(q)}{q(q+\mu)}, \quad (3)$$

where the GT part with $S_{GT} = \boldsymbol{\sigma}_a \cdot \boldsymbol{\sigma}_b$ dominates over the Fermi (F) and tensor (T) ones. The momentum transfer

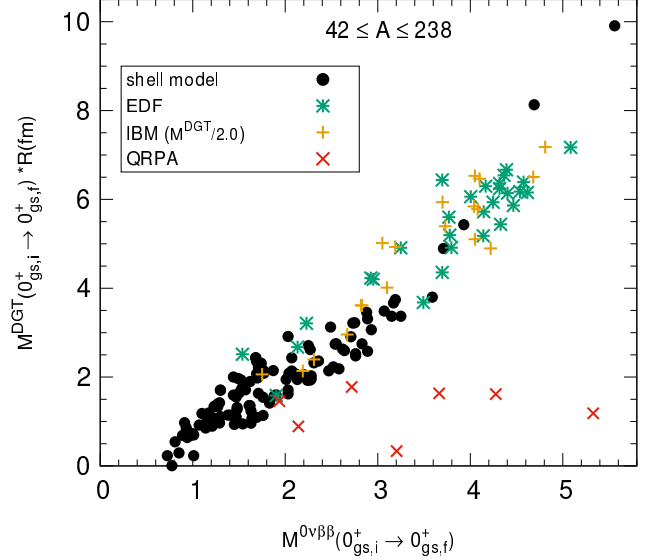


Figure 1. Correlation between the DGT (M^{DGT}) and neutrinoless $\beta\beta$ decay ($M^{0\nu\beta\beta}$) nuclear matrix elements for a set of nuclei covering a very wide range of mass numbers $42 \leq A \leq 238$. Results with the shell model (black points) are compared to the energy-density functional theory (EDF, green stars), the interacting boson model (IBM, orange crosses) and the quasiparticle random-phase approximation (QRPA, red x crosses). DGT matrix elements are multiplied by $R = 1.2A^{1/3}$ to compensate for a similar factor in the definition of $M^{0\nu\beta\beta}$.

q also enters the spherical Bessel functions $j(qr_{ab})$, and the nuclear radius $R = 1.2A^{1/3}$ fm is introduced for convenience. The explicit form of $h_X(q)$ and μ can be found in Ref. [13]. The spin and isospin structure of the DGT and neutrinoless $\beta\beta$ matrix elements is the same, and the two processes basically differ in their momentum transfer.

Figure 1 shows shell model results for the DGT transitions to the ground state, and neutrinoless $\beta\beta$ matrix element for the same nucleus. A very wide range of isotopes from ^{42}Ca to ^{136}Xe is covered in the shell model calculations, including several $\beta\beta$ emitters. A very good correlation between the two observables is found, valid across the nuclear chart. Figure 1 also compares results from other many-body methods used to calculate neutrinoless $\beta\beta$ decay. While the energy-density functional theory and interacting boson model results support the very good correlation suggested by the shell model, the quasiparticle random-phase approximation results find no correlation at all.

In order to understand the correlation between DGT and neutrinoless $\beta\beta$ matrix elements Fig. 2 shows their density distribution as a function of the internucleon distance and the momentum transfer. Figure 2 shows that, even though the momentum transfers are very different (vanishing for

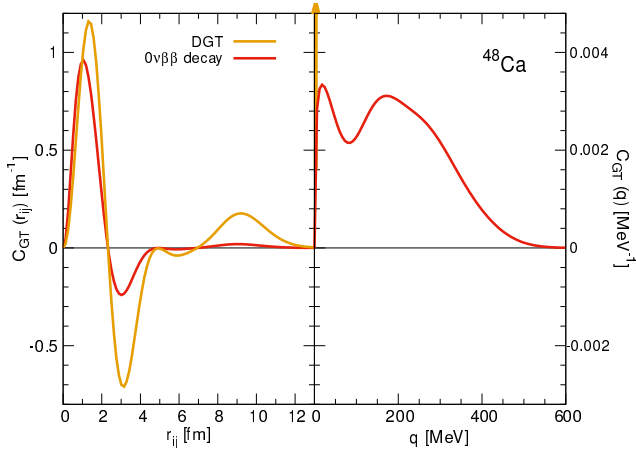


Figure 2. Density distribution of the DGT and neutrinoless $\beta\beta$ matrix elements as a function of the internucleon distance r_{ij} and the momentum transfer q for ^{48}Ca .

DGT and $q \sim 100$ MeV for neutrinoless $\beta\beta$ decay), in both cases it is only nucleons relatively close to one another that contribute to the matrix elements (note the cancellation between intermediate a long range contributions in the DGT transition). The proportionality between DGT and neutrinoless $\beta\beta$ can be understood due to the dominance of the short-range contributions [14, 15].

In short, our study has found a very good correlation between DGT transitions and neutrinoless $\beta\beta$ decay, which suggests that a measurement of the DGT transition to the ground state can be used to constrain the value of the neutrinoless $\beta\beta$ matrix element for that nucleus. We will explore in more detail the origin and implications of this correlation in future work.

References

- [1] M. Ichimura, H. Sakai, and T. Wakasa, *Prog. Part. Nucl. Phys.* **56**, 446 (2006).
- [2] K. Yako *et al.*, *Phys. Rev. Lett.* **103**, 012503 (2009).
- [3] D. Frekers, P. Puppe, J. H. Thies, and H. Ejiri, *Nucl. Phys. A* **916**, 219 (2013).
- [4] M. Takaki *et al.*, *CNS Annual Report* **94**, 9 (2014).
- [5] M. Takaki *et al.*, *JPS Conf. Proc.* **6**, 020038 (2015).
- [6] T. Uesaka *et al.*, *RIKEN RIBF NP-PAC*, NP1512-RIBF141 (2015).
- [7] N. Shimizu, J. Menéndez, and K. Yako, *CNS Annual Report* **96**, 65 (2016).
- [8] N. Shimizu, J. Menéndez, and K. Yako, *Phys. Rev. Lett.* **120**, 142502 (2018).
- [9] P. Vogel and M. R. Zirnbauer, *Phys. Rev. Lett.* **57**, 3148 (1986).
- [10] E. Caurier, J. Menéndez, F. Nowacki, and A. Poves, *Phys. Rev. Lett.* **100**, 052503 (2008).
- [11] J. Menéndez, N. Hinohara, J. Engel, G. Martínez-Pinedo, and T. R. Rodríguez, *Phys. Rev. C* **93**, 014305 (2016).
- [12] J. Engel, and J. Menéndez, *Rep. Prog. Phys.* **80**, 046301 (2017).
- [13] J. Menéndez, *J. Phys. G* **45** 014003 (2018).
- [14] E. R. Anderson, S. K. Bogner, R. J. Furnstahl, and R. J. Perry, *Phys. Rev. C* **82**, 054001 (2010).
- [15] S. K. Bogner, and D. Roscher, *Phys. Rev. C* **86**, 064304 (2012).

Nuclear studies for the direct detection of dark matter

J. Menéndez^a, M. Hoferichter^b, P. Klos^{c,d} and A. Schwenk^{c,d,e}

^aCenter for Nuclear Study, Graduate School of Science, The University of Tokyo

^bInstitute for Nuclear Theory, University of Washington

^cInstitut für Kernphysik, Technische Universität Darmstadt

^dExtreMe Matter Institute EMMI, GSI Helmholtzzentrum für Schwerionenforschung

^eMax-Planck-Institut für Kernphysik

Dark matter constitutes about a quarter of the energy-density of the universe and 80% of its mass, but its composition remains elusive. A key step to understand the nature of dark matter is the direct detection in the laboratory [1]. This experimental program is led by searches that aim to observe the scattering of dark matter particles off atomic nuclei [2]. The interpretation of these direct detection experiments, however, depends on the nuclear matrix elements, or structure factors, that describe the dark matter scattering off nuclei. One of the most promising dark matter candidates are weakly interacting massive particles (WIMPs), which can couple to the standard model fields, quarks and gluons [3]. Since the nature of this hypothetical interaction is unknown, the most general form of WIMP interactions with nuclei need to be considered.

It is useful to focus on the WIMP-nucleus interactions that receive coherent contributions from several nucleons in the nucleus. In the case of xenon or germanium detectors, complete coherence can enhance the corresponding nuclear structure factors by a factor $A^2 \sim 10^4$. Also, we keep only terms up to third order [4] in chiral effective field theory (EFT) [5–7], an effective theory of quantum chromodynamics, QCD, valid at nuclear structure energies. Chiral EFT organizes the interaction of nucleons with WIMPs according to a counting given by the chiral symmetry of QCD. Therefore, the lowest orders in chiral EFT are the ones expected to be dominant based on the symmetries of QCD.

Under these assumptions, the cross-section for dark matter scattering off nuclei can be written as a function of the momentum transfer q as

$$\begin{aligned} \frac{d\sigma}{dq^2} = & \frac{1}{4\pi v^2} \left| \sum_{I=\pm} \left(c_I^M - \frac{q^2}{m_N^2} c_I^M \right) \mathcal{F}_I^M(q^2) \right. \\ & + c_\pi \mathcal{F}_\pi(q^2) + c_b \mathcal{F}_b(q^2) \\ & \left. + \frac{q^2}{2m_N^2} \sum_{I=\pm} c_I^{\Phi''} \mathcal{F}_I^{\Phi''}(q^2) \right|^2, \end{aligned} \quad (1)$$

where v is the WIMP velocity, m_N the nucleon mass, and I stand for isovector (equal, +) or isoscalar (opposite, -) contributions from neutrons and protons. The coefficients c encode the information on the coupling of WIMPs to the quarks and gluons in the nucleon. The nuclear structure factors $\mathcal{F}(q^2)$ need to be calculated theoretically in nuclear many-body calculations. Detailed expressions of all terms in Eq. (1) can be found in Ref. [8].

Figure 1 shows the leading nuclear structure factors corresponding to the coupling of a WIMP to one nucleon (one-body terms, 1b) in the most abundant germa-

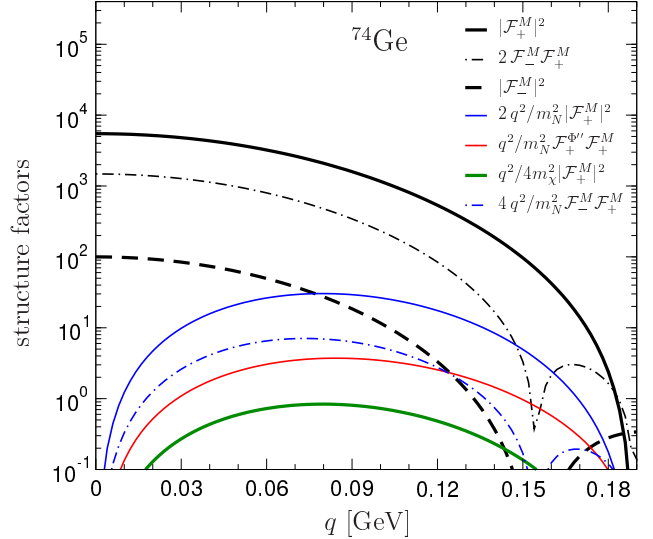


Figure 1. Leading nuclear structure factors for WIMPs coupling to one nucleon in ^{74}Ge , from Eq. (1) and assuming $c = 1$ for all coefficients. Thick black (solid and dashed) and green (solid) lines correspond to individual terms, while all other curves represent interferences. For instance, the red line shows the nuclear structure factor for the interference between the $\mathcal{F}_+^M(q^2)$ and $q^2/(2m_N^2)\mathcal{F}_+^{\Phi''}(q^2)$ terms in Eq. (1).

nium isotope, ^{74}Ge . All coefficients are taken $c = 1$. The six individual 1b contributions $\mathcal{F}_+^M(q^2)$, $\mathcal{F}_-^M(q^2)$, $q^2/m_N^2\mathcal{F}_+^M(q^2)$, $q^2/m_N^2\mathcal{F}_-^M(q^2)$, $q^2/(2m_N^2)\mathcal{F}_+^{\Phi''}(q^2)$ and $q^2/(2m_N^2)\mathcal{F}_-^{\Phi''}(q^2)$, plus all interference terms are considered. Therefore, Fig. 1 shows the expected hierarchy between the different WIMP-nucleon interactions based on chiral EFT and nuclear structure effects. The dominant contribution is characterized by \mathcal{F}_+^M , where all A nucleons in the nucleus contribute coherently. This is interaction considered in standard spin-independent searches [9, 10].

Figure 2 shows, also for ^{74}Ge , the main nuclear structure factors that contain a contribution from the coupling of WIMPs to two nucleons (two-body terms, 2b). While similar terms—meson-exchange currents—have been extensively studied in electromagnetic and weak nuclear interactions [11, 12], they are usually neglected in the analysis of dark matter interactions with nuclei—a notable exception are the spin-dependent interactions proposed in Ref. [13]. We distinguish two independent two-nucleon currents that do not vanish at $q = 0$, $\mathcal{F}_\pi(q^2)$ and $\mathcal{F}_b(q^2)$. They represent the coupling of the WIMP to the pion exchanged between two nucleons, and can interfere with the dominant

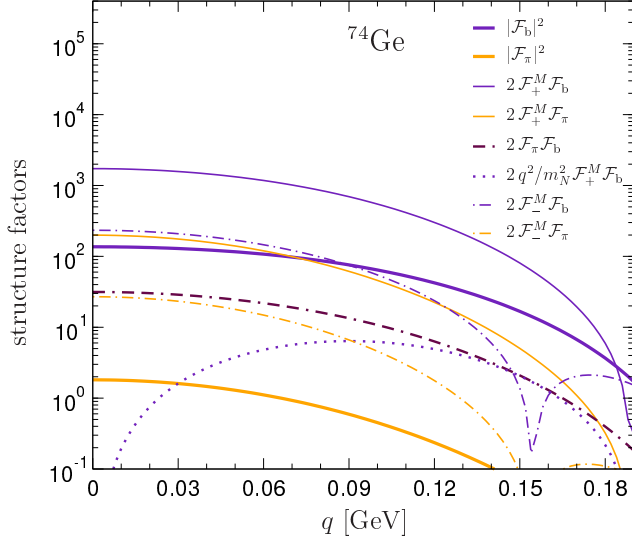


Figure 2. Leading nuclear structure factors for WIMPs coupling to two nucleons in ^{74}Ge , from Eq. (1) and assuming $c = 1$ for all coefficients. Interferences with terms describing WIMPs coupling to one nucleon are also included. Thick indigo and orange lines show individual terms, while all other curves correspond to interferences. For instance, the maroon dotted-double-dashed line represents the nuclear structure factor for the interference between the $\mathcal{F}_\pi(q^2)$ and $\mathcal{F}_b(q^2)$ terms in Eq. (1).

one-nucleon coupling. Two nucleon currents are expected to be the main correction to the leading spin-independent WIMP-nucleus interaction.

In previous work Ref. [8], we studied the WIMP scattering off xenon isotopes. Our present research extends this study to other nuclei which are used in direct dark matter detection experiments, such as argon, germanium, fluorine and silicon. In all these calculations we use the state-of-the-art nuclear shell model with phenomenological interactions [14–16]. A second novelty of the present research is that we have clarified the origin of the two independent WIMP couplings to the pion exchanged by two nucleons, adding terms missing in Ref. [8]. Future research will focus on extending this study to WIMP-nucleus interactions which do not receive coherent contributions from many nucleons, such as spin-dependent interactions.

References

- [1] L. Baudis, J. Phys. G **43**, 044001 (2016).
- [2] T. Marrodán Undagoitia and L. Rauch, J. Phys. G **43**, 013001 (2016).
- [3] G. Bertone, D. Hooper and J. Silk, Phys. Rept. **405**, 279 (2005).
- [4] M. Hoferichter, P. Klos and A. Schwenk, Phys. Lett. B **746**, 410 (2015).
- [5] E. Epelbaum, H. W. Hammer and U.-G. Meißner, Rev. Mod. Phys. **81**, 1773 (2009).
- [6] R. Machleidt and D. R. Entem, Phys. Rept. **503**, 1 (2011).

- [7] H.-W. Hammer, A. Nogga and A. Schwenk, Rev. Mod. Phys. **85**, 197 (2013).
- [8] M. Hoferichter, P. Klos, J. Menéndez and A. Schwenk, Phys. Rev. D **94**, 063505 (2016).
- [9] E. Aprile *et al.* [XENON Collaboration], Phys. Rev. Lett. **121**, 111302 (2018).
- [10] P. Agnes *et al.* [DarkSide Collaboration], Phys. Rev. Lett. **121**, 081307 (2018).
- [11] S. Bacca and S. Pastore, J. Phys. G **41**, 123002 (2014).
- [12] S. Pastore, A. Baroni, J. Carlson, S. Gandolfi, S. C. Pieper, R. Schiavilla and R. B. Wiringa, Phys. Rev. C **97**, 022501 (2018).
- [13] J. Menéndez, D. Gazit and A. Schwenk, Phys. Rev. D **86**, 103511 (2012).
- [14] B. A. Brown and W. A. Richter, Phys. Rev. C **74**, 034315 (2006).
- [15] E. Caurier, J. Menéndez, F. Nowacki and A. Poves, Phys. Rev. C **75**, 054317 (2007) Erratum: [Phys. Rev. C **76**, 049901 (2007)] [nucl-th/0702047].
- [16] J. Menéndez, A. Poves, E. Caurier and F. Nowacki, Nucl. Phys. A **818**, 139 (2009) [arXiv:0801.3760 [nucl-th]].

Monte Carlo shell model calculations for shape staggering in Hg isotopes

Y. Tsunoda^a and T. Otsuka^{b,a,c,d,e}

^aCenter for Nuclear Study, the University of Tokyo

^bDepartment of Physics, the University of Tokyo

^cRIKEN Nishina Center

^dInstituut voor Kern- en Stralingsfysica, KU Leuven, Belgium

^eNational Superconducting Cyclotron Laboratory, Michigan State University, USA

Nuclear shape is one of the most important properties for the study of the nuclear collectivity. The neutron-deficient Hg isotopes show staggering of charge radius [1–4]. The odd- A isotopes $^{181,183,185}\text{Hg}$ have large charge radius while the other Hg isotopes have smaller charge radius. We have investigated shapes of these Hg isotopes by using the Monte Carlo shell model (MCSM) calculations [5–7] and this work is contained in Ref. [4].

In order to describe nuclear deformation in the shell model, we have to use sufficiently large model space. The model space used in our calculations is the $0g_{7/2}$, $1d_{5/2}$, $1d_{3/2}$, $2s_{1/2}$, $0h_{11/2}$, $0h_{9/2}$, $1f_{7/2}$, $1f_{5/2}$, $2p_{3/2}$, $2p_{1/2}$, and $0i_{13/2}$ orbits for protons, and the $0h_{9/2}$, $1f_{7/2}$, $1f_{5/2}$, $2p_{3/2}$, $2p_{1/2}$, $0i_{13/2}$, $0i_{11/2}$, $1g_{9/2}$, $1g_{7/2}$, $2d_{5/2}$, $2d_{3/2}$, $3s_{1/2}$, and $0j_{15/2}$ orbits for neutrons. We use the effective interaction as is used in Ref. [4]. We performed MCSM calculations in order to use this large model space. In the MCSM, the wave function $|\Psi\rangle$ is represented as a superposition of the projected Slater determinants (MCSM basis vectors) as

$$|\Psi\rangle = \sum_{n,K} f_{n,K} P_{MK}^{J\pi} |\phi_n\rangle,$$

where $P_{MK}^{J\pi}$ is the angular-momentum and parity projector and $|\phi_n\rangle$ is a Slater determinant. Coefficients $f_{n,K}$ are determined by the diagonalization of the Hamiltonian matrix in the subspace spanned by the MCSM basis vectors $P_{MK}^{J\pi} |\phi_n\rangle$. $|\phi_n\rangle$ is determined to minimize the expectation value of the energy of the wave function. We can analyze the nuclear intrinsic shape by using the MCSM basis vector before projection, $|\phi_n\rangle$. In this method, we use the figure (referred to as T-plot) of the potential energy surface (PES) with circles indicating the shape of the MCSM basis vector. An example of T-plot is shown in Fig. 1(d). The PES is calculated by constrained Hartree-Fock method using the shell-model effective interaction. We calculate the quadrupole moments, Q_0 and Q_2 , of the MCSM basis vector before projection and locate a circle at the corresponding place in the PES. The area of the circle is proportional to the overlap probability between the MCSM basis vector $P_{MK}^{J\pi} |\phi_n\rangle$ and the wave function $|\Psi\rangle$. Thus, the distribution pattern of the circles indicates the nuclear intrinsic shape for the wave function. Although the $J = 0$ wave function is isotropic, we can analyze intrinsic shape of the 0^+ state because we use the MCSM basis vector before the angular-momentum projection. We estimate the charge radius of the calculated state from the quadrupole deformation parameter β_2 deduced from the T-

plot. β_2 is calculated as

$$\beta_2 = f_{\text{scale}} \sqrt{\frac{5}{16\pi}} \frac{4\pi}{3R^2A} \sqrt{(Q_0)^2 + 2(Q_2)^2},$$

where $R = 1.2A^{1/3}$ fm and $f_{\text{scale}} = e_p/e + e_n/e$ with effective charges $e_p = 1.6e$ and $e_n = 0.6e$. The mean-square charge radius $\langle r^2 \rangle$ is calculated as

$$\langle r^2 \rangle = \langle r^2 \rangle_{\text{DM}} \left(1 + \frac{5}{4\pi} \langle \beta_2 \rangle^2 \right),$$

where $\langle r^2 \rangle_{\text{DM}}$ is the droplet model mean-square charge radius. Details of the procedure are described in Ref. [4].

We calculated several states of the nuclei from ^{177}Hg to ^{186}Hg . Figure 1(d) shows the T-plots of the $1/2_1^-$ state of ^{185}Hg and the 0_1^+ state of ^{186}Hg and the former T-plot shows some quantum fluctuation of the shape. Because of the quantum fluctuation, the calculated charge radius is shown by box with some height in Fig. 1(a). The calculated states have different shape and one of the calculated states has charge radius corresponding to the experimental ground state for each nucleus. These states have the lowest energy of the calculated states except for ^{181}Hg and the consistent magnetic moment with the experimental ground state. The calculated energy difference between the $1/2_3^-$ and $1/2_1^-$ states of ^{181}Hg is only 218 keV. Figure 1(b) shows the comparison of the magnetic moment of the MCSM calculations and the experiments. The magnetic moment is calculated with a spin quenching factor of 0.9. The experimental $13/2^+$ isomeric state of ^{185}Hg has smaller charge radius and the calculated spherical $13/2_2^+$ state has similar charge radius and magnetic moment to the experimental isomeric state.

We show the occupation numbers of the calculated states in order to discuss the mechanism of the shape staggering. Figure 1(c) shows the occupation numbers of the neutron $i_{13/2}$ orbit and the proton $h_{9/2}$ orbit for the calculated states. The states with small deformation have small occupation number of neutron $i_{13/2}$ until ^{180}Hg and it increases from ^{180}Hg to ^{186}Hg . These states have small occupation number of proton $h_{9/2}$. The states with large deformation show the nearly half-filled neutron $i_{13/2}$ orbit and the more occupied proton $h_{9/2}$ orbit. Neutrons in the $i_{13/2}$ orbit and protons in the $h_{9/2}$ orbit contribute to quadrupole deformation and they gain binding energy from attractive monopole interaction between these orbits as well as quadrupole interaction. For even- N nucleus, pairing correlation in spherical state

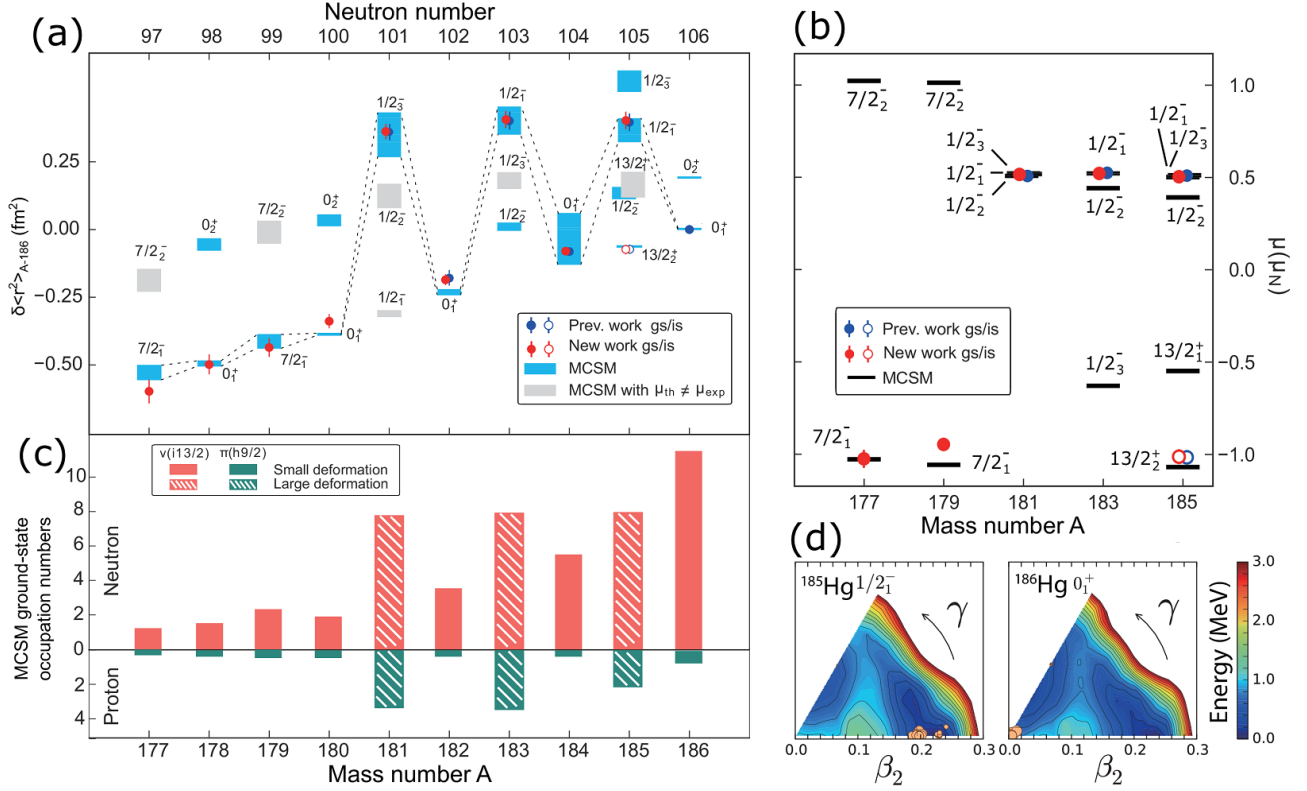


Figure 1. (a) The change in mean-square charge radius, $\delta\langle r^2 \rangle$, relative to that of the ground state of ^{186}Hg . The red points are experimental data [4]. The blue points refer to literature values from Ref. [3]. The shaded boxes indicate radii corresponding to the MCSM wave functions (see text for details). The grey areas show MCSM wave functions for which the calculated magnetic moment differs from the measured value. (b) Comparison of the calculated and experimental magnetic moments for different states in the odd-mass mercury isotopes. (c) The occupation numbers of the neutron $i_{13/2}$ orbit and the proton $h_{9/2}$ orbit for the states indicated by the blue connected areas in (a). (d) T-plots for two different states in $^{185,186}\text{Hg}$, with large and small deformations, respectively. Adapted from Fig. 2 of Ref. [4].

produces sufficient binding energy and the ground state becomes spherical. This is suppressed in odd- N nucleus by the unpaired neutron. The deformed ground states around ^{183}Hg can appear in the region where the neutron $i_{13/2}$ orbit is partially occupied. Thus, the mechanism of the shape staggering around ^{183}Hg can be explained.

This work has been supported in part by MEXT as ‘‘Priority Issue on post-K computer’’ (Elucidation of the Fundamental Laws and Evolution of the Universe), JICFuS, and the RIKEN-CNS joint research project on large-scale nuclear-structure calculations. The MCSM calculations were performed on the K computer at the RIKEN AICS (Project ID: hp160211, hp170230).

References

- [1] J. Bonn *et al.*, Phys. Lett. B **38**, 308 (1972).
- [2] T. K uhl *et al.*, Phys. Rev. Lett. **39**, 180 (1977).
- [3] G. Ulm *et al.*, Z. Phys. A **325**, 247 (1986).
- [4] B. A. Marsh *et al.*, Nature Physics **14**, 1163 (2018).
- [5] T. Otsuka, M. Honma, T. Mizusaki, N. Shimizu, and Y. Utsuno, Prog. Part. Nucl. Phys. **47**, 319 (2001).
- [6] N. Shimizu, T. Abe, Y. Tsunoda, Y. Utsuno, T. Yoshida, T. Mizusaki, M. Honma, and T. Otsuka, Prog. Theor. Exp. Phys. **2012**, 01A205 (2012).
- [7] N. Shimizu, T. Abe, M. Honma, T. Otsuka, T. Togashi, Y. Tsunoda, Y. Utsuno, and T. Yoshida, Phys. Scr. **92**, 063001 (2017).

Ground-state properties from the unitary-model-operator approach

T. Miyagi, T. Abe^a, M. Kohno^b, P. Navratil^c, R. Okamoto^d, T. Otsuka^{e,a,f,g}, N. Shimizu, and S. R. Stroberg^{c,h}

Center for Nuclear Study, The University of Tokyo

^a*Department of Physics, The University of Tokyo, Japan*

^b*Research Center for Nuclear Physics, Osaka University, Japan*

^c*TRIUMF, Canada*

^d*Senior Academy, Kyushu Institute of Technology, Japan*

^e*RIKEN, Nishina Center, Japan*

^f*National Superconducting Cyclotron Laboratory, Michigan State University, USA*

^g*Instituut voor Kern- en Stralingsfysica, KU Leuven, Belgium*

^h*Physics Department, Reed College, USA*

The nuclear saturation is one of the most fundamental properties observed in stable nuclei. The microscopic reproduction of this property is still challenging, however, because of the complexity of the nuclear force and of the quantum many-body problems. The developments in the chiral effective field theory (EFT) have provided the systematically improvable nuclear interactions. Combining with the recent progress in the ab initio many-body calculation methods, the medium-mass nuclei can be investigated. Due to the non-perturbative nature of the nuclear force, in most cases, it is impossible to apply directly the nuclear interactions to the many-body calculations. To perform the many-body calculations, we evolve the nuclear Hamiltonian with the similarity renormalization group (SRG) flow equation. With such nuclear interactions, recent ab initio results significantly underestimate the nuclear radii. As seen in no-core shell-model calculations for few-body systems [1], we should also evolve consistently other operators than the Hamiltonian. In this report, we demonstrate the effect of the SRG evolution on radius operator.

In this work, we employ the unitary-model-operator approach (UMOA) to solve the non-relativistic nuclear many-body Schrödinger equation: $H|\Psi_{g.s.}\rangle = E_{g.s.}|\Psi_{g.s.}\rangle$. Here, H is the Hamiltonian, $E_{g.s.}$ is the ground-state energy, and $|\Psi_{g.s.}\rangle$ is the ground-state wave function. In most cases, the many-body Schrödinger equation cannot be directly solved because of the current computational limitations. Instead, we construct the effective Hamiltonian with the unitary transformation,

$$\tilde{H} = U^\dagger H U,$$

such that \tilde{H} is decoupled with the one-particle-one-hole (1p1h) and two-particle-two-hole (2p2h) excitations. Here, U is defined by the product form of the exponential operators $U = e^{S^{(1)}} e^{S^{(2)}}$, where $S^{(1)}$ and $S^{(2)}$ are one- and two-body anti-hermitian correlation operators, respectively. The $S^{(1)}$ and $S^{(2)}$ are calculated with the Lee-Suzuki method. Since the 1p1h and 2p2h excitations are already decoupled with the uncorrelated Slater determinant $|\Phi\rangle = U^\dagger|\Psi_{g.s.}\rangle$, the ground-state energy $E_{g.s.}$ can be obtained approximately by

$$E_{g.s.} \approx \langle \Phi | \tilde{H} | \Phi \rangle.$$

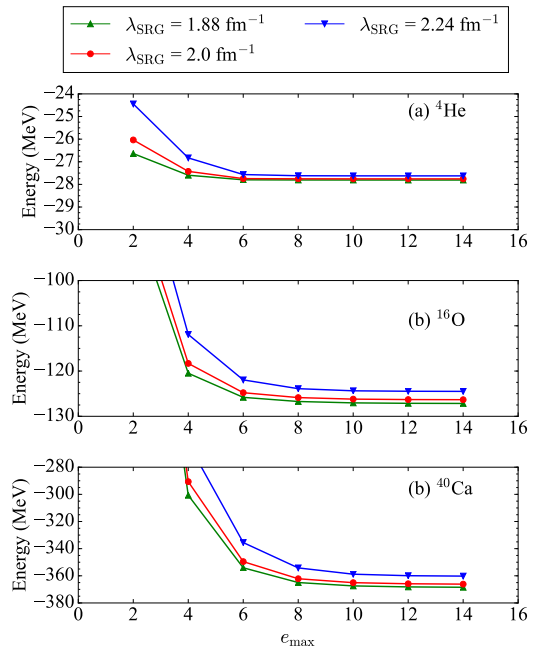


Figure 1. Ground-state energies for ${}^4\text{He}$ (a), ${}^{16}\text{O}$ (b), and ${}^{40}\text{Ca}$ (c) as functions of e_{\max} .

Note that \tilde{H} can be many-body operator. Then, we employ the cluster expansion and truncate the effect of the four- and many-body terms. (See Ref [2] for details.) As for the root-mean-squared radius, the effective operator $\tilde{r}^2 = U^\dagger r^2 U$ can be used. Using \tilde{r}^2 , the root-mean-squared radius can be evaluated as

$$r_{g.s.} \approx \sqrt{\langle \Phi | \tilde{r}^2 | \Phi \rangle}.$$

Similarly to the Hamiltonian, the unitary transformation induces the many-body terms. The radii examined here are calculated keeping up to two-body terms and does not include any contributions from three- and higher-body terms.

In this work, we use the next-to-next-to-next-to leading order ($N^3\text{LO}$) NN interaction by Entem and Machleidt [3] and local form of $N^2\text{LO}$ $3N$ interaction [4] from the chiral EFT. To suppress the strong short range repulsion of nuclear interaction, we employ the SRG technique and keep the terms up to three-body terms. To investigate the effect

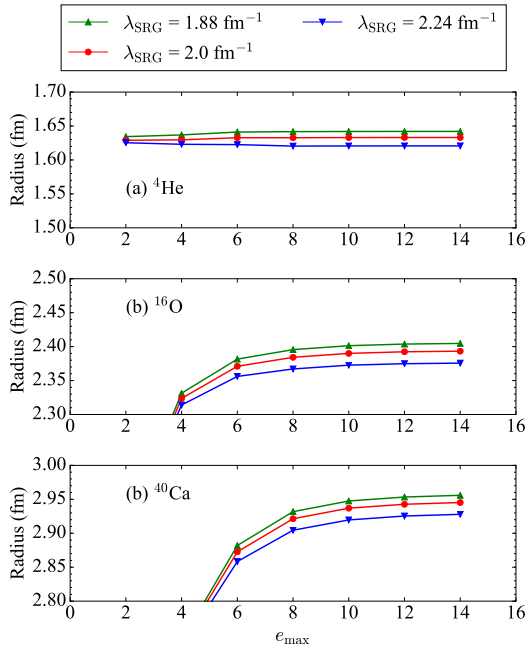


Figure 2. Charge radii calculated with the bare radius operator for ${}^4\text{He}$ (a), ${}^{16}\text{O}$ (b), and ${}^{40}\text{Ca}$ (c) as functions of e_{\max} .

of the SRG induced many-body terms, we use three SRG resolution scales; $\lambda_{\text{SRG}} = 1.88, 2.0,$ and 2.24 fm^{-1} where the evolved Hamiltonians are sufficiently soft to obtain the converged results. For the sake of controllable computations, the normal-ordered two-body (NO2B) approximation is used. The NO2B Hamiltonian is obtained through the Hartree-Fock (HF) calculations. For the three-body matrix element, we cannot store in the memory for all the matrix element needed in the calculations. In HF calculations, therefore, we consider the three-body matrix element only where $2n_1 + l_1 + 2n_2 + l_2 + 2n_3 + l_3 \leq e_{3\max}$ is satisfied. Here, $n_i (i = 1, 2, 3)$ is the single-particle radial quantum number and $l_i (i = 1, 2, 3)$ is the angular momentum. We observed that the ground-state energies for nuclei calculated in this work change less than 1% when we vary $e_{3\max}$ from 12 to 14. Therefore, the all results shown here are calculated at $e_{3\max} = 14$. The UMOA calculations are done in the model space defined by $e_{\max} = \max(2n_1 + l_1)$ [2].

In figure 1 and 2, the convergence property is shown for ground-state energies and charge radii for ${}^4\text{He}$, ${}^{16}\text{O}$, and ${}^{40}\text{Ca}$. As shown in the figure, converged results are found at $e_{\max} = 14$. Moreover, our ground-state energies agree with the recent ab initio results with the same interaction within a few percent. In figure 3, calculated charge radii with the bare, two-body SRG evolved, and three-body SRG evolved radius operators are shown. As found in the figure, the λ_{SRG} -dependence of radii reduces from bare to three-body evolved operators, which implies that the hierarchy for induced many-body terms is retained. Similar to the earlier no-core shell model calculation results for ${}^4\text{He}$ [1], the SRG evolution of operators shrinks the nucleon distribution. The SRG evolution of the radius operator which is consistent with the Hamiltonian evolution gives 1-2% changes for radii. Since the SRG evolution is introduced to suppress the

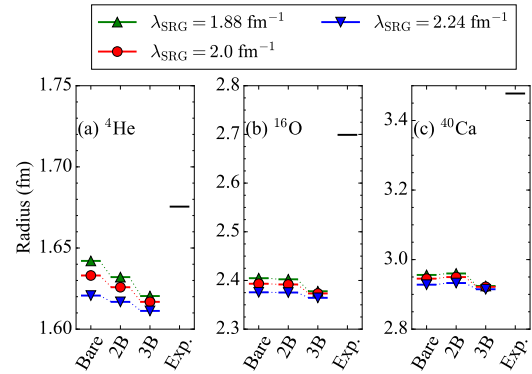


Figure 3. Charge radii evaluated with the expectation values of bare, two-body (2B) SRG evolved, and three-body (3B) SRG evolved mean-squared radius operator for ${}^4\text{He}$ (a), ${}^{16}\text{O}$ (b), and ${}^{40}\text{Ca}$ (c). All calculation results are obtained at $e_{\max} = 14$. The experimental data are taken from Ref. [5].

to the short-range contributions, this small change of radius is consistent with the long-range nature of the radius operator [1]. From these findings, it would not be sufficient to fill the gap between the calculated radii and data by only taking into consideration the induced many-body radius operators. The reproduction of radii is still an open question and it seems that the further insights for the NN and $3N$ interactions are indispensable.

References

- [1] M. D. Schuster, S. Quaglioni, C. W. Johnson, E. D. Jurgenson, and P. Navrátil, Phys. Rev. C 90 (2014), 011301.
- [2] T. Miyagi, T. Abe, R. Okamoto, and T. Otsuka, Phys. Rev. C 96 (2017), 054312.
- [3] D. R. Entem and R. Machleidt, Phys. Rev. C 68 (2003), 041001.
- [4] P. Navrátil, Few-Body Syst. 41 (2007), 117.
- [5] I. Angeli and K. P. Marinova, At. Data Nucl. Data Tables 99 (2013) 69.

A thermodynamical consideration on nuclear shell model

N. Tsunoda and N. Shimizu

Center for Nuclear Study, Graduate School of Science, University of Tokyo

Thermodynamics is one of the most general and widely used theories, not only in physics, but also in chemistry or biology. It can describe global properties of the system, for example, equation of state and its phase transitions as a phenomenology.

On the other hand, nuclei have various rich properties. Some are spherical, others are deformed, some are magic nuclei, others are not. Theories and experiments have always been clarifying new rich properties about stable and unstable nuclei, and will always be. Among those theories, the nuclear shell model is one of the most successful theories.

In this report, we will present a possible thermodynamic formulation of nuclear shell model. The aim of this work is to suggest a new perspective of nuclear shape or phase, using thermodynamic language, such as temperature, entropy and specific heat. We will first formulate the thermodynamics in nuclear shell model and then present the numerical example of the theory.

First of all, we will start from shell model Hamiltonian and its decomposition

$$H = \sum_i \epsilon_i a_i^\dagger a_i + \sum_{i,j,k,l} V_{ijkl} a_i^\dagger a_j^\dagger a_l a_k \quad (1)$$

$$= \sum_i \epsilon_i a_i^\dagger a_i + \sum_{i,j} \frac{\sum_J (2J+1) \langle ij|V|ij \rangle_{JT}}{\sum_J (2J+1)} + H_{multi} \quad (2)$$

$$= H_0 + H_{multi}. \quad (3)$$

The second term of the second line is called monopole interaction, which is angular averaged part of the twobody interaction between two orbits. In the third line, we combine the onebody part and monopole term as H_0 and the rest are defined as multipole term, H_{multi} . Since monopole interaction is diagonal for shell model basis, this do not change particle occupation numbers of the orbits. It is multipole term that makes the wavefunction complicated.

For the purpose of the thermodynamic formulation, we consider that H_0 configures the system and H_{multi} gives thermal fluctuation to the system. The Schrödinger equation reads,

$$H_0 |\Phi_i\rangle = E_i |\Phi_i\rangle, H \sum_i c_i |\Phi_i\rangle = E \sum_i c_i |\Phi_i\rangle. \quad (4)$$

If the system is in thermal equilibrium, the system will follow the canonical distribution with some specific value of temperature T . That is,

$$p_i = |c_i|^2 = \exp(-E_i/T)/Z, \quad Z = \sum_i \exp(-E_i/T) \quad (5)$$

where Z is partition function. Then, free energy and internal energy can be defined as

$$F = -\ln Z, \quad U = \sum_i E_i \exp(-E_i/T) \quad (6)$$

Entropy can be defined as an analogy to information entropy,

$$S = -\sum_i p_i \ln p_i \quad (7)$$

To know thermodynamical properties, we set up a series of Hamiltonian

$$H(\lambda) = H_0 + \lambda H_{multi} \quad (8)$$

with changing λ . In general, larger λ corresponds to higher temperature T . To explain implementation to the atomic nuclei, let us explain through an example.

Figure 1 shows the case of ^{68}Se . The original Hamiltonian is gxpfla interaction, which is one of the successful phenomenological interactions for pf -shell nuclei [1]. We set up λ dependent interaction according to Eq. (8). Calculations are done with changing λ from 0.20 to 1.60. Note that $\lambda = 1.00$ is exactly the original gxpfla interaction. Upper panels, probabilities $p_i = |c_i|^2$ are plotted with blue round points. X-axes are corresponding E_i value, in other words, expectation value of H_0 for each eigen state of H_0 . Points are fitted with exponential according to Eq. (5) with red line (note that the axes are log scale). Indeed, the probabilities are actually governed by the canonical distribution, approximately. Since the effective interaction is not originally designed for thermal system and the system is not sufficiently large to be a thermal system, canonical distribution is not perfect. Still, we can define the value of temperature T by the slope of this fitting. We observe that the slope is getting weaker as λ increases. In the limit of $\lambda \rightarrow 0$, the wavefunction will be $|\Psi\rangle = |\Phi_0\rangle$ (i.e. $|c_0|^2 = 1$), where $|\Phi_0\rangle$ is ground state of H_0 . As λ increases, they are excited to higher-energy states and end up with very small $|c_0|^2$, for example, when $\lambda = 1.60$, $c_0^2 \approx 10^{-4}$.

It is clear that nuclei are more spherical with smaller λ and lower temperature, because large proportion of the wavefunction is composed of $|\Phi_0\rangle$. In opposite, with large λ and high temperature nuclei tends to deformed because of the large fraction of the wavefunction is not just simple $|\Phi_0\rangle$. Obviously large λ corresponds to large entropy as well (see Eq. (7)).

Next we move on to the lower panels of Fig. 1, where the probability densities and state densities as functions of $\langle H_0 \rangle$ is shown. Red lines indicate the probability density of the calculated wavefunction and the blue lines are state densities of the system itself, just for the reference. Interestingly, we can observe a phase transition around $\lambda = 0.92$ 0.94.

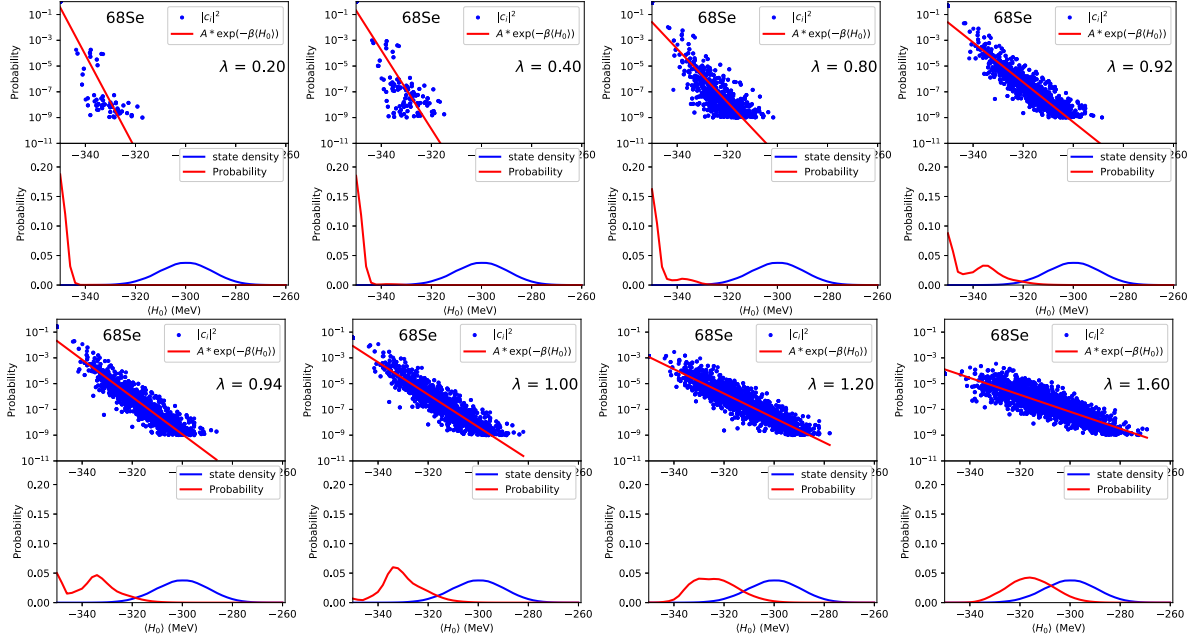


Figure 1. Thermodynamic plot of ^{68}Se . Calculations are repeated changing multipole strength λ from 0.20 to 1.60. For each λ , the upper figures show the $|c_i|^2$ values and the lower figures show probability density of the wavefunction and state density of the model space.

In the region $\lambda \leq 0.80$, the peak of the probability density is located on E_0 , in this case, around -350 MeV. On the other hand, when $\lambda \geq 1.00$, the peak is located around -320 MeV, which is apparently different from E_0 . Most interestingly, when $\lambda = 0.92$ and 0.94 , there are two different peaks on E_0 and around -320 MeV. This is the very point of phase transition, where two different phases are co-existing. In other words, this can be regarded as a critical phenomenon. Critical phenomena can be shown more clearly by defining specific heat for this system as

$$C = \frac{\partial U}{\partial T} \quad (9)$$

$$= \frac{\langle E^2 \rangle - \langle E \rangle^2}{T^2} = \frac{\sum_i p_i E_i^2 - (\sum_i p_i E_i)^2}{T^2}, \quad (10)$$

where we use the definition of Eq. (6). The numerator of Eq. (10) is fluctuation of the energy, and this quantity should diverge when an second order phase transition occurs. However, since the nuclei are not infinite systems any rigorous phase transition will not occur. Then we can consider the system as near-critical point when the specific heat is maximum. In the case of ^{68}Se , specific heat is maximum at $\lambda = 0.92$. If we assume original gxpfla interaction describe experimental situation well, the temperature of ^{68}Se is higher than critical temperature. Therefore, ^{68}Se is deformed.

Finally, we plotted the specific heat of various pf -shell nuclei as functions of temperature in Fig. 2. The strength and width of the peak depend on nuclei. As we discussed, there is no rigorous phase transition in all the nuclei, but the stronger and narrower peak corresponds to the sharper second order phase transition. For example, ^{56}Ni has the

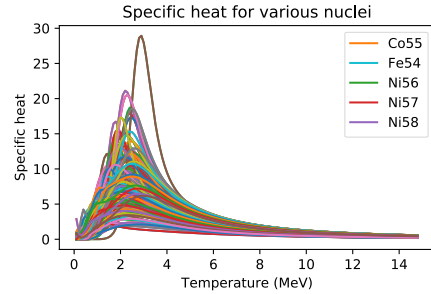


Figure 2. Specific heat of various nuclei as a function of temperature. Legend are shown only for several nuclei which have large peak.

strongest peak. This is clearly because of the shell structure, where neutron and proton $f_{7/2}$ orbit is fully occupied and known as doubly magic nuclei. For ^{56}Ni , critical point comes at $\lambda = 1.12$ and with original gxpfla interaction the temperature of ^{56}Ni is lower than critical temperature, which means ^{56}Ni is spherical. We can discuss the critical temperature and phase transition for other kind of nuclei as well on the same footing.

References

- [1] M. Honma et al., Phys. Rev. C **65**, 061301 (2002).

Other Activities

The 16th CNS International Summer School CNSSS17

T. Ichikawa, N. Imai, T. Gunji, H. Liang^{a,c}, S. Michimasa, Y. Mizoi^b, S. Ota, T. Otsuka^c, H. Sakai^a, H. Sakurai^{a,c}, N. Shimizu, S. Shimoura, H. Ueno^a, T. Uesaka^a, Y. Utsuno^d, K. Yako, and H. Yamaguchi.

Center for Nuclear Study, Graduate School of Science, University of Tokyo

^a*RIKEN Nishina Center*

^b*Faculty of Engineering, Osaka Electro-Communication University*

^c*Department of Physics, Univ. of Tokyo*

^d*Advanced Science Research Center, Japan Atomic Energy Agency*

The 16th CNS International Summer School (CNSSS17) was hosted by Center for Nuclear Study (CNS) from 23th to 29th in August, 2017. The school was supported by RIKEN Nishina Center and Asian Nuclear Physics Association (ANPhA). The venue was the Nishina hall in the Wako campus of RIKEN.

The summer school was the sixteenth one in the series which aimed at providing graduate students and postdocs with basic knowledge and perspectives of nuclear physics. It consisted of lectures by leading scientists in the fields of both experimental and theoretical nuclear physics. Each lecture started with an introductory talk from the fundamental point of view and ended with up-to-date topics in the relevant field.

The list of the lecturers and the title of lectures are following:

- Prof. Umesh Garg (Nortre Dome, USA), “High spin physics”
- Prof. Munetake Ichimura (RIKEN Nishina Center, Japan), “Nuclear direct reaction to Continuum”
- Prof. Tomotsugu Wakasa (Kyushu Univ. Japan), “Gamov-Teller and Spin-dipole responses and experimental methods for spin excitation”
- Prof. Robert Roth (TU Darmstadt, Germany), “*Ab initio* Nuclear Structure Theory”
- Dr. Aiko Takamine (RIKEN, Japan), “Overview of RI Beam Facility”
- Dr. Bhanu Pratap Das (Titech, Japan), “Relativistic Effects in Superheavy Elements”
- Dr. Naofumi Tsunoda (CNS, Japan), “Effective interaction of nuclei”

Seven lecturers and ninety participants joined the school from eight countries. Two lectures and twenty participants came from foreign institutes. The time of each class was 50 minutes. There was 10 minutes break between the class to encourage the participants to communicate the lecturers. They talked each other in free discussion times such as breaks, lunch times, welcome and poster session in a relaxed atmosphere. Figure 1 presents a group photo of all the participants with the lecturers.



Figure 1. A group photos of the participants of CNSSS17 with the lecturers.

As traditional, there were four “Young Scientist Sessions”, where twenty-six oral presentations and nine poster presentation were given by graduate students and postdocs.

We have launched the CNSSS young scientist awards (CNSSSYS awards) for the good presentations selected from the young scientist sessions from this school. The winners of the first CNSSSYS award were;

- Mr. Toshitaka Niwase (Kyushu Univ.) “High-precision mass measurements of short-lived nuclei with MRTOF-GARIS-II”
- Mr. Yasuhiro Ueno (Univ. of Tokyo) “Precision Test of Bound-State QED via the Spectroscopy of Muonium Hyperfine Structure”
- Dr. Takayuki Miyagi (CNS, Univ. of Tokyo) “Unitary-model-operator-approach calculations with the chiral NN+3N forces”
- Dr. Xiaoli Sun (Inst. of High Energy Phy.) “First generation method of PSF-basaed system matrix for PET Reconstruction”
- Mr. Wilmar Rodriguez (National University of Colombia) “The use of Hk-EOS technique to study the nuclear continuum”.

The certificate of the awards were presented to them as demonstrated in Fig. 2.

The best presenter among them, Mr. Yasuhiro Ueno, was also awarded the first APPS-DNP/ANPhA prize for young



Figure 2. The winners of the first CNSSS young scientist awards. From left, Prof. Shimoura (school master), Dr. Sun, Mr. Niwase, Dr. Miyagi, Mr. Rodrigues, Mr. Ueno and Dr. Motobayashi (vice chair of ANPhA).



Figure 3. The ceremony of the AAPPS-DNP/ANPhA prize. Mr. Yasuhiro Ueno received the certificate of the AAPP-S-DNP/ANPhA prize for the young physicist from the vice chair of the ANPhA, Dr. Tohru Motobayashi.

physicist, which was sponsored by AAPPS-DNP/ANPhA. He received the certificate as well as the prize money as prestend in Fig. 3.

The organizers appreciate Nishina Center for providing the venue as well as the accommodations. We are grateful to supports from ANPhA. We thank administration staffs of the CNS for their helpful supports. We also thank graduate students and postdocs in the CNS for their dedicated efforts. Finally we acknowledge all the lectures and participants for their contributions to the CNSSS17.

Laboratory Exercise for Undergraduate Students

S. Ota, M. Niikura^a, R. Tsunoda, T. Koiwai^a, K. Yako, H. Sakurai^{a,b} and S. Shimoura

Center for Nuclear Study, Graduate School of Science, University of Tokyo

^a*Department of Physics, University of Tokyo*

^b*RIKEN Nishina Center*

Nuclear scattering experiments were performed as a laboratory exercise for undergraduate students of the University of Tokyo. This program was aiming at providing undergraduate students with an opportunity to learn how to study subatomic physics by using an ion beam from an accelerator. In 2017, 32 students attended this program.

The four beam times were scheduled in the second semester for third-year students, and 8 students participated in each beam time. The experiments were performed at the RIBF using a 26-MeV alpha beam accelerated by the AVF cyclotron. The alpha beam extracted from the AVF cyclotron was transported to the E7B beam line in the E7 experimental hall. The scattering chamber has two separate target ports which enable us to perform two independent experiments without opening the chamber during the beam time. In each beam time, the students were divided into two groups and took one of the following two subjects:

- (1) Measurement of elastic scattering of incident alpha particle with ^{197}Au , to learn how to determine nuclear size.
- (2) Measurement of gamma rays emitted from the cascade decay of highly excited ^{154}Gd and ^{184}Os , to learn the nuclear deformation.

Before the experiment, the students took a course on the basic handling of the semiconductor detectors and electronic circuits at the Hongo campus, and attended a radiation safety lecture at RIKEN. They also joined a tour to the RI beam factory at RIKEN.

In the $\alpha+^{197}\text{Au}$ measurement, α particles scattered with the Au target with a thickness of $1\ \mu\text{m}$ were detected using a silicon PIN-diode located 15-cm away from the target. A collimator with a diameter of 6 mm was attached on the silicon detector. The energy spectrum of the scattered α particles was recorded by a multi-channel analyzer (MCA) system. The beam was stopped by a Faraday cup located downstream of the scattering chamber. The cross section for the alpha elastic scattering was measured in the angular range of $\theta_{\text{lab}} = 20\text{--}150^\circ$.

The measured cross section was compared with the calculated cross section of the Rutherford scattering. The cross section was also analyzed by the potential model calculation, and the radius of the ^{197}Au nucleus was discussed. Some students obtained the radius of ~ 10 fm by using a classical model where the trajectory of the α particle in the nuclear potential is obtained using the Runge-Kutta method. Others tried to understand the scattering process by calculating the angular distribution using the distorted wave Born approximation method with a Coulomb wave function and

a realistic nuclear potential.

In the measurement of gamma rays, excited states in ^{154}Gd and ^{184}Os nuclei were populated by the $^{152}\text{Sm}(\alpha,2n)$ and $^{182}\text{W}(\alpha,2n)$ reactions, respectively. The gamma rays emitted from the cascade decay of the rotational bands were measured by a high-purity germanium detector located 30-cm away from the target. The energy of the gamma ray were recorded by the MCA system. The gain and the efficiency of the detector system had been calibrated using standard gamma-ray sources of ^{22}Na , ^{60}Co , ^{133}Ba , and ^{137}Cs . The gamma rays from the 10^+ and 8^+ states in ^{154}Gd and ^{184}Os , respectively, were successfully identified. Based on the energies of the gamma rays, the moment of inertia and the deformation parameters of the excited states were discussed by using a classical rigid rotor model and a irrotational fluid model. The students found that the reality lies between the two extreme models. The initial population among the levels in the rotational band was also discussed by taking the effect of the internal conversion into account.

It was the first time for most of the students to use large experimental equipments. They learned basic things about the experimental nuclear physics and how to extract physics from the data. We believe this program was very impressive for the students. The authors would like to thank Dr. Y. Uwamino, the CNS accelerator group, and the RIBF cyclotron crew for their helpful effort in the present program.

Appendices

**Symposium, Workshop, Seminar, PAC and
External Review**

CNS Reports

Publication List

Talks and Presentations

Personnel

Symposium, Workshop, Seminar, Colloquium, and PAC

A. Symposium and Workshop

- (1) Ito International Research Center (IIRC) symposium
“ Perspectives of the physics of nuclear structure ” , Nov. 1–4, 2017, the University of Tokyo, Hongo, Japan
- (2) ImPACT-OEDO Workshop
July 13–14, 2017, RIKEN, Japan

B. CNS Seminar

- (1) Jongwon Hwang (CNS): “Structure of ^{19}C via one-neutron knockout from ^{20}C ”, Apr. 26, 2017, Nishina Hall, RIKEN, Japan
- (2) Kouichi Haigino (Tohoku U.): “重イオン核融合反応：多自由度系における量子トンネル現象と超重元素の合成”, Jun. 20, 2017, Nishina Hall, RIKEN, Japan
- (3) Toshimi Suda (Tohoku U.): “科研費について (RIKEN-CNS-WASC-Special Seminar)”, Sep. 19, 2017, RIBF Conference Hall, RIKEN, Japan
- (4) Toshitaka Kajino (NAO): “Impact of Neutron Star Mergers vs. Supernovae on Explosive Nucleosynthesis and Neutrino Physics”, Feb. 7, 2018, Nishina Hall, RIKEN, Japan
- (5) Masayuki Matsuo (Niigata U.): “Di-neutron correlation, pairing collectivity and pair transfer”, Mar. 20, 2018, Nishina Hall, RIKEN, Japan

C. Program Advisory Committee for Nuclear-Physics Experiments at RI Beam Factory

- (1) The 18th NP-PAC meeting
Date: December 7-9, 2017
Place: RIBF Conference Hall on the 2nd floor of the RIBF Building

CNS Reports

#96 “CNS Annual Report 2016”

Edited by T. Gunji, and Y. Kishi March, 2018

Publication List

A. Original Papers

- (1) S. Kawase, T. Uesaka, T.L. Tang, D. Beaumel, M. Dozono, T. Fukunaga, T. Fujii, N. Fukuda, A. Galindo-Uribarri, S. Hwang, N. Inabe, T. Kawabata, T. Kawahara, W. Kim, K. Kisamori, M. Kobayashi, T. Kubo, Y. Kubota, K. Kusaka, C. Lee, Y. Maeda, H. Matsubara, S. Michimasa, H. Miya, T. Noro, Y. Nozawa, A. Obertelli, K. Ogata, S. Ota, E. Padilla-Rodal, S. Sakaguchi, H. Sakai, M. Sasano, S. Shimoura, S. Stepanyan, H. Suzuki, T. Suzuki, M. Takaki, H. Takeda, A. Tamii, H. Tokieda, T. Wakasa, T. Wakui, K. Yako, J. Yasuda, Y. Yanagisawa, R. Yokoyama, K. Yoshida, K. Yoshida, J. Zenihiro, “Exclusive quasi-free proton knockout from oxygen isotopes at intermediate energies”, *Prog. Theor. Exp. Phys.* 2018, 021D01 (2018).
- (2) D. Steppenbeck, S. Takeuchi, N. Aoi, P. Doornenbal, M. Matsushita, H. Wang, H. Baba, S. Go, J.D. Holt, J. Lee, K. Matsui, S. Michimasa, T. Motobayashi, D. Nishimura, T. Otsuka, H. Sakurai, Y. Shiga, P.-A. Soderstrom, S. R. Stroberg, T. Sumikama, R. Taniuchi, J.A. Tostevin, Y. Utsuno, J. J. Valiente-Dobon, K. Yoneda, “Structure of ^{55}Sc and development of the $N=34$ subshell closure”, *Phys. Rev. C* **96**, 064310 (2017).
- (3) S. Momiyama, P. Doornenbal, H. Scheit, S. Takeuchi, M. Niikura, N. Aoi, K. Li, M. Matsushita, D. Steppenbeck, H. Wang, H. Baba, E. Ideguchi, M. Kimura, N. Kobayashi, Y. Kondo, J. Lee, S. Michimasa, T. Motobayashi, N. Shimizu, M. Takechi, Y. Togano, Y. Utsuno, K. Yoneda, H. Sakurai, “In-beam gamma-ray spectroscopy of ^{35}Mg via knockout reactions at intermediate energies”, *Phys. Rev. C* **96**, 034328 (2017).
- (4) Z. Patel, P. M. Walker, Z. Podolyak, P. H. Regan, T. A. Berry, P.-A. Soderstrom, H. Watanabe, E. Ideguchi, G. S. Simpson, S. Nishimura, Q. Wu, F. R. Xu, F. Browne, P. Doornenbal, G. Lorusso, S. Rice, L. Sinclair, T. Sumikama, J. Wu, Z. Y. Xu, N. Aoi, H. Baba, F. L. Bello Garrote, G. Benzoni, R. Daido, Z. Dombradi, Y. Fang, N. Fukuda, G. Gey, S. Go, A. Gottardo, N. Inabe, T. Isobe, D. Kameda, K. Kobayashi, M. Kobayashi, T. Komatsubara, I. Kojouharov, T. Kubo, N. Kurz, I. Kuti, Z. Li, M. Matsushita, S. Michimasa, C. B. Moon, H. Nishibata, I. Nishizuka, A. Odahara, E. Sahin, H. Sakurai, H. Schaffner, H. Suzuki, H. Takeda, M. Tanaka, J. Taprogge, Zs. Vajta, A. Yagi, R. Yokoyama, “Isomer-delayed gamma-ray spectroscopy of $A=159-164$ midshell nuclei and the variation of K -forbidden $E1$ transition hindrance factors”, *Phys. Rev. C* **96**, 034305 (2017).
- (5) S. Kawase, K. Nakano, Y. Watanabe, H. Wang, H. Otsu, H. Sakurai, D. S. Ahn, M. Aikawa, T. Ando, S. Araki, S. Chen, N. Chiga, P. Doornenbal, N. Fukuda, T. Isobe, S. Kawakami, T. Kin, Y. Kondo, S. Koyama, S. Kubono, Y. Maeda, A. Makinaga, M. Matsushita, T. Matsuzaki, S. Michimasa, S. Momiyama, S. Nagamine, T. Nakamura, M. Niikura, T. Ozaki, A. Saito, T. Saito, Y. Shiga, M. Shikata, Y. Shimizu, S. Shimoura, T. Sumikama, P. A. Soderstrom, H. Suzuki, H. Takeda, S. Takeuchi, R. Taniuchi, Y. Togano, J. Tsubota, M. Uesaka, Y. Watanabe, K. Wimmer, T. Yamamoto, K. Yoshida, “Study of proton- and deuteron-induced spallation reactions on the long-lived fission product ^{93}Zr at 105 MeV/nucleon in inverse kinematics”, *Prog. Theor. Exp. Phys.* 2018, 093D03 (2017).
- (6) N. Nakatsuka, H. Baba, T. Aumann, R. Avigo, S.R. Banerjee, A. Bracco, C. Caesar, F. Camera, S. Ceruti, S. Chen, V. Derya, P. Doornenbal, A. Giaz, A. Horvat, K. Ieki, T. Inakura, N. Imai, T. Kawabata, N. Kobayashi, Y. Kondo, S. Koyama, M. Kurata-Nishimura, S. Masuoka, M. Matsushita, S. Michimasa, B. Million, T. Motobayashi, T. Murakami, T. Nakamura, T. Ohnishi, H.J. Ong, S. Ota, H. Otsu, T. Ozaki, A. Saito, H. Sakurai, H. Scheit, F. Schindler, P. Schrock, Y. Shiga, M. Shikata, S. Shimoura, D. Steppenbeck, T. Sumikama, I. Syndikus, H. Takeda, S. Takeuchi, A. Tamii, R. Taniuchi, Y. Togano, J. Tscheuschner, J. Tsubota, H. Wang, O. Wieland, K. Wimmer, Y. Yamaguchi, K. Yoneda, J. Zenihiro, “Observation of isoscalar and isovector dipole excitations in neutron-rich ^{200}O ”, *Phys. Lett. B* **768**, 387–392 (2017).
- (7) P. Doornenbal, H. Scheit, S. Takeuchi, Y. Utsuno, N. Aoi, K. Li, M. Matsushita, D. Steppenbeck, H. Wang, H. Baba, E. Ideguchi, N. Kobayashi, Y. Kondo, J. Lee, S. Michimasa, T. Motobayashi, T. Otsuka, H. Sakurai, M. Takechi, Y. Togano, K. Yoneda, “Low- Z shore of the “island of inversion” and the reduced neutron magicity toward ^{28}O ”, *Phys. Rev. C* **95**, 041301 (2017).
- (8) H. N. Liu, J. Lee, R. Doornenbal, H. Scheit, S. Takeuchi, N. Aoi, K. Li, M. Matsushita, D. Steppenbeck, H. Wang, H. Baba, E. Ideguchi, N. Kobayashi, Y. Kondo, G. Lee, S. Michimasa, T. Motobayashi, A. Poves, H. Sakurai, M. Takechi, Y. Togano, J. A. Tostevin, Y. Utsuno, “Intruder configurations in the ground state of ^{30}Ne ”, *Phys. Lett. B* **767**, 58–62 (2017).

- (9) H. Wang, H. Otsu, H. Sakurai, D. Ahn, M. Aikawa, T. Ando, S. Araki, S. Chen, N. Chiga, P. Doornenbal, N. Fukuda, T. Isobe, S. Kawakami, S. Kawase, T. Kin, Y. Kondo, S. Koyama, S. Kubono, Y. Maeda, A. Makinaga, M. Matsushita, T. Matsuzaki, S. Michimasa, S. Momiyama, S. Nagamine, T. Nakamura, K. Nakano, M. Niikura, T. Ozaki, A. Saito, T. Saito, Y. Shiga, M. Shikata, Y. Shimizu, S. Shimoura, T. Sumikama, P. -A. Soderstrom, H. Suzuki, H. Takeda, S. Takeuchi, R. Taniuchi, Y. Togano, J. Tsubota, M. Uesaka, Y. Watanabe, Y. Watanabe, K. Wimmer, T. Yamamoto, K. Yoshida, “Spallation reaction study for the long-lived fission product ^{107}Pd ”, *Prog. Theor. Exp. Phys.* 2017, 021D01 (2017).
- (10) Hideshi Muto, Yukimitsu Ohshiro, Yasuteru Kotaka, Hidetoshi Yamaguchi, Yasuhiro Sakemi, Kiyoshi Kobayashi, Makoto Nishimura, Michihiro Oyaizu, Shigeru Kubono, Masayuki Kase, Toshiyuki Hattori Susumu Shimoura: “Note: An innovative method for $^{12}\text{C}^{4+}$ suppression in $^{18}\text{O}^{6+}$ beam production in an electron cyclotron resonance ion source”, *Rev. Sci. Instr.* **89**, 016103 (2018).
- (11) H. Suzuki, T. Kubo, N. Fukuda, N. Inabe, D. Kameda, H. Takeda, K. Yoshida, K. Kusaka, Y. Yanagisawa, M. Ohtake, H. Sato, Y. Shimizu, H. Baba, M. Kurokawa, K. Tanaka, O. B. Tarasov, D. Bazin, D. J. Morrissey, B. M. Sherrill, K. Ieki, D. Murai, N. Iwasa, A. Chiba, Y. Ohkoda, E. Ideguchi, S. Go, R. Yokoyama, T. Fujii, D. Nishimura, H. Nishibata, S. Momota, M. Lewitowicz, G. DeFrance, I. Celikovic, and K. Steiger: “Discovery of new isotopes $^{81,82}\text{Mo}$ and $^{85,86}\text{Ru}$ and a determination of the particle instability of ^{103}Sb ”, *Phys. Rev. C* **96**, 034604 (2017).
- (12) B. Moon, C.-B. Moon, A. Odahara, R. Lozeva, P.-A. Soderstrom, F. Browne, C. Yuan, A. Yagi, B. Hong, H. S. Jung, P. Lee, C. S. Lee, S. Nishimura, P. Doornenbal, G. Lorusso, T. Sumikama, H. Watanabe, I. Kojouharov, T. Isobe, H. Baba, H. Sakurai, R. Daido, Y. Fang, H. Nishibata, Z. Patel, S. Rice, L. Sinclair, J. Wu, Z. Y. Xu, R. Yokoyama, T. Kubo, N. Inabe, H. Suzuki, N. Fukuda, D. Kameda, H. Takeda, D. S. Ahn, Y. Shimizu, D. Murai, F. L. Bello Garrote, J. M. Daugas, F. Didierjean, E. Ideguchi, T. Ishigaki, S. Morimoto, M. Niikura, I. Nishizuka, T. Komatsubara Y. K. Kwon, K. Tshoo: “beta-decay scheme of ^{140}Te to ^{140}I : Suppression of Gamow-Teller transitions between the neutron $h^{9/2}$ and proton $h^{11/2}$ partner orbitals”, *Phys. Rev. C* **96**, 014325 (2017).
- (13) B. Moon, C.-B. Moon, P.-A. Soderstrom, A. Odahara, R. Lozeva, B. Hong, F. Browne, H. S. Jung, P. Lee, C. S. Lee, A. Yagi, C. Yuan, S. Nishimura, P. Doornenbal, G. Lorusso, T. Sumikama, H. Watanabe, I. Kojouharov, T. Isobe, H. Baba, H. Sakurai, R. Daido, Y. Fang, H. Nishibata, Z. Patel, S. Rice, L. Sinclair, J. Wu, Z. Y. Xu, R. Yokoyama, T. Kubo, N. Inabe, H. Suzuki, N. Fukuda, D. Kameda, H. Takeda, D. S. Ahn, Y. Shimizu, D. Murai F. L. Bello Garrote, J. M. Daugas, F. Didierjean E. Ideguchi, T. Ishigaki, S. Morimoto, M. Niikura, I. Nishizuka, T. Komatsubara, Y. K. Kwon, K. Tshoo: “Nuclear structure and beta-decay schemes for Te nuclides beyond $N = 82$ ”, *Phys. Rev. C* **95**, 044322 (2017).
- (14) K. Win, Y. Fujita, Y. Y. Oo, H. Fujita, Y. F. Niu, T. Adachi, G. P. A. Berg, G. Colo, H. Dohmann, M. Dozono, D. Frekers, E. -W. Grewe, K. Hatanaka, D. Ishikawa, R. Kehl, N. T. Khai, Y. Kalmykov, H. Matsubara, P. von Neumann-Cosel, T. Niizeki, T. Ruhe, Y. Shimbara, K. Suda, A. Tamii, J. Thies, and H. P. Yoshida: “High-resolution study of $T-z = +1 \rightarrow$ Gamow-Teller transitions in the $\text{Mg}^{26}(\text{He}^3, t)\text{Al}^{26}$ reaction”, *Phys. Rev. C* **96**, 064309 (2017).
- (15) K. Sekiguchi, H. Witala, T. Akieda, D. Eto, H. Kon, Y. Wada, A. Watanabe, S. Chebotaryov, M. Dozono, J. Golak, H. Kamada, S. Kawakami, Y. Kubota, Y. Maeda, K. Miki, E. Milman, A. Ohkura, H. Sakai, S. Sakaguchi, N. Sakamoto, M. Sasano, Y. Shindo, R. Skibinski, H. Suzuki, M. Tabata, T. Uesaka, T. Wakasa, K. Yako, T. Yamamoto, Y. Yanagisawa, and J. Yasuda: “Complete set of deuteron analyzing powers from dp elastic scattering at 190 MeV/nucleon”, *Phys. Rev. C* **96**, 064001 (2017).
- (16) T. Wakasa, J. Yasuda, M. Dozono, T. Fukunaga, S. Gotanda, K. Hatanaka, K. Ishibashi, S. Kimura, Y. Maeda, Y. Maeda, Y. Nishio, T. Noro, T. Nozoe, K. Ohnaka, S. Sakaguchi, Y. Sakemi, K. Sekiguchi, T. Taguchi, and Y. Wada: “Cross sections and analyzing powers for (\vec{p}, np) reactions of ^2H , ^6Li , and ^{12}C at 296 MeV”, *Phys. Rev. C* **96**, 014604 (2017).
- (17) J.W. Hwang, S. Kim, Y. Satou, N.A. Orr, Y. Kondo, T. Nakamura, J. Gibelin, N. L. Achouri, T. Aumann, H. Baba, F. Delaunay, P. Doornenbal, N. Fukuda, N. Inabe, T. Isobe, D. Kameda, D. Kanno, N. Kobayashi, T. Kobayashi, T. Kubo, S. Leblond, J. Lee, F. M. Marqués, R. Minakata, T. Motobayashi, D. Murai, T. Murakami, K. Muto, T. Nakashima, N. Nakatsuka, A. Navin, S. Nishi, S. Ogoshi, H. Otsu, H. Sato, Y. Shimizu, H. Suzuki, K. Takahashi, H. Takeda, S. Takeuchi, R. Tanaka, Y. Togano, A. G. Tuff, M. Vandebrouck, K. Yoneda, “Single-neutron knockout from ^{20}C and the structure of ^{19}C ”, *Phys. Lett. B* **769**, 503–508 (2017).

- (18) R. Yokoyama, S. Go, D. Kameda, T. Kubo, N. Inabe, N. Fukuda, H. Takeda, H. Suzuki, K. Yoshida, K. Kusaka, K. Tanaka, Y. Yanagisawa, M. Ohtake, H. Sato, Y. Shimizu, H. Baba, M. Kurokawa, D. Nishimura, T. Ohnishi, N. Iwasa, A. Chiba, T. Yamada, E. Ideguchi, T. Fujii, H. Nishibata, K. Ieki, D. Murai, S. Momota, Y. Sato, J. W. Hwang, S. Kim, O. B. Tarasov, D. J. Morrissey, B. M. Sherrill, G. Simpson, and C. R. Praharaj, “New K isomers in the neutron-rich N=100 isotones ^{162}Sm , ^{163}Eu , and ^{164}Gd ”, *Phys. Rev. C* **95**, 034313 (2017).
- (19) N. Fukuda, T. Kubo, D. Kameda, N. Inabe, H. Suzuki, Y. Shimizu, H. Takeda, K. Kusaka, Y. Yanagisawa, M. Ohtake, K. Tanaka, K. Yoshida, H. Sato, H. Baba, M. Kurokawa, T. Ohnishi, N. Iwasa, A. Chiba, T. Yamada, E. Ideguchi, S. Go, R. Yokoyama, T. Fujii, H. Nishibata, K. Ieki, D. Murai, S. Momota, D. Nishimura, Y. Sato, J. Hwang, S. Kim, Oleg B. Tarasov, D. J. Morrissey, and G. Simpson, “Identification of New Neutron-Rich Isotopes in the Rare-Earth Region Produced by 345 MeV/nucleon ^{238}U ”, *J. Phys. Soc. Jpn.* **87** 014202 (2017).
- (20) J.C. Zamora et al., “Nuclear-matter radius studies from $^{58}\text{Ni}(\alpha, \alpha)$ experiments at the GSI Experimental Storage Ring with the EXL facility”, *Phys. Rev. C* **96**, 034617 (2017).
- (21) K. Sekiguchi et al., “Complete set of deuteron analyzing powers from dp elastic scattering at 190 MeV/nucleon”, *Phys. Rev. C* **96**, 064001 (2017).
- (22) L. Stuhl, M. Sasano, K. Yako, J. Yasuda, T. Uesaka, “PANDORA, a large volume low-energy neutron detector with real-time neutron–gamma discrimination”, *Nucl. Instr. and Meth. in Phys. Res. A* **864**, 164–171 (2017).
- (23) S. Acharya et al. [ALICE Collaboration], “First measurement of Ξ_c^0 production in pp collisions at $\sqrt{s} = 7$ TeV”, *Phys. Lett. B* **781**, 8 (2018).
- (24) S. Acharya et al. [ALICE Collaboration], “Measurement of Z^0 -boson production at large rapidities in Pb-Pb collisions at $\sqrt{s_{NN}}=5.02$ TeV”, *Phys. Lett. B* **780**, 372 (2018).
- (25) S. Acharya et al. [ALICE Collaboration], “Longitudinal asymmetry and its effect on pseudorapidity distributions in Pb-Pb collisions at $\sqrt{s_{NN}} = 2.76$ TeV”, *Phys. Lett. B* **781**, 20 (2018).
- (26) S. Acharya et al. [ALICE Collaboration], “Production of ^4He and $^4\bar{\text{He}}$ in Pb-Pb collisions at $\sqrt{s_{NN}} = 2.76$ TeV at the LHC”, *Nucl. Phys. A* **971**, 1 (2018).
- (27) S. Acharya et al. [ALICE Collaboration], “Production of deuterons, tritons, ^3He nuclei and their antinuclei in pp collisions at $\sqrt{s} = 0.9, 2.76$ and 7 TeV”, *Phys. Rev. C* **97**, no. 2, 024615 (2018).
- (28) S. Acharya et al. [ALICE Collaboration], “Search for collectivity with azimuthal J/ψ -hadron correlations in high multiplicity p-Pb collisions at $\sqrt{s_{NN}} = 5.02$ and 8.16 TeV”, *Phys. Lett. B* **780**, 7 (2018).
- (29) S. Acharya et al. [ALICE Collaboration], “ J/ψ elliptic flow in Pb-Pb collisions at $\sqrt{s_{NN}} = 5.02$ TeV”, *Phys. Rev. Lett.* **119**, no. 24, 242301 (2017).
- (30) S. Acharya et al. [ALICE Collaboration], “Constraining the magnitude of the Chiral Magnetic Effect with Event Shape Engineering in Pb-Pb collisions at $\sqrt{s_{NN}} = 2.76$ TeV”, *Phys. Lett. B* **777**, 151 (2018).
- (31) S. Acharya et al. [ALICE Collaboration], “The ALICE Transition Radiation Detector: construction, operation, and performance”, *Nucl. Instrum. Meth. A* **881**, 88 (2018).
- (32) S. Acharya et al. [ALICE Collaboration], “Kaon femtoscopy in Pb-Pb collisions at $\sqrt{s_{NN}} = 2.76$ TeV”, *Phys. Rev. C* **96**, no. 6, 064613 (2017).
- (33) S. Acharya et al. [ALICE Collaboration], “Systematic studies of correlations between different order flow harmonics in Pb-Pb collisions at $\sqrt{s_{NN}} = 2.76$ TeV”, *Phys. Rev. C* **97**, no. 2, 024906 (2018).
- (34) S. Acharya et al. [ALICE Collaboration], “ π^0 and η meson production in proton-proton collisions at $\sqrt{s} = 8$ TeV”, *Eur. Phys. J. C* **78**, no. 3, 263 (2018).
- (35) C. Aidala et al. [PHENIX Collaboration], “Measurements of azimuthal anisotropy and charged-particle multiplicity in d+Au collisions at $\sqrt{s_{NN}} = 200, 62.4, 39,$ and 19.6 GeV”, *Phys. Rev. C* **96**, no. 6, 064905 (2017).
- (36) S. Acharya et al. [ALICE Collaboration], “Charged-particle multiplicity distributions over a wide pseudorapidity range in proton-proton collisions at $\sqrt{s} = 0.9, 7,$ and 8 TeV”, *Eur. Phys. J. C* **77**, no. 12, 852 (2017).

- (37) S. Acharya et al. [ALICE Collaboration], “Measurement of deuteron spectra and elliptic flow in Pb–Pb collisions at $\sqrt{s_{NN}} = 2.76$ TeV at the LHC,” *Eur. Phys. J. C* **77**, no. 10, 658 (2017).
- (38) C. Aidala et al. [PHENIX Collaboration], “Measurements of Multiparticle Correlations in d+Au Collisions at 200, 62.4, 39, and 19.6 GeV and p+Au Collisions at 200 GeV and Implications for Collective Behavior,” *Phys. Rev. Lett.* **120**, no. 6, 062302 (2018).
- (39) S. Acharya et al. [ALICE Collaboration], “Searches for transverse momentum dependent flow vector fluctuations in Pb-Pb and p-Pb collisions at the LHC,” *JHEP* **1709**, 032 (2017).
- (40) S. Acharya et al. [ALICE Collaboration], “D-meson azimuthal anisotropy in midcentral Pb-Pb collisions at $\sqrt{s_{NN}} = 5.02$ TeV,” *Phys. Rev. Lett.* **120**, no. 10, 102301 (2018).
- (41) S. Acharya et al. [ALICE Collaboration], “Measuring $K_S^0 K^\pm$ interactions using Pb-Pb collisions at $\sqrt{s_{NN}} = 2.76$ TeV,” *Phys. Lett. B* **774**, 64 (2017).
- (42) S. Acharya et al. [ALICE Collaboration], “Linear and non-linear flow modes in Pb-Pb collisions at $\sqrt{s_{NN}} = 2.76$ TeV,” *Phys. Lett. B* **773**, 68 (2017).
- (43) D. Adamová et al. [ALICE Collaboration], “ J/ψ production as a function of charged-particle pseudorapidity density in p-Pb collisions at $\sqrt{s_{NN}} = 5.02$ TeV,” *Phys. Lett. B* **776**, 91 (2018).
- (44) C. Aidala et al. [PHENIX Collaboration], “Nuclear Dependence of the Transverse-Single-Spin Asymmetry for Forward Neutron Production in Polarized p+A Collisions at $\sqrt{s_{NN}} = 200$ GeV,” *Phys. Rev. Lett.* **120**, no. 2, 022001 (2018).
- (45) C. Aidala et al. [PHENIX Collaboration], “Cross section and transverse single-spin asymmetry of muons from open heavy-flavor decays in polarized p+p collisions at $\sqrt{s} = 200$ GeV,” *Phys. Rev. D* **95**, no. 11, 112001 (2017).
- (46) J. Adam et al. [ALICE Collaboration], “Flow dominance and factorization of transverse momentum correlations in Pb-Pb collisions at the LHC,” *Phys. Rev. Lett.* **118**, no. 16, 162302 (2017).
- (47) D. Adamova et al. [ALICE Collaboration], “Azimuthally differential pion femtoscopy in Pb-Pb collisions at $\sqrt{s_{NN}} = 2.76$ TeV,” *Phys. Rev. Lett.* **118**, no. 22, 222301 (2017).
- (48) S. Acharya et al. [ALICE Collaboration], “Production of muons from heavy-flavour hadron decays in p-Pb collisions at $\sqrt{s_{NN}} = 5.02$ TeV,” *Phys. Lett. B* **770**, 459 (2017).
- (49) C. Aidala et al. [PHENIX Collaboration], “B-meson production at forward and backward rapidity in p+p and Cu + Au collisions at $\sqrt{s_{NN}} = 200$ GeV,” *Phys. Rev. C* **96**, no. 6, 064901 (2017).
- (50) A. Adare et al. [PHENIX Collaboration], “Measurements of e^+e^- pairs from open heavy flavor in p+p and d+A collisions at $\sqrt{s_{NN}} = 200$ GeV,” *Phys. Rev. C* **96**, no. 2, 024907 (2017).
- (51) S. Acharya et al. [ALICE Collaboration], “Production of π^0 and η mesons up to high transverse momentum in pp collisions at 2.76 TeV,” *Eur. Phys. J. C* **77**, no. 5, 339 (2017).
- (52) S. Acharya et al. [ALICE Collaboration], “First measurement of jet mass in Pb–Pb and p–Pb collisions at the LHC,” *Phys. Lett. B* **776**, 249 (2018).
- (53) S. Acharya et al. [ALICE Collaboration], “Measurement of D-meson production at mid-rapidity in pp collisions at $\sqrt{s} = 7$ TeV,” *Eur. Phys. J. C* **77**, no. 8, 550 (2017).
- (54) S. Acharya et al. [ALICE Collaboration], “Energy dependence of forward-rapidity J/ψ and $\psi(2S)$ production in pp collisions at the LHC,” *Eur. Phys. J. C* **77**, no. 6, 392 (2017).
- (55) J. Adam et al. [ALICE Collaboration], “ $K^*(892)^0$ and $\phi(1020)$ meson production at high transverse momentum in pp and Pb-Pb collisions at $\sqrt{s_{NN}} = 2.76$ TeV,” *Phys. Rev. C* **95**, no. 6, 064606 (2017).
- (56) D. Adamova et al. [ALICE Collaboration], “Production of $\Sigma(1385)^\pm$ and $\Xi(1530)^0$ in p-Pb collisions at $\sqrt{s_{NN}} = 5.02$ TeV,” *Eur. Phys. J. C* **77**, no. 6, 389 (2017).
- (57) C. Aidala et al. [PHENIX Collaboration], “Measurements of $B \rightarrow J/\psi$ at forward rapidity in p+p collisions at $\sqrt{s} = 510$ GeV,” *Phys. Rev. D* **95**, no. 9, 092002 (2017).

- (58) J. Adam et al. [ALICE Collaboration], “Insight into particle production mechanisms via angular correlations of identified particles in pp collisions at $\sqrt{s}=7$ TeV,” *Eur. Phys. J. C* **77**, no. 8, 569 (2017).
- (59) J. Adam et al. [ALICE Collaboration], “Centrality dependence of the pseudorapidity density distribution for charged particles in Pb-Pb collisions at $\sqrt{s_{NN}}=5.02$ TeV,” *Phys. Lett. B* **772**, 567 (2017).
- (60) A. Adare et al. [PHENIX Collaboration], “Angular decay coefficients of J/ψ mesons at forward rapidity from p+p collisions at $\sqrt{s}=510$ GeV,” *Phys. Rev. D* **95**, 092003 (2017).
- (61) L. Yang, C.J. Lin, H.M. Jia, D.X. Wang, N.R. Ma, L.J. Sun, F. Yang, X.X. Xu, Z.D. Wu, H.Q. Zhang, and Z.H. Liu: “Is the Dispersion Relation Applicable for Exotic Nuclear Systems? The Abnormal Threshold Anomaly in the ${}^6\text{He} + {}^{209}\text{Bi}$ System”, *Phys. Rev. Lett.* **119**, 042503 (2017).
- (62) L. Yang, C.J. Lin, H.M. Jia, D.X. Wang, N.R. Ma, L.J. Sun, F. Yang, X.X. Xu, Z.D. Wu, H.Q. Zhang, and Z.H. Liu: “Abnormal behavior of the optical potential for the halo nuclear system ${}^6\text{He} + {}^{209}\text{Bi}$ ”, *Phys. Rev. C* **96**, 044615 (2017).
- (63) I. Indelicato, M. La Cognata, C. Spitaleri, V. Burjan, S. Cherubini, M. Gulino, S. Hayakawa, Z. Hons, V. Kroha, L. Lamia, M. Mazzocco, J. Mrazek, R. G. Pizzone, S. Romano, E. Strano, D. Torresi, A. Tumino, “New Improved Indirect Measurement of the ${}^{19}\text{F}(p, \alpha){}^{16}\text{O}$ Reaction at Energies of Astrophysical Relevance”, *Astrophysical Journal*, **845**, 19, 13 pages, (2017).
- (64) D. Kahl, H. Yamaguchi, S. Kubono, A.A. Chen, A. Parikh, D.N. Binh, J. Chen, S. Cherubini, N. N. Duy, T. Hashimoto S. Hayakawa, N. Iwasa, H. S. Jung, S. Kato, Y. K. Kwon S. Nishimura, S. Ota, K. Setoodehnia, T. Teranishi, H. Tokieda, T. Yamada, C. C. Yun and L. Y. Zhang, “First measurement of ${}^{30}\text{S} + \alpha$ resonant elastic scattering for the ${}^{30}\text{S}(\alpha, p)$ reaction rate”, *Phys. Rev. C* **97**, 015802 (2018).
- (65) T. Aoki, Y. Torii, B.K. Sahoo, B.P. Das, K. Harada, T. Hayamizu, K. Sakamoto, H. Kawamura, T. Inoue, A. Uchiyama, S. Ito, R. Yoshioka, K.S. Tanaka, M. Itoh, A. Hatakeyama, Y. Sakemi, “Parity-nonconserving interaction-induced light shifts in the ${}^7\text{S}^{1/2} - {}^6\text{D}^{3/2}$ transition of the ultracold ${}^{210}\text{Fr}$ atoms to probe new physics beyond the standard model”, *Appl. Phys.* **123** (2017) no.4, 120.
- (66) N. Shimizu, J. Menendez and K. Yako, “Double Gamow-Teller transition and its relation to neutrinoless decay”, *Phys. Rev. Lett.* **120**, 142502 (2018).
- (67) T. Mizusaki, M. Oi and N. Shimizu, “Why does sign problem occur in Onishi formula?”, *Phys. Lett. B* **779**, 237 (2018).
- (68) S. Ansari, J.-M. Régis, J. Jolie, N. Saed-Samii, N. Warr, W. Korten, M. Zielińska, M.-D. Salsac, A. Blanc, M. Jentschel, U. Köster, P. Mutti, T. Soldner, G. S. Simpson, F. Drouet, A. Vancraeynest, G. de France, E. Clément, O. Stezowski, C. A. Ur, W. Urban, P. H. Regan, Zs. Podolyák, C. Larijani, C. Townsley, R. Carroll, E. Wilson, H. Mach, L. M. Fraile, V. Pazyi, B. Olaizola, V. Vedia, A. M. Bruce, O. J. Roberts, J. F. Smith, M. Scheck, T. Kröll, A.-L. Hartig, A. Ignatov, S. Ilieva, S. Lalkovski, N. Mărginean, T. Otsuka, N. Shimizu, T. Togashi, and Y. Tsunoda, “Experimental study of lifetime and phase transition in neutron-rich ${}^{98,100,102}\text{Zr}$ ”, *Phys. Rev. C* **96**, 054323 (2017).
- (69) M. Queiser, A. Vogt, M. Seidlitz, P. Reiter, T. Togashi, N. Shimizu, Y. Utsuno, T. Otsuka, M. Honma, P. Petkov, K. Arnsward, R. Altenkirch, B. Birkenbach, A. Blazhev, T. Braunroth, A. Dewald, J. Eberth, C. Fransen, B. Fu, H. Hess, R. Hetzenegger, R. Hirsch, J. Jolie, V. Karayonchev, L. Kaya, L. Lewandowski, C. Müller-Gatermann, J.-M. Régis, D. Rosiak, D. Schneiders, B. Siebeck, T. Steinbach, K. Wolf, and K.-O. Zell, “Cross-shell excitations from the pf shell: Lifetime measurements in ${}^{61}\text{Zn}$ ”, *Phys. Rev. C* **96**, 044313 (2017).
- (70) S. Momiyama, P. Doornenbal, H. Scheit, S. Takeuchi, M. Niikura, N. Aoi, K. Li, M. Matsushita, D. Steppenbeck, H. Wang, H. Baba, E. Ideguchi, M. Kimura, N. Kobayashi, Y. Kondo, J. Lee, S. Michimasa, T. Motobayashi, N. Shimizu, M. Takechi, Y. Togano, Y. Utsuno, K. Yoneda, and H. Sakurai, “In-beam gamma-ray spectroscopy of ${}^{35}\text{Mg}$ via knockout reaction at intermediate energies”, *Phys. Rev. C* **96**, 034328 (2017).
- (71) J.-M. Régis, J. Jolie, N. Saed-Samii, N. Warr, M. Pfeiffer, A. Blanc, M. Jentschel, U. Köster, P. Mutti, T. Soldner, G. S. Simpson, F. Drouet, A. Vancraeynest, G. de France, E. Clément, O. Stezowski, C. A. Ur, W. Urban, P. H. Regan, Zs. Podolyák, C. Larijani, C. Townsley, R. Carroll, E. Wilson, L. M. Fraile, H. Mach, V. Pazyi, B. Olaizola, V. Vedia, A. M. Bruce, O. J. Roberts, J. F. Smith, M. Scheck, T. Kröll, A.-L. Hartig, A. Ignatov, S. Ilieva, S. Lalkovski, W. Korten, N. Mărginean, T. Otsuka, N. Shimizu, T. Togashi, and Y. Tsunoda, “Abrupt shape transition at neutron number $N=60$: $B(E2)$ values in ${}^{94,96,98}\text{Sr}$ from fast gamma-gamma timing”, *Phys. Rev. C* **95**, 054319 (2017).

- (72) N. Shimizu, T. Abe, M. Honma, T. Otsuka, T. Togashi, Y. Tsunoda, Y. Utsuno and T. Yoshida, “Monte Carlo shell model studies with massively parallel supercomputers”, *Phys. Scr.* **92**, 063001 (2017).
- (73) T. Miyagi, T. Abe, R. Okamoto, and T. Otsuka, “Introduction of the one-body correlation operator in the unitary-model-operator approach”, *Phys. Rev. C* **96**, 054312 (2017).
- (74) C.Wraith, X.F.Yang, L.Xie, C.Babcock, J.Bieroń, J.Billowes, M.L.Bissell, K.Blaum, B.Cheal, L.Filippin, R.F.Garcia Ruiz, W.Gins, L.K.Grob, G.Gaigalas, M.Godefroid, C.Gorges, H.Heylen, M.Honma, P.Jönsson, S.Kaufmann, M.Kowalska, J.Krämer, S.Malbrunot-Ettenauer, R.Neugart, G.Neyens, W.Nortershauser, F.Nowacki, T.Otsuka, J.Papuga, R.Sánchez, Y.Tsunoda, D.T.Yordanov, “Evolution of nuclear structure in neutron-rich odd-Zn isotopes and isomers”, *Phys. Lett. B* **771**, 385 (2017).
- (75) E. Sahin, F. L. Bello Garrote, Y. Tsunoda, T. Otsuka, G. de Angelis, A. Gorgen, M. Niikura, S. Nishimura, Z. Y. Xu, H. Baba, F. Browne, M.-C. Delattre, P. Doornenbal, S. Franchoo, G. Gey, K. Hadynska-Klek, T. Isobe, P. R. John, H. S. Jung, I. Kojouharov, T. Kubo, N. Kurz, Z. Li, G. Lorusso, I. Matea, K. Matsui, D. Mengoni, P. Morfouace, D. R. Napoli, F. Naqvi, H. Nishibata, A. Odahara, H. Sakurai, H. Schaffner, P.-A. Soderstrom, D. Sohler, I. G. Stefan, T. Sumikama, D. Suzuki, R. Taniuchi, J. Taprogge, Z. Vajta, H. Watanabe, V. Werner, J. Wu, A. Yagi, M. Yalcinkaya, and K. Yoshinaga, “Shell Evolution towards ^{78}Ni : Low-Lying States in ^{77}Cu ”, *Phys. Rev. Lett.* **118**, 242502 (2017).
- (76) R. P. de Groote, J. Billowes, C. L. Binnersley, M. L. Bissell, T. E. Cocolios, T. Day Goodacre, G. J. Farooq-Smith, D. V. Fedorov, K. T. Flanagan, S. Franchoo, R. F. Garcia Ruiz, Á. Koszorús, K. M. Lynch, G. Neyens, F. Nowacki, T. Otsuka, S. Rothe, H. H. Stroke, Y. Tsunoda, A. R. Vernon, K. D. A. Wendt, S. G. Wilkins, Z. Y. Xu, and X. F. Yang, “Dipole and quadrupole moments of 73-78Cu as a test of the robustness of the Z = 28 shell closure near ^{78}Ni ”, *Phys. Rev. C* **96**, 041302(R) (2017).
- (77) C. M. Shand, Z. Podolyák, M. Górska, P. Doornenbal, A. Obertelli, F. Nowacki, T. Otsuka, K. Sieja, J. A. Tostevin, Y. Tsunoda, G. Authelet, H. Baba, D. Calvet, A. Château, S. Chen, A. Corsi, A. Delbart, J. M. Gheller, A. Giganon, A. Gillibert, T. Isobe, V. Lapoux, M. Matsushita, S. Momiyama, T. Motobayashi, M. Niikura, H. Otsu, N. Paul, C. Péron, A. Peyaud, E. C. Pollacco, J.-Y. Rousse, H. Sakurai, C. Santamaria, M. Sasano, Y. Shiga, D. Steppenbeck, S. Takeuchi, R. Taniuchi, T. Uesaka, H. Wang, K. Yoneda, T. Ando, T. Arici, A. Blazhev, F. Browne, A. M. Bruce, R. J. Carroll, L. X. Chung, M. L. Cortés, M. Dewald, B. Ding, Z. Dombrádi, F. Flavigny, S. Franchoo, F. Giacoppo, A. Gottardo, K. Hadynska-Klek, A. Jungclaus, Z. Korkulu, S. Koyama, Y. Kubota, J. Lee, M. Lettmann, B. D. Linh, J. Liu, Z. Liu, C. Lizarazo, C. Louchart, R. Lozeva, K. Matsui, T. Miyazaki, K. Moschner, M. Nagamine, N. Nakatsuka, S. Nishimura, C. R. Nita, C. R. Nobs, L. Olivier, S. Ota, R. Orlandi, Z. Patel, P. H. Regan, M. Rudigier, E. Şahin, T. Saito, P.-A. Söderström, I. Stefan, T. Sumikama, D. Suzuki, Z. Vajta, V. Vaquero, V. Werner, K. Wimmer, J. Wu, and Z. Y. Xu, “Shell evolution beyond Z = 28 and N = 50: Spectroscopy of $^{81,82,83,84}\text{Zn}$ ”, *Phys. Lett. B* **773**, 492 (2017).
- (78) L. Olivier, S. Franchoo, M. Niikura, Z. Vajta, D. Sohler, P. Doornenbal, A. Obertelli, Y. Tsunoda, T. Otsuka, G. Authelet, H. Baba, D. Calvet, F. Château, A. Corsi, A. Delbart, J. M. Gheller, A. Gillibert, T. Isobe, V. Lapoux, M. Matsushita, S. Momiyama, T. Motobayashi, H. Otsu, C. Péron, A. Peyaud, E. C. Pollacco, J. Y. Roussé, H. Sakurai, C. Santamaria, M. Sasano, Y. Shiga, S. Takeuchi, R. Taniuchi, T. Uesaka, H. Wang, K. Yoneda, F. Browne, L. X. Chung, Z. Dombradi, F. Flavigny, F. Giacoppo, A. Gottardo, K. Hadynska-Klek, Z. Korkulu, S. Koyama, Y. Kubota, J. Lee, M. Lettmann, C. Louchart, R. Lozeva, K. Matsui, T. Miyazaki, S. Nishimura, K. Ogata, S. Ota, Z. Patel, E. Sahin, C. Shand, P. A. Söderström, I. Stefan, D. Steppenbeck, T. Sumikama, D. Suzuki, V. Werner, J. Wu, and Z. Xu, “Persistence of the Z = 28 Shell Gap Around ^{78}Ni : First Spectroscopy of ^{79}Cu ”, *Phys. Rev. Lett.* **119**, 192501 (2017).
- (79) S. Bottoni, S. Zhu, R. V. F. Janssens, M. P. Carpenter, Y. Tsunoda, T. Otsuka, A. O. Macchiavelli, D. Cline, C. Y. Wu, A. D. Ayangeakaa, B. Bucher, M. Q. Buckner, C. M. Campbell, C. J. Chiara, H. L. Crawford, M. Cromaz, H. M. David, P. Fallon, A. Gade, J. P. Greene, J. Harker, A. B. Hayes, C. R. Hoffman, B. P. Kay, A. Korichi, T. Lauritsen, J. Sethi, D. Seweryniak, W. B. Walters, D. Weisshaar, and A. Wiens, “Nucleon correlations and the structure of $^{71}_{30}\text{Zn}^{41}$ ”, *Phys. Lett. B* **775**, 271 (2017).
- (80) S. Yoshida, Y. Utsuno, N. Shimizu, and T. Otsuka, “Systematic shell-model study of β -decay properties and Gamow-Teller strength distributions in A ~ 40 neutron-rich nuclei”, *Phys. Rev. C* **97**, 054321 (2018).
- (81) B. Fernández-Domínguez, B. Pietras, W. N. Catford, N. A. Orr, M. Petri, M. Chartier, S. Paschalis, N. Patterson, J. S. Thomas, M. Caamaño, T. Otsuka, A. Poves, N. Tsunoda, N. L. Achouri, J.-C. Angélique, N. I. Ashwood, A.

Banu, B. Bastin, R. Borcea, J. Brown, F. Delaunay, S. Franchoo, M. Freer, L. Gaudefroy, S. Heil, M. Labiche, B. Laurent, R. C. Lemmon, A. O. Macchiavelli, F. Negoita, E. S. Paul, C. Rodríguez-Tajes, P. Roussel-Chomaz, M. Staniou, M. J. Taylor, L. Trache, and G. L. Wilson, “Re-examining the transition into the $N = 20$ island of inversion: Structure of ^{30}Mg ”, *Phys. Lett.* **B 779**, 124 (2018).

- (82) S. Leoni, B. Fornal, N. Mărginean, M. Sferrazza, Y. Tsunoda, T. Otsuka, G. Bocchi, F. C. L. Crespi, A. Bracco, S. Aydin, M. Boromiza, D. Bucurescu, N. Cieplicka-Oryńczak, C. Costache, S. Călinescu, N. Florea, D. G. Ghiță, T. Glodariu, A. Ionescu, Ł. W. Iskra, M. Krzysiek, R. Mărginean, C. Mihai, R. E. Mihai, A. Mitu, A. Negreț, C. R. Niță, A. Olăcel, A. Oprea, S. Pascu, P. Petkov, C. Petrone, G. Porzio, A. Șerban, C. Sotty, L. Stan, I. Știru, L. Stroe, R. Șuvăilă, S. Toma, A. Turturică, S. Ujeniuc, and C. A. Ur, “Multifaceted Quadruplet of Low-Lying Spin-Zero States in ^{66}Ni : Emergence of Shape Isomerism in Light Nuclei”, *Phys. Rev. Lett.* **118**, 162502 (2017)
- (83) J. Menéndez, “Neutrinoless $\beta\beta$ decay mediated by the exchange of light and heavy neutrinos: the role of nuclear structure correlations”, *J. Phys. G Nucl. Part. Phys.* **45**, 014003 (2018).
- (84) H. L. Crawford, A. O. Macchiavelli, P. Fallon, M. Albers, V. M. Bader, D. Bazin, C. M. Campbell, R. M. Clark, M. Cromaz, J. Dilling, A. Gade, A. Gallant, J. D. Holt, R. V. F. Janssens, R. Krücken, C. Langer, T. Lauritsen, I. Y. Lee, J. Menéndez, S. Noji, S. Paschalis, F. Recchia, J. Rissanen, A. Schwenk, M. Scott, J. Simonis, S. R. Stroberg, J. A. Tostevin, C. Walz, D. Weisshaar, A. Wiens, K. Wimmer, and S. Zhu, “Unexpected distribution of ν 1f7/2 strength in $\text{Ca}49$ ”, *Phys. Rev.* **C 95**, 064317 (2017).
- (85) P. Klos, A. Carbone, K. Hebeler, J. Menéndez, and A. Schwenk, “Uncertainties in constraining low-energy constants from ^3H β decay”, *Eur. Phys. J. A* **53**, 168 (2017).
- (86) M. Hoferichter, P. Klos, J. Menéndez, and A. Schwenk, “Improved Limits for Higgs-Portal Dark Matter from LHC Searches”, *Phys. Rev. Lett.* **119**, 181803 (2017).
- (87) H. Muto, Y. Ohshiro, Y. Kotaka, H. Yamaguchi, Y. Sakemi, K. Kobayashi, M. Nishimura, M. Oyaizu, S. Kubono, M. Kase, T. Hattori, and S. Shimoura, “An innovative method for $^{12}\text{C}^{4+}$ suppression in $^{18}\text{O}^{6+}$ beam production in an electron cyclotron resonance ion source”, *REVIEW OF SCIENTIFIC INSTRUMENTS* **89**, 016103 (2018)

B. Proceedings

- (1) T. Gunji [ALICE Collaboration], “Low mass dielectron measurements in pp, p-Pb, and Pb-Pb collisions with ALICE at the LHC”, *Nucl. Part. Phys. Proc.* 289-290, 181 (2017).
- (2) T. Otsuka, Y. Tsunoda, T. Togashi N. Shimizu and T. Abe, “Quantum self-organization and nuclear collectivities”, *Journal of Physics: Conf. Series* 966 (2018) 012027.
- (3) S. Michimasa, S. Ota, M. Dozono, M. Takaki, K. Kisamori, H. Miya, M. Kobayashi, Y. Kiyokawa, H. Baba, N. Fukuda, N. Inabe, S. Kawase, T. Kubo, Y. Kubota, C.S. Lee, M. Matsushita, H. Sakai, A. Stolz, H. Tokieda, T. Uesaka, K. Yako, Y. Yanagisawa, R. Yokoyama, K. Yoshida, S. Shimoura, “SHARAQ spectrometer: High-resolution spectroscopy using exotic beams and reactions”, *PoS (INPC2016)* 106, (2017).
- (4) D. Steppenbeck, S. Takeuchi, N. Aoi, P. Doornenbal, M. Matsushita, H. Wang, H. Baba, S. Go, J. Lee, K. Matsui, S. Michimasa, T. Motobayashi, D. Nishimura, T. Otsuka, H. Sakurai, Y. Shiga, P.-A. Soderstrom, T. Sumikama, R. Taniuchi, Y. Utsuno, J.J. Valiente-Dobon, K. Yoneda, “Low-lying Structures Of Exotic Sc Isotopes And The Evolution Of The $N = 34$ Subshell Closure”, *PoS (INPC2016)* 030, (2017).
- (5) R. Yokoyama, E. Ideguchi, G. Simpson, Mn. Tanaka, S. Nishimura, P. Doornenbal, P.-A. Soderstrom, G. Lorusso, Z.Y. Xu, J. Wu, T. Sumikama, N. Aoi, H. Baba, F. Bello, F. Browne, R. Daido, Y. Fang, N. Fukuda, G. Gey, S. Go, S. Inabe, T. Isobe, D. Kameda, K. Kobayashi, M. Kobayashi, T. Komatsubara, T. Kubo, I. Kuti, Z. Li, M. Matsushita, S. Michimasa, C. B. Moon, H. Nishibata, I. Nishizuka, A. Odahara, Z. Patel, S. Rice, E. Sahin, L. Sinclair, H. Suzuki, H. Takeda, J. Taprogge, Zs. Vajta, H. Watanabe, A. Yagi, “Role of Hexadecupole Deformation in the Shape Evolution of Neutron-rich Nd Isotopes”, *PoS (INPC2016)* 015, (2017).

- (6) Y. Togano, T. Nakamura, Y. Kondo, N. Kobayashi, R. Tanaka, R. Minakata, S. Ogoshi, S. Nishi, D. Kanno, T. Nakashima, J. Tsubota, A. T. Saito, J. A. Tostevin, N. A. Orr, J. Gibelin, F. Delaunay, F. M. Marques, N. L. Achouri, S. Leblond, Q. Deshayes, K. Yoneda, T. Motobayashi, H. Otsu, T. Isobe, H. Baba, H. Sato, Y. Shimizu, T. Kubo, N. Inabe, N. Fukuda, D. Kameda, H. Suzuki, H. Takeda, J. H. Lee, P. Doornenbal, S. Takeuchi, T. Kobayashi, K. Takahashi, K. Muto, T. Murakami, N. Nakatsuka, Y. Sato, S. Kim, J. Hwang, T. Aumann, D. Murai, A. Navin, A. G. Tuff, M. Vandebrouck, “Reaction Cross Section Of The Two-neutron Halo Nucleus ^{22}C At 235 MeV/nucleon”, PoS (INPC2016) 281, (2017).
- (7) H. Wang, H. Otsu, H. Sakurai, D. Ahn, N. Chiga, P. Doornenbal, N. Fukuda, T. Isobe, T. Kubo, S. Kubono, G. Lorusso, P. -A. Soderstrom, H. Suzuki, H. Takeda, Y. Watanabe, K. Yoshida, T. Matsuzaki, Y. Shimizu, T. Sumikama, M. Uesaka, S. Kawase, K. Nakano, Y. Watanabe, S. Araki, T. Kin, S. Takeuchi, Y. Togano, T. Nakamura, Y. Kondo, T. Ozaki, A. Saito, J. Tsubota, M. Aikawa, A. Makinaga, T. Ando, S. Koyama, S. Momiyama, S. Nagamine, M. Niikura, T. Saito, R. Taniuchi, K. Wimmer, S. Kawakami, Y. Maeda, T. Yamamoto, Y. Shiga, M. Matsushita, S. Michimasa, S. Shimoura, “Spallation reaction study for the long-lived fission products in nuclear waste: Cross section measurements for ^{137}Cs , ^{90}Sr and ^{107}Pd using inverse kinematics method”, Energy Procedia 131 127–132 (2017).
- (8) S. Kawase, Y. Watanabe, H. Wang, H. Otsu, H. Sakurai, S. Takeuchi, Y. Togano, T. Nakamura, Y. Maeda, D. S. Ahn, M. Aikawa, S. Araki, S. D. Chen, N. Chiga, P. Doornenbal, N. Fukuda, T. Ichihara, T. Isobe, S. Kawakami, T. Kin, Y. Kondo, S. Koyama, T. Kubo, S. Kubono, M. Kurokawa, A. Makinaga, M. Matsushita, T. Matsuzaki, S. Michimasa, S. Momiyama, S. Nagamine, K. Nakano, M. Niikura, T. Ozaki, A. Saito, T. Saito, Y. Shiga, M. Shikata, Y. Shimizu, S. Shimoura, T. Sumikama, P. -A. Soderstrom, H. Suzuki, H. Takeda, R. Taniuchi, J. Tsubota, Y. Watanabe, K. Wimmer, T. Yamamoto, K. Yoshida, “Cross section measurement of residues produced in proton- and deuteron-induced spallation reactions on ^{93}Zr at 105 MeV/u using the inverse kinematics method”, EPJ Web of Conferences 146, 03012 (2017).
- (9) K. Nakano, Y. Watanabe, S. Kawase, H. Wang, H. Otsu, H. Sakurai, S. Takeuchi, Y. Togano, T. Nakamura, Y. Maeda, D. S. Ahn, M. Aikawa, S. Araki, S. Chen, N. Chiga, P. Doornenbal, N. Fukuda, T. Ichihara, T. Isobe, S. Kawakami, T. Kin, Y. Kondo, S. Koyama, T. Kubo, S. Kubono, M. Kurokawa, A. Makinaga, M. Matsushita, T. Matsuzaki, S. Michimasa, S. Momiyama, S. Nagamine, M. Niikura, T. Ozaki, A. Saito, T. Saito, Y. Shiga, M. Shikata, Y. Shimizu, S. Shimoura, T. Sumikama, P.-A. Soderstrom, H. Suzuki, H. Takeda, R. Taniuchi, J. Tsubota, Y. Watanabe, K. Wimmer, T. Yamamoto, K. Yoshida, “Cross sections for nuclide production in proton- and deuteron-induced reactions on ^{93}Nb measured using the inverse kinematics method”, EPJ Web of Conferences 146, 11046 (2017).
- (10) K. Sekiguchi, Y. Wada, A. Watanabe, D. Eto, T. Akieda, H. Kon, K. Miki, N. Sakamoto, H. Sakai, M. Sasano, Y. Shimizu, H. Suzuki, T. Uesaka, Y. Yanagisawa, M. Dozono, S. Kawase, Y. Kubota, C. S. Lee, K. Yako, Y. Maeda, S. Kawakami, T. Yamamoto, S. Sakaguchi, T. Wakasa, J. Yasuda, A. Ohkura, Y. Shindo, M. Tabata, E. Milman, S. Chebotaryov, H. Okamura, and T. L. Tang: “Deuteron Analyzing Powers for dp Elastic Scattering at Intermediate Energies and Three-Nucleon Forces”, Few-Body Systems 58, 48 (2017).
- (11) H Yamaguchi, D Kahl, S Hayakawa, Y Sakaguchi, K Abe, T Nakao, T Suhara, N Iwasa, A Kim, D H Kim, S M Cha, M S Kwag, J H Lee, E J Lee, K Y Chae, Y Wakabayashi, N Imai, N Kitamura, P Lee, J Y Moon, K B Lee, C Akers, H S Jung, N N Duy, L H Khiem and C S Lee, “Study on a-cluster levels in non-4n nuclei using low-energy RI beams”, Journal of Physics: Conference Series, 863, 012025 (2017).
- (12) D. Kahl, H. Shimizu, H. Yamaguchi, K. Abe, O. Beliuskina, S. M. Cha, K. Y. Chae, A. A. Chen, Z. Ge, S. Hayakawa, N. Imai, N. Iwasa, A. Kim, D. H. Kim, M. J. Kim, S. Kubono, M. S. Kwag, J. Liang, J. Y. Moon, S. Nishimura, S. Oka, S. Y. Park, A. Psaltis, T. Teranishi, Y. Ueno and L. Yang, “Isomer beam elastic scattering: $^{26m}\text{Al}(p, p)$ for astrophysics”, EPJ Web Conf., 165, 01030 (2017).
- (13) H. Yamaguchi, D. Kahl, S. Hayakawa, L. Yang, H. Shimizu, Y. Sakaguchi, K. Abe, T. Nakao, T. Suhara, N. Iwasa, A. Kim, D.H. Kim, S.M. Cha, M.S. Kwag, J.H. Lee, E.J. Lee, K.Y. Chae, Y. Wakabayashi, N. Imai, N. Kitamura, P. Lee, J.Y. Moon, K.B. Lee, C. Akers, H.S. Jung, N.N. Duy, L.H. Khiem, C.S. Lee, T. Hashimoto, S. Kubono, T. Kawabata, T. Teranishi, Y.K. Kwon and D.N. Binh, “Nuclear astrophysics projects at the low-energy RI beam separator CRIB”, EPJ Web Conf., 165, 01056 (2017).
- (14) Umakanth Dammalapati, Ken-ichi Harada, Tomohiro Hayamizu, Kosuke Sakamoto, Ko Kato, Takahiro Aoki, Sako Ito, Takeshi Inoue, Aiko Uchiyama, Hirokazu Kawamura, Masatoshi Itoh, Takatoshi Aoki, Atsushi Hatakeyama, Yasuhiro Sakemi, “Francium: Tool for Fundamental Symmetry Investigations”, JPS Conf.Proc. 18 (2017) 011046.

- (15) M. Itoh, S. Ando, T. Aoki, H. Arikawa, S. Ezure, K. Harada, T. Hayamizu, T. Inoue, T. Ishikawa, K. Kato, H. Kawamura, Y. Sakemi, A. Uchiyama, “Measurement of the 3α decay from the Hoyle and the broad 10 MeV states in ^{12}C ”, J.Phys.Conf.Ser. 863 (2017) no.1, 012019.

C. Theses

- (1) H. Shimizu: “Toward the experimental evaluation of the contribution of the isomer to the Al-26 problem in ongoing nucleosynthesis in the galaxy”: Master Thesis, the University of Tokyo. March 2018.

D. Other Publications

Talks and Presentations

A. Conferences

- (1) Y.Sakemi (invited): “Fundamental physics with ultracold radioactive atoms and molecules”, MITP program “Low energy probes of new physics (LEPONP2017)”, 14-24, May, 2017, Mainz, Germany
- (2) Y.Sakemi (invited): “Fundamental physics with cooled radioactive atoms - possible extension of Fr-EDM”, 10th International Conference on Nuclear Physics at Storage Rings (STORI2017), 13-18 Nov. 2017, Kanazawa, Japan
- (3) H. Yamaguchi: “Nuclear astrophysics projects at the low-energy RI beam separator CRIB”, The 8th Nuclear Physics in Astrophysics International conference (NPA8), Jun. 18–23, 2017, INFN-LNS, Catania, Italy.
- (4) S. Hayakawa: “Measurements of the ${}^7\text{Be}+n$ Big-Bang nucleosynthesis reactions at CRIB by the Trojan Horse method”, The 8th Nuclear Physics in Astrophysics International Conference (NPA8), June 18–23, 2017, Catania, Italy
- (5) H. Yamaguchi: “Indirect studies on astrophysical reactions at the low-energy RI beam separator CRIB”, The 14th International Symposium on Origin of Matter and Evolution of the Galaxies (OMEG2017), Jun. 27-30, 2017, Hotel ICC, Daejeon, Korea.
- (6) S. Hayakawa: “Measurements of the neutron-induced reactions on ${}^7\text{Be}$ with CRIB by the Trojan Horse method”, The 14th international symposium on Origin of Matter and Evolution of Galaxies (OMEG2017), Jun. 27–30 2017, Daejeon, Rep. of Korea.
- (7) H. Yamaguchi (invited): “Direct measurements and detection techniques with low-energy RIBs”, 9th European Summer School on Experimental Nuclear Astrophysics (Santa Tecla School), Sep. 17–24, 2017, Hotel Santa Tecla Palace, Acireale, Italy.
- (8) H. Shimizu : “Isomeric ${}^{26m}\text{Al}$ Beam Production with CRIB”, The 9th European Summer School on Experimental Nuclear Astrophysics, Sep. 17–24, 2017, Hotel Santa Tecla Palace, Acireale, Italy.
- (9) H. Yamaguchi (invited): “Studying nuclear astrophysics and nuclear clustering at the low-energy RI beam separator CRIB”, The International Symposium on Physics of Unstable Nuclei 2017 (ISPUN2017), Sep. 25-30, 2017, Wyndham Legende Halong Hotel, Halong, Vietnam.
- (10) H. Yamaguchi (oral, invited): “Study on alpha-cluster states via resonant scattering with low-energy RI beams”, Workshop on Nuclear Cluster Physics 2017 (WNCP2017), Oct. 25–27, 2017, Hokkaido University, Sapporo, Japan.
- (11) K. Yako(invited) “Exploring nuclear structure by double charge exchange reactions in Japan”, Conference on Neutrino and Nuclear Physics (CNNP2017), Oct. 15-21, 2017, University of Catania, Catania, Italy.
- (12) P. Schrock (oral), “Shell structure at the border of the island of inversion: Spectroscopy of neutron-rich Al isotopes. The International Symposium on Physics of Unstable Nuclei 2017, Sept. 25–30, 2017, Ha-noi, Vitnam,
- (13) S. Shimoura (Oral): “REDUCTION AND RESOURCE RECYCLING OF HIGH-LEVEL RADIOACTIVE WASTES THROUGH NUCLEAR TRANSMUTATION - NUCLEAR REACTION DATA OF LONG-LIVED FISSION PRODUCTS”, International Nuclear Fuel Cycle Conference (GLOBAL2017), September 24–29, 2017, Seoul, Korea.
- (14) S. Shimoura (Invited): “New energy-degrading beam line OEDO in RIKEN RI beam factory”, The International Symposium on Physics of Unstable Nuclei 2017 (ISPUN17), September 25–30, 2017, Halong City, Vietnam.
- (15) P. Schrock (oral): “Shell structure at the border of the island of inversion: Spectroscopy of neutron-rich Al isotopes.”, The International Symposium on Physics of Unstable Nuclei 2017 (ISPUN17), September 25–30, 2017, Halong City, Vietnam.
- (16) S. Shimoura (invited): “Tetra-neutron system studied by (${}^8\text{He}$, ${}^8\text{Be}$) reaction”, Workshop on Nuclear Structure and Reaction Theories: Building Together for the Future, October 9–13, 2017, GANIL, Caen, France.

- (17) S. Shimoura (Invited): “Tetra-neutron system populated by RI-beam experiments”, Critical Stability of Quantum Few-Body Systems (crit17), October 16–20, 2017, MPIPKS, Dresden, Germany.
- (18) S. Shimoura (invited): “Experimental studies of the tetra-neutron system by using RI-beam”, The 23rd European Conference on Few-Body Problems in Physics, Aug. 8–12, 2016, Aarhus, Denmark.
- (19) S. Shimoura (invited): “Exotic nuclei studied by exotic reaction”, Ito International Research Center (IIRC) Symposium “ Perspectives of the Physics of Nuclear Structure ”, November 1–4, 2017, UTokyo, Tokyo, Japan.
- (20) S. Michimasa (invited): “ Direct mass measurement of Calcium isotopes beyond $N = 34$ ”, International symposium “Perspectives of the physics of nuclear structure”, November 1–4, 2017, the University of Tokyo, Hongo, Tokyo, Japan.
- (21) S. Shimoura (invited): “Tetra-neutron system studied by $^4\text{He}(^8\text{He}, ^8\text{Be})$ ”, Workshop on Nuclear Cluster Physics (WNCP2016), Oct. 17–21, 2016, Kanto-Gakuin University, Yokohama, Japan.
- (22) S. Shimoura (invited): “Tetra-neutron system populated by using RI-beam induced reaction”, 第6回「中性子星の核物質」研究会, Dec. 1–3, 2017, RIKEN Nishina Center, Wako, Saitama, Japan.
- (23) N. Imai (Invited): “将来計画WG不安定核班第2期からの報告”, RIBF 理論若手放談会：エキゾチック核物理の広がり Jul. 31 – Aug.2, 2017 理研神戸・融合連携イノベーション推進棟
- (24) N. Imai: “surrogate reaction of $^{79}\text{Se}(n,\gamma)^{80}\text{Se}$ ” ImPACT-OEDO workshop, July 13–14, 2017, RIBF conference room, Wako, Saitama, Japan.
- (25) M. Dozono: “p/d induced reaction of ^{107}Pd ”, ImPACT-OEDO workshop, July 13–14, 2017, RIBF conference room, Wako, Saitama, Japan.
- (26) S. Michimasa: “Preliminary report of OEDO commissioning”, ImPACT-OEDO workshop, July 13–14, 2017, RIBF conference room, Wako, Saitama, Japan.
- (27) N. Imai (invited): “Energy-degraded beam line at RIBF, OEDO” International Workshop on “Physics Opportunities using CAGRA and RCNP tracking Ge detector ” (CAGRA17), Oct 10-12, 2017 Sigma Hall, Toyonaka Campus, Osaka University, Osaka, Japan
- (28) P. Schrock (invited): “Transfer Reactions with CAGRA at OEDO”, International Workshop on “ Physics Opportunities using CAGRA and RCNP tracking Ge detector ” (CAGRA17) Oct 10-12, 2017 Sigma Hall, Toyonaka Campus, Osaka University, Osaka, Japan
- (29) O. Beliuskina: “The ultrafast dE-ToF sc diamond detector”, International Workshop on “ Physics Opportunities using CAGRA and RCNP tracking Ge detector ” (CAGRA17), Oct 10 - 12, 2017 Sigma Hall, Toyonaka Campus, Osaka University, Osaka, Japan
- (30) N. Imai(Invited): “OEDO を用いた低エネルギー LLFP の核反応データ取得”, Nov. 16–17, 2017, 東海村産業情報プラザ (アイヴィル)
- (31) N. Imai (Invited): “Nuclear Data of LLFP and Future prospect of a new energy degraded beam line OEDO”, RIBF Users group meeting, Dec. 6, 2017, RIBF conference room
- (32) O. Beliuskina (oral): “The ultrafast dE-ToF single crystal diamond detector”, The 6th ADAMAS Workshop, Nov. 27–28, 2017, Zagreb, Croatia.
- (33) S. Ota, “Nuclear matter from low-energy reaction ”, OEDO Workshop, Jul.15, 2017, CNS Wako campus, Saitama, Japan
- (34) S. Ota, “Equation of state of nuclear matter from direct reactions ”, Workshop on RI and Heavy-ion science, Oct. 19-20, 2017, Ewha womans university, Seoul, Korea
- (35) S. Ota, “Active targets CAT ’ s for missing mass spectroscopy with high-intensity beams ”, Workshop on active targets and time projection chambers for high-intensity and heavy-ion beams in nuclear physics, Jan. 17-19, Santiago de Compostela University, Spain.
- (36) N. Shimizu, “ Double Gamow-Teller transition and its relation to neutrinoless double beta decay ”, Nuclear ab initio Theories and Neutrino Physics, Seattle, USA, March 2018.

- (37) N. Shimizu, “Shell model study on a double-beta decay nucleus ^{48}Ca ”, “Probing fundamental interactions by low energy excitations”, KTH Royal Institute of Technology, Stockholm, Sweden, June 2017.
- (38) T. Miyagi, “Recent progress in the unitary-model-operator approach”, TRIUMF workshop on Progress in Ab Initio Techniques in Nuclear Physics, Vancouver, Canada, March 2018.
- (39) T. Miyagi, “Unitary-model-operator approach calculations with the chiral NN+3N forces”, 16th CNS Summer School, RIKEN, Wako, Japan, August 2017.
- (40) T. Miyagi, “Ground-state energies and radii from the unitary-model-operator approach”, Probing fundamental interactions by low energy excitations -Advances in theoretical nuclear physics, Royal Institute of Technology, Stockholm, Sweden, June 2017.
- (41) Y. Utsuno, “Shell-model study for the $A \sim 130$ region”, Gif-Sur-Yvette, France (Conference “Shapes and Symmetries in Nuclei: from Experiment to Theory (SSNET ’17)”), November 2017.
- (42) Y. Utsuno, “Consistent description of shell gaps and deformed states around O-16 and Ca-40”, Mumbai, India (Conference “Frontiers in Gamma Ray Spectroscopy (FIG18)”), March 2018.
- (43) T. Abe, “Advances in the Monte Carlo Shell Model for Understanding Nuclear Structure”, Ito International Center (IIRC) Symposium “Perspectives of the Physics of Nuclear Structure”, Ito Hall, the University of Tokyo, November 2017.
- (44) T. Abe, “Recent advances in the no-core Monte Carlo shell model”, “Progress in Ab Initio Techniques in Nuclear Physics”, TRIUMF, Canada, March 2018.
- (45) Y. Tsunoda, “Monte Carlo shell model calculations for structure of nuclei around $Z=28$ ”, IVth Topical Workshop on Modern Aspects in Nuclear Structure, Bormio, Italy, February 2018.
- (46) Y. Tsunoda, “Nuclear structure studied by Monte Carlo shell model calculations”, NUSTAR Annual Meeting 2018, GSI, Darmstadt, Germany, March 2018.
- (47) N. Tsunoda, “Exotic neutron-rich medium-mass nuclei with realistic nuclear force”, Keystone ARIS2017, May 2017.
- (48) N. Tsunoda, “Structure of exotic nuclei based on nuclear force”, Perspective of physics of nuclear structure, Tokyo, Japan, November 2017.
- (49) N. Tsunoda, “Many body perturbation theory for the effective interaction for the shell model calculation and its application to island of inversion”, Leuven-Tokyo mini workshop, Tokyo, Japan, March 2018.
- (50) Y. Tsunoda, “Shapes of medium-mass nuclei studied by Monte Carlo shell model calculations”, RCNP International workshop on “Physics Opportunities using CAGRA and RCNP tracking Ge detector” (CAGRA17), Osaka University, October, 2017
- (51) Y. Tsunoda (poster), “Shapes of medium and heavy nuclei studied by Monte Carlo shell model calculations”, Ito International Research Center (IIRC) symposium “Perspectives of the physics of nuclear structure”, the University of Tokyo, November, 2017
- (52) J. Menéndez, “Nuclear matrix elements for double-beta decay: present and future”, Solvay workshop “Beyond the Standard model with Neutrinos and Nuclear Physics”, Brussels (Belgium), 30 November 2017.
- (53) J. Menéndez, “Nuclear Matrix Elements for Fundamental Symmetries”, “Perspective of the Physics of Nuclear Structure” Conference, Tokyo (Japan), 4 November 2017.
- (54) J. Menéndez, “Double Gamow-Teller transition of ^{48}Ca and its relation to neutrinoless double-beta decay”, “Conference on Neutrino and Nuclear Physics (CNNP2017)”, Catania (Italy), 17 October 2017.
- (55) J. Menéndez, “The interplay of nuclear structure with β and double- β decays”, “International Symposium on Physics of Unstable Nuclei 2017 (ISPUN17)”, Halong City (Vietnam), 26 September 2017.
- (56) J. Menéndez, “Status of neutrinoless double-beta decay nuclear matrix elements”, “Recent developments in neutrino physics and astrophysics” workshop, Gran Sasso (Italy), 6 September 2017.

- (57) J. Menéndez, “Which nuclear data and correlations can constrain neutrinoless double-beta decay matrix elements?”, INT Program “Neutrinoless Double-beta Decay”, Seattle (USA), 21 June 2017.
- (58) S. Hayashi, “ J/ψ production in heavy ion collisions”, Heavy Ion Café, January 13, 2018, RIKEN, Wako, Japan
- (59) S. Hayakawa: “CRIB での 7Be ビームを用いたビッグバン元素合成反応の測定”, X 線天体と元素合成を中心とする宇宙核物理研究会, July 20–21, 2017, RIKEN, Wako, Japan.
- (60) H. Shimizu: “CRIB における 26Al 核異性体の陽子弾性共鳴散乱実験”, X 線天体と元素合成を中心とする宇宙核物理研究会, July 20–21, 2017, RIKEN, Wako, Japan.
- (61) 山口英斉: “ α 共鳴散乱による不安定核クラスター状態の研究”, Aug 3-5, 2017, RCNP 研究会「核子・ストレンジネス多体系におけるクラスター現象」大阪大学核物理研究センター
- (62) S. Michimasa: “SHARAQ スペクトロメータを用いた中性子過剰核の直接質量測定”, 第 7 回先導原子力研コロキウム, July 21, 2017, Tokyo Institute of Technology, Meguro, Tokyo, Japan.
- (63) S. Michimasa et al.: “LLFP 安定核種化・短寿命化のための核変換法の開発 (6)OEDO ビームラインの性能評価”, AESJ Fall meeting, Sept. 13–15, Hokkaido University, Sapporo, Hokkaido, Japan.
- (64) S. Michimasa et al.: “低速 RI ビームを用いた LLFP 核の核反応断面積測定”, AESJ Spring meeting, Mar. 26–28, Osaka University, Osaka, Japan.
- (65) M. Dozono et al.: “低速 RI ビームを用いた $107\text{Pd}, 93\text{Zr}$ の陽子および重陽子誘起反応測定”, AESJ Spring meeting, Mar. 26–28, Osaka University, Osaka, Japan.
- (66) 清水則孝, 「ベイズ統計による殻模型計算の解析」, 素粒子・原子核・宇宙「京からポスト京に向けて」シンポジウム, 筑波大学文京校舎, 2017 年 12 月.
- (67) 清水則孝, 「殻模型計算による核準位密度の微視的記述」, 2017 年度核データ研究会, 茨城県東海村・東海駅前・アイヴィル, 2017 年 11 月.
- (68) 宮城宇志, 「中重核における 3 体力の効果」, RIBF 理論若手放談会: エキゾチック核物理の広がり, 理化学研究所, 神戸キャンパス, 2017 年 8 月.
- (69) 角田佑介, 「モンテカルロ殻模型による原子核形状の研究」, RIBF 理論若手放談会: エキゾチック核物理の広がり, 理化学研究所神戸キャンパス, 2017 年 7 月.
- (70) 角田佑介, 「中重核・重い原子核の形状のモンテカルロ殻模型による研究」, 素粒子・原子核・宇宙「京からポスト京に向けて」シンポジウム, 筑波大学東京キャンパス文京校舎, 2017 年 12 月.
- (71) 角田佑介, 「量子自己組織化と原子核の集団性」, 研究会「量子クラスターで読み解く物質の階層構造」, 東京工業大学大岡山キャンパス, 2018 年 3 月.
- (72) 角田直文, 「Medium-mass nuclei from nuclear force」, 京都大学 基研研究会「核力に基づく核構造・核反応物理の展開」, 2017 年 3 月.
- (73) 角田直文, 「核力と中性子過剰核の構造」, 理研神戸・融合連携イノベーション推進棟 RIBF 若手放談会「エキゾチック核物理の広がり」, 2017 年 7, 8 月.
- (74) 小高 康照他 “空間電荷効果を導入した理研 AVF サイクロトロン入射軌道解析”, 第 14 回日本加速器学会年会, 2016 年 8 月 1-3 日, 北海道札幌市 北海道大学
- (75) 大城幸光 (oral): 「CNS イオン源の現状」, 第 14 回 AVF 合同打合せ, 2017 年 6 月 29-30 日, 福島県立医科大学
- (76) 小高康照 (oral): 「4 次元エミッタンス測定値を用いた AVF 入射軌道解析 (2)」, 第 14 回 AVF 合同打合せ, 2017 年 6 月 29-30 日, 福島県立医科大学
- (77) 大城幸光 (oral): 「CNS イオン源の現状」, 第 15 回 AVF 合同打合せ, 2018 年 2 月 26-27 日, 大阪大学 RCNP
- (78) 小高康照 (oral): 「AVF 入射軌道解析の現状」, 第 15 回 AVF 合同打合せ, 2018 年 2 月 26-27 日, 大阪大学 RCNP

B. JPS Meetings

- (1) N. Imai: “不安定核物理の将来”, JPS Fall meeting, Sept. 12–15, Utsunomiya University, Utsunomiya, Tochigi, Japan.
- (2) T. Gunji, “高エネルギー重イオン衝突による物理の将来”, JPS Fall meeting, Sept. 12–15, Utsunomiya University, Utsunomiya, Tochigi, Japan.
- (3) S. Hayashi, “Inclusive J/ψ measurement in p-Pb collisions with the ALICE detector”, JPS Autumn Meeting 2017, September 12-15, 2017, Utsunomiya University, Utsunomiya, Japan
- (4) Y. Sekiguchi for the ALICE collaboration, “Study of particle correlations in p-Pb collisions with ALICE detector”, 日本物理学会 2017 年秋季大会、宇都宮大学、峰キャンパス、9 月 12 日-15 日
- (5) H. Murakami for the ALICE collaboration, “Status of direct photon measurement in small systems with ALICE”, 日本物理学会 2017 年秋季大会 宇都宮大学
- (6) 早川勢也 (oral): “トロイの木馬法による $7\text{Be}+n$ ビッグバン元素合成反応の測定 II”, 日本物理学会 2017 年秋季大会, Sep 12–15, 2017, 宇都宮大学.
- (7) N. Kitamura et al.: “TRIUMF におけるトリチウム標的の評価”, JPS Fall meeting, Sept. 12–15, Utsunomiya University, Utsunomiya, Tochigi, Japan.
- (8) K. Kawata et al.: “ ^{58}Ni の入射核破砕反応による高スピンアイソマービームの生成”, JPS Fall meeting, Sept. 12–15, Utsunomiya University, Utsunomiya, Tochigi, Japan.
- (9) C. Iwamoto et al.: “ガスアクティブ標的 CAT の大型化に向けた二重増幅率抑制型多層 THGEM の開発”, JPS Fall meeting, Sept. 12–15, Utsunomiya University, Utsunomiya, Tochigi, Japan.
- (10) 清水則孝, 「ボゴリューボフ準粒子基底によるモンテカルロ殻模型」, 日本物理学会 2017 年秋季大会 (宇都宮大学峰キャンパス), 2017 年 9 月.
- (11) 宮城宇志, 「3 体力効果を取り込んだ UMOA 計算」, 日本物理学会 2017 年秋季大会, 宇都宮大学, 峰キャンパス, 2017 年 9 月.
- (12) 角田佑介, 「モンテカルロ殻模型による Sm 同位体の形状変化の研究」, 日本物理学会 2017 年秋季大会、宇都宮大学峰キャンパス, 2017 年 9 月.
- (13) 角田佑介, 「Sm 同位体の形状変化のモンテカルロ殻模型による研究」, 日本物理学会第 73 回年次大会、東京理科大学野田キャンパス, 2018 年 3 月.
- (14) 角田直文, 「中性子過剰な Mg 同位体の新たな様相」, 宇都宮大学 日本物理学会 2017 年秋季大会, 2017 年 9 月.
- (15) 角田直文, 「原子核殻模型における統計力学的考察」, 宇都宮大学 日本物理学会 2017 年秋季大会, 2017 年 9 月.
- (16) 角田直文, 「現実的核力に基づく多殻有効相互作用の構築と中性子過剰核への適用」, 東京理科大学 日本物理学会第 73 回年次大会, 2018 年 3 月
- (17) 富樫智章, 「Zr 同位体近傍における形の量子相転移のモンテカルロ殻模型による研究」, 宇都宮大学, 日本物理学会 2017 年秋季大会, 2017 年 9 月
- (18) 富樫智章, 「大規模殻模型計算による中性子過剰 $N=82$ 近傍の半減期の計算」, 宇都宮大学, 日本物理学会 2017 年秋季大会, 2017 年 9 月
- (19) 富樫智章, 「モンテカルロ殻模型による Sn 同位体の系統的研究」, 東京理科大学, 日本物理学会第 73 回年次大会, 2018 年 3 月.

C. Lectures

- (1) S. Shimoura: “エキゾチック原子核の世界”, 集中講義, June 9, 16, 23, 2017, 立教大学
- (2) S. Shimoura: “Direct Reaction”, Rewriting Nuclear Physics Textbooks: Basic nuclear interactions and their link to nuclear processes in the cosmos and on earth, July 24–28, 2017, Pisa, Italy
- (3) S. OTA, “Matter dominant universe through nuclear physics ’ ’”, High school lecture for Fukuoka Prefectural Chikushigaoka High School, Aug. 1, 2017, CNS Wako campus, Saitama, Japan

D. Seminars

- (1) H. Yamaguchi : “CRIB and OEDO - the low energy RI beam facilities of CNS, the University of Tokyo”, Nov. 10, 2017, Nuclear Physics Seminar, Beihang University, Beijing, China.

Personnel

Director

SHIMOURA, Susumu

*Professor, Graduate School of Science
Center for Nuclear Study*

Scientific Staff

SAKEMI, Yasuhiro

Professor

YAKO, Kentaro

Associate Professor

IMAI, Nobuaki

Associate Professor

GUNJI, Taku

Associate Professor

SHIMIZU, Noritaka

Project Associate Professor

YAMAGUCHI, Hidetoshi

Lecturer

WIMMER, Kathrin

Lecturer

MICHIMASA, Shin'ichiro

Assistant Professor

OTA, Shinsuke

Assistant Professor

NAGAHAMA, Hiroki

Assistant Professor

Guest Professors

UTSUNO, Yutaka

JAEA

MIZOI, Yutaka

Osaka Electro-Communication University

Technical Staff

KOTAKA, Yasuteru

Technical Assistants

KATAYANAGI, Mamoru

OHSHIRO, Yukimitsu

KUREI, Hiroshi

KOJIMA, Reiko

Post Doctoral Associates

TOGASHI, Tomoaki

HAYASHI, ShinIchi

STUHL, Laszlo

MENENDEZ SANCHEZ, Javier

HAYAKAWA, Seiya

YANG, Lei

HWANG, Jongwon

BELIUSKINA, Olga

ABE, Takashia

ICHIKAWA, Takatoshi

SCHROCK, Philipp

DOZONO, Masanori

ZHANG, Ningtao

IWAMOTO, Chihiro

TSUNODA, Yusuke

MIYAGI, Takayuki

TSUNODA, Naofumi

Graduate Students

TOKIEDA, Hiroshi

NAKAJIMA, Ryo

SHIMIZU, Hideki

KAWATA, Keita

TSUNODA, Rieko

SEKIGUCHI, Yuko

KITAMURA, Noritaka

TAKAKI, Motonobu

MASUOKA, Soichiro

Administration Staff

OKI, Mikio

YAMAMOTO, Ikuko

ENDO, Takako

KISHI, Yukino

SOMA, Yuko

Committees

Steering Committee

TAKEDA, Hiroyuki	<i>Department of Biological Sciences, Graduate School of Science, UT</i>
HOSHINO, Masahiro	<i>Department of Earth and Planetary Physics, Graduate School of Science, UT</i>
HASEGAWA, Shuji	<i>Department of Physics, Graduate School of Science, UT</i>
SHIMOURA, Susumu	<i>Center for Nuclear Study, Graduate School of Science, UT</i>
SAKEMI, Yasuhiro	<i>Center for Nuclear Study, Graduate School of Science, UT</i>
YAKO, Kentaro	<i>Center for Nuclear Study, Graduate School of Science, UT</i>
SAKURAI, Hiroyoshi	<i>Department of Physics, Graduate School of Science, UT</i>
NAGAMIYA, Shoji	<i>RIKEN</i>
MORI, Toshinori	<i>International Center for Elementary Particle Physics, UT</i>
TAKAHASHI, Hiroyuki	<i>Department of Nuclear Engineering and Management, Graduate School of Engineering, UT</i>

